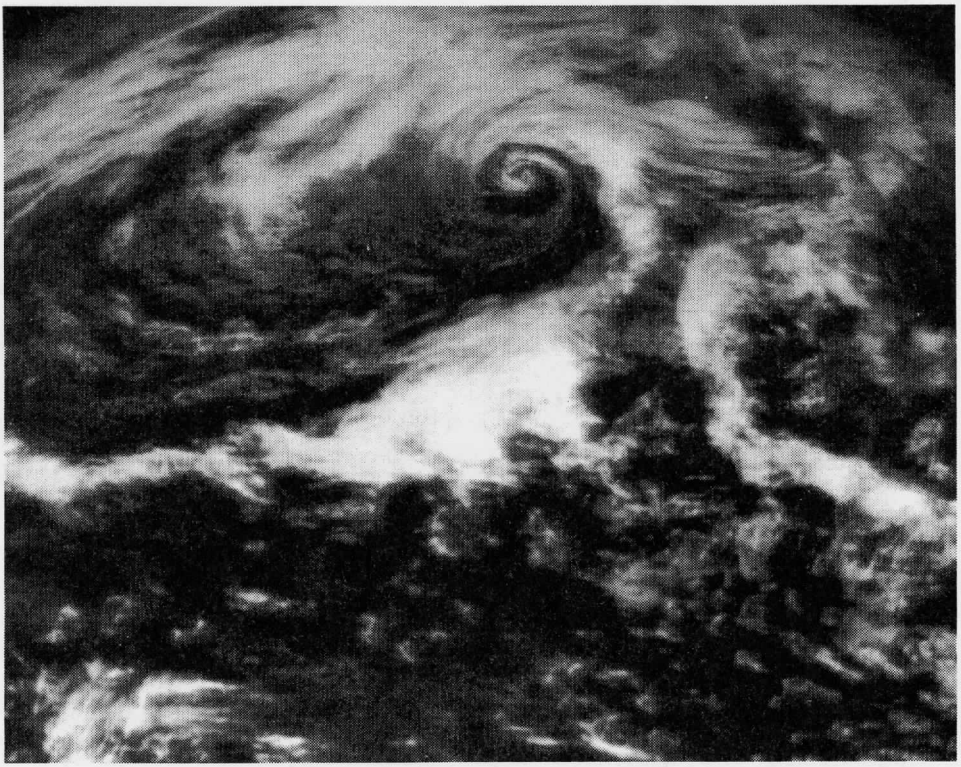

Annual Report 1971

STUDIES OF THE ATMOSPHERE USING AEROSPACE PROBES

Volume II: Application Studies

Space Science and Engineering Center, University of Wisconsin

COVER DESCRIPTION

An atmospheric cyclone, when viewed from a satellite, forms a distinctive cloud pattern which can be appreciated as both awesome and beautiful. The cover picture was obtained from the ATS-I satellite spin-scan camera over the mid-north Pacific on January 5, 1967. F. H. Nicholson, author of one of the papers in this report, was intrigued by the beauty of this storm. As an interesting exercise, he developed a mathematical curve to fit the cyclone's spirals. From this intellectual effort grew his paper in this volume, which presents a new general mathematical formulation of natural vortices. Of such is the stuff of science.

Space Science and Engineering Center
The University of Wisconsin
Madison, Wisconsin

STUDIES OF THE ATMOSPHERE USING AEROSPACE PROBES

Annual Report on

NOAA Grant 1-36036

1971

The research reported in this document has been supported by the National Oceanic and Atmospheric Administration

July, 1972

PREFACE

As we continue to work with data from the meteorological satellites, we discover aspects of the data which we had seen previously but which we had not appreciated fully. The papers in this volume pursue some of these observed phenomena with the intent of developing concepts for deriving quantitative measures of meteorological parameters.

Sromovsky has investigated the characteristics of the sun glint from the ocean's surface and has studied the use of this bright spot in measuring gaseous and particulate atmospheric constituents.

Auvine and Anderson have continued earlier work in using the rate of growth of cumulonimbus anvils to measure convective intensity and have substantiated the validity of this technique.

Nicholson and Johnson report on a deceptively simple, yet potentially important vortex model which describes observed phenomena precisely. We look forward to application of the model in operational employment of satellite images.

Each of the papers presents a beginning point for further work as well as a report of work completed. I am pleased to acknowledge this work by my associates, and I look forward to further developments in all three areas.

Verner E. Suomi
Principal Investigator

CONTENTS

Technical Articles

SUN GLINT AS AN ATMOSPHERIC PROBE

by L. A. Sromovsky

Introduction

Surface-based measurements of the attenuation of solar radiation by the atmosphere have revealed a wealth of information about its molecular and particulate constituents. It would be desirable to make such transmission measurements from a satellite platform in order to sample larger atmospheric volumes than is possible from the surface, and also in order to sample regions of the earth poorly covered by surface sensors (e.g., the oceanic regions). In addition, satellite observations might make possible the tracking of some variable constituents on a global scale.

It has been proposed that the sun glint (reflection of sunlight from the sea surface), which is so prominent in pictures from the ATS and many other satellites, could be used to determine both the absolute magnitude and relative wavelength dependence of atmospheric transmission over much of the wavelength region between .4μ and 4μ. In essence the sea surface is treated as a mirror of imperfect but determinable reflectivity. Comparison of the intensity expected from simple reflection by the mirror (calculated from what is known about the mirror) with the intensity of radiation which also makes two traverses of the atmosphere (directly observed from satellite) should reveal the atmospheric transmission and thus many properties of the atmospheric constituents.

In this report we will show that it is theoretically feasible to make use of the sun glint to determine two important factors in atmospheric transmission: 1) the wavelength dependence of the aerosol extinction coefficient, and 2) the fractional selective absorption due to molecular constituents. We find that these two factors can be determined without ground-based calibration of the sun glint and in the presence of significant background effects. The techniques which can accomplish this are detailed in this report.

Partially supported by E. P. A. Contract No. 68-02-0002.

The analysis on which our results are based considers, in order, the properties of the mirror, the sources and magnitudes of background signals, the way in which atmospheric transmission combines with other factors to determine the observed spectral radiances, and experimental measurements of spectral radiances which are needed to determine atmospheric transmission.

Properties of the Mirror (The Cox and Munk Model of the Sun Glint)

A perfectly flat sea surface would reflect an image of the sun with a radiance of approximately 2% that of the sun's disc (for near-normal to near -45° view angles). This reflected sunlight would constitute a small (10 milliradians in diameter) and extremely bright source (over 10^4 times as bright as the brightest cloud). However, the roughness of the sea surface degrades this image to a diffuse spot of much larger angular extent and much reduced radiance. A quantitative description of this effect is contained in the Cox and Munk model of the sun glint [1].

According to Cox and Munk, the ratio of the sea surface radiance to the incident flux density is proportional to the probability of finding parts of the sea surface tilted so as to reflect sunlight to the observer, namely

$$R \equiv N/F = \frac{1}{4}\rho(\omega)\frac{\sec^4\beta}{\cos\mu}\,p(Z_x, Z_y) \qquad (1)$$

where the following notation is employed (see Figure 1):

R = sun glint scattering coefficient (sterad^{-1})

N = sea surface radiance (W - m^{-2} - μ^{-1} - sterad^{-1})

F = solar flux density (W - m^{-2} - μ^{-1})

ω = angle of incidence and reflection

β = sea surface tilt angle relative to local normal

Z_x, Z_y = components of local sea surface slope ($Z_x^2 + Z_y^2 = \tan^2\beta$)

μ = angle between observing direction and local vertical

$\rho_\lambda(\omega)$ = Fresnel reflection coefficient of sea water at angle ω and wavelength λ

$p(Z_x, Z_y)\,dZ_x dZ_y$ = probability of finding sea surface slopes with x and y components in the range (Z_x, Z_x+dZ_x) and (Z_y, Z_y+dZ_y).

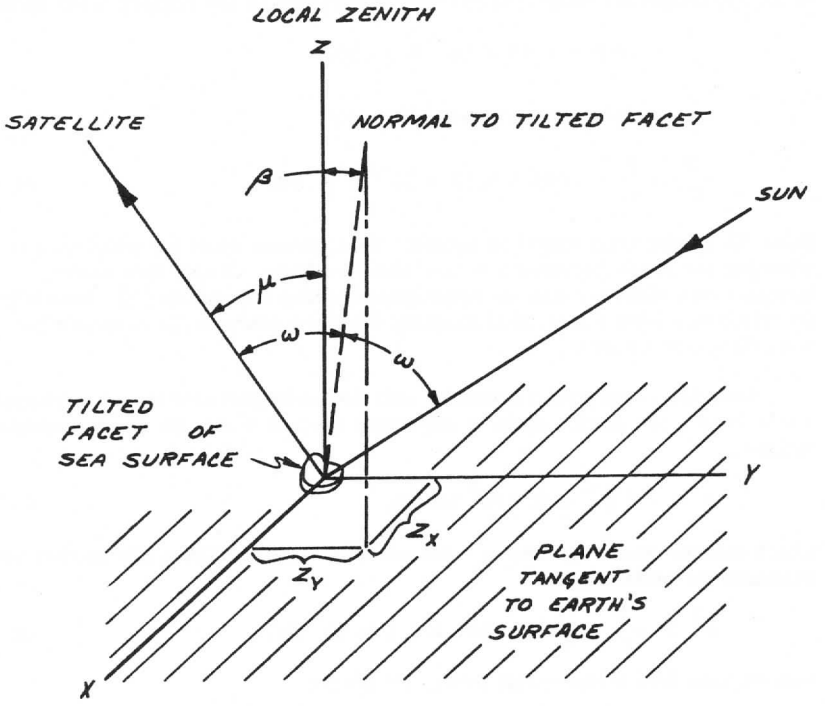

Figure 1. Geometry for calculating R, the sun glint scattering coefficient.

If the x and y axes are chosen to be aligned with the upwind and crosswind directions (denoted by u and c, respectively), the probability density takes the simple first-order form

$$p = (2\pi\sigma_c\sigma_u)^{-1} \exp(-\tfrac{1}{2}(Z_c^2/\sigma_c^2 + Z_u^2/\sigma_u^2)), \tag{2}$$

which is a two-dimensional gaussian function. Cox and Munk obtained the following empirical equations relating the widths to the surface wind speed:

$$\sigma_c^2 = .003 + 1.92 \times 10^{-3} W \pm .002$$

$$\sigma_u^2 = .000 + 3.16 \times 10^{-3} W \pm .004$$

$$\sigma_c^2 + \sigma_u^2 = .003 + 5.12 \times 10^{-3} W \pm .004 \tag{3}$$

Here W is the wind speed in m/sec. This fit was made for wind speeds covering the range between 1 m/sec and 14 m/sec. Using this model, Levanon was able to estimate wind speeds using ATS-I data [2]. Recently Kornfield has been successful in using the asymmetry in (2) to determine wind direction as well [3].

Since the crosswind asymmetry will not be significant to our subsequent discussions, we shall employ a somewhat simpler model for the probability density,

$$p = (\pi\sigma^2)^{-1} \exp(-1/\sigma^2 \tan^2\beta), \tag{4}$$

which results when σ_u and σ_c are assumed equal. The width in this one-dimensional model is just

$$\sigma^2 = \sigma_c^2 + \sigma_u^2 = .003 + 5.12 \times 10^{-3} W. \tag{5}$$

Substituting this latter result in Eq. (1) yields

$$R = \frac{1}{4} \rho_\lambda(\omega) \frac{\sec^4\beta}{\cos\mu} \frac{1}{\pi\sigma^2} \exp(-\tan^2\beta/\sigma^2) . \tag{6}$$

This model describes the broadening of the glitter pattern with increasing wind speed, and also the accompanying reduction in the peak of the sea surface radiance. Note that the maximum sun glint signal occurs for $\tan\beta = 0$ (the point of specular reflection for a calm sea), and has the form

$$R_{SP} = \frac{1}{4\pi\sigma^2} \rho_\lambda(\omega) \sec\mu , \tag{7}$$

where R_{SP} denotes the sun glint scattering coefficient at the specular point. The wind dependence of R_{SP} for $\mu = \omega = 0$ is shown in Figure 2. It is significant that the only wavelength dependence of R comes about through the Fresnel reflection coefficient $\rho_\lambda(\omega)$. Given the dependence of $\rho_\lambda(\omega)$ on λ we could thus determine the value of R at any wavelength by measuring it at only one. However there seems to be a significant disagreement between experimental results for $\rho_\lambda(\omega)$ even for pure H_2O, especially in the infrared region (Figure 3). There has been some recent work on the differential behavior of pure H_2O and sea water [4], but this is of little use in absolute terms. In addition there is little information available on the variability of sea water over the globe or as a function of time. The frequency of surface slicks is particularly important information in this context.

Background Radiation

In addition to simple atmospheric attenuation, there are a number of extraneous background sources which can also modify the apparent brightness of the sun glint. These may be classified as follows:

1) skylight (molecular and aerosol), radiance = S_1F

2) sky glint (reflection of skylight by the sea surface), radiance = S_2F

3) sea light (solar radiance scattered by molecules and particulate matter in the sea), radiance = S_3F

4) foam light (solar radiation scattered by whitecaps), radiance = S_4F

5) black body radiation of the earth, radiance = B .

These sources are pictorially presented in Figure 4. Note that the first four are proportional to the extraterrestrial solar flux F as is the sun glint. Thus a comparison of these sources with the sun glint is readily made as a comparison of their effective scattering coefficients S_i with the sun glint scattering coefficient R .

1. Skylight

Extensive tables of the effective scattering coefficient for a plane parallel Rayleigh atmosphere have been compiled by Coulson, Dave and Sekera [5]. Their results include the effects of polarization and multiple scattering. However, except for optical depths greater than unity, little error is made by using a single scattering model (see Figure 5), which

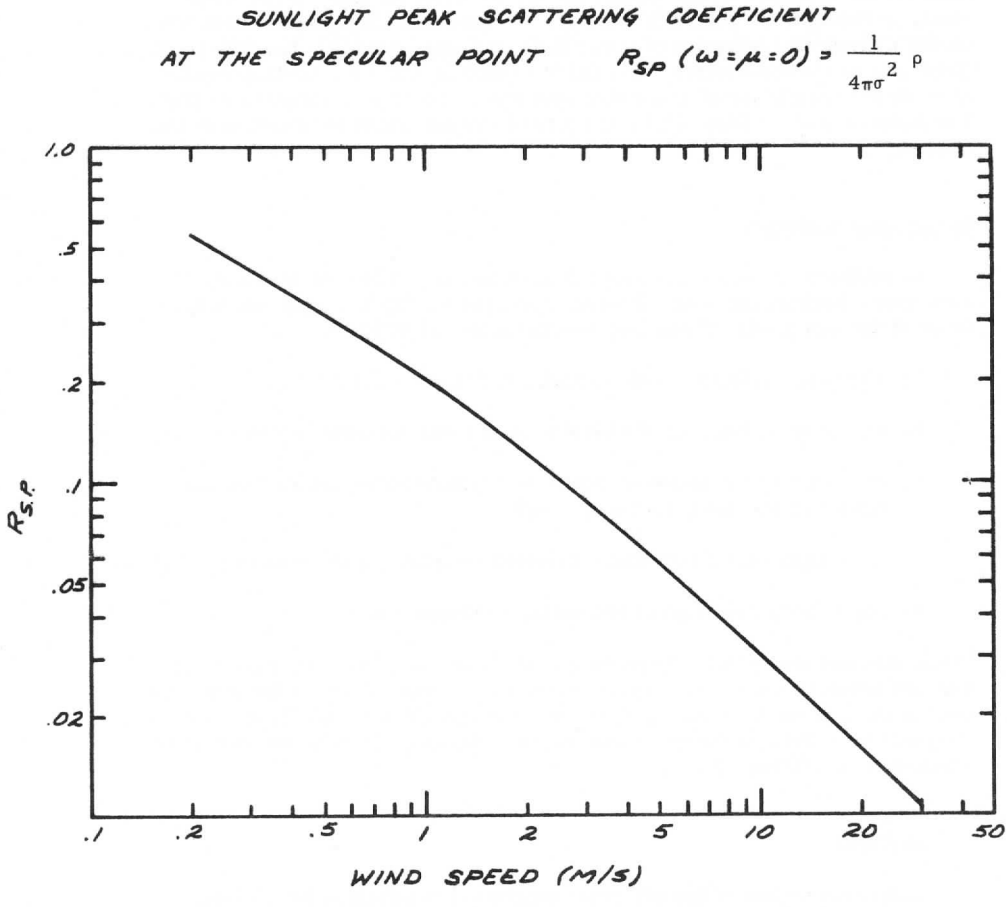

Figure 2. Dependence of the sun glint peak scattering coefficient on wind speed.

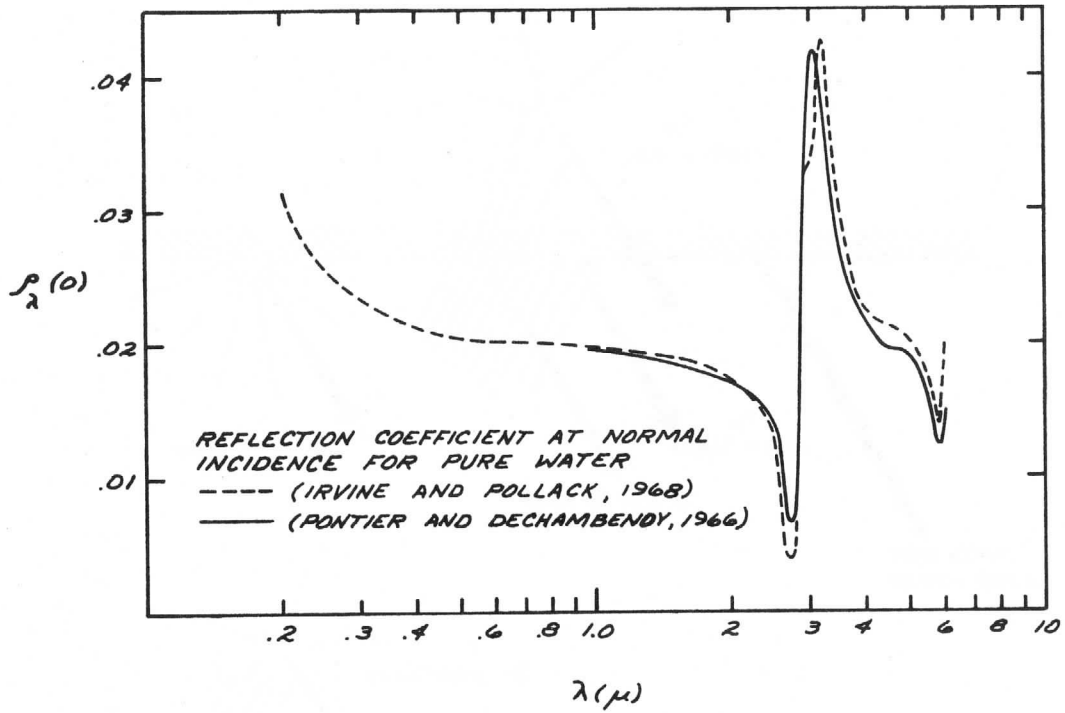

Figure 3. Wavelength dependence of ρ_λ ($\omega = 0°$) for pure water.

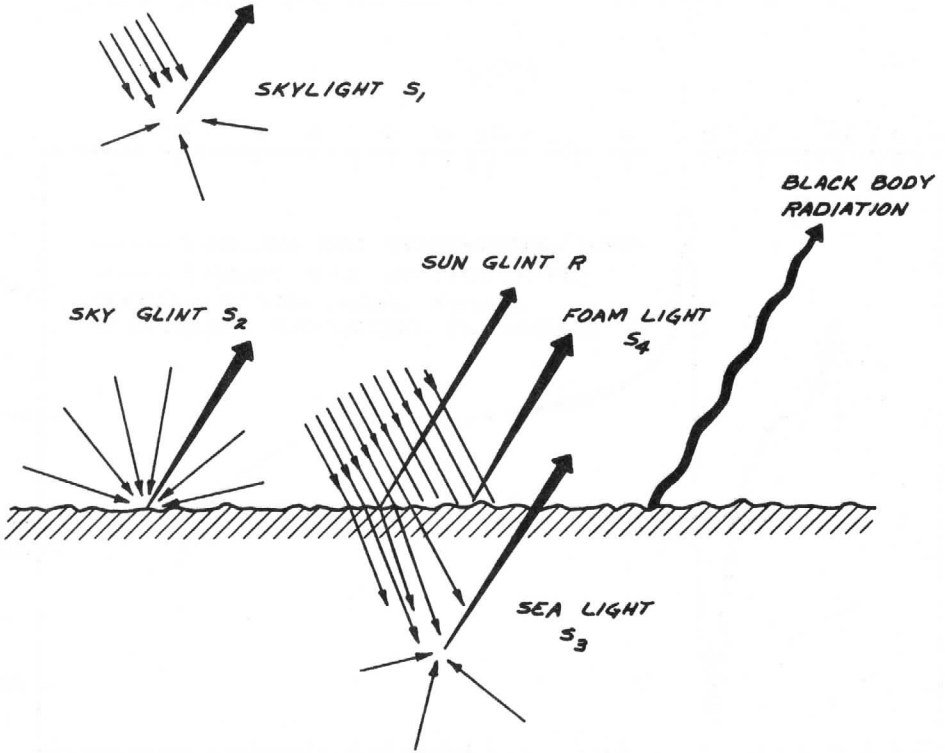

Figure 4. Sources of Background.

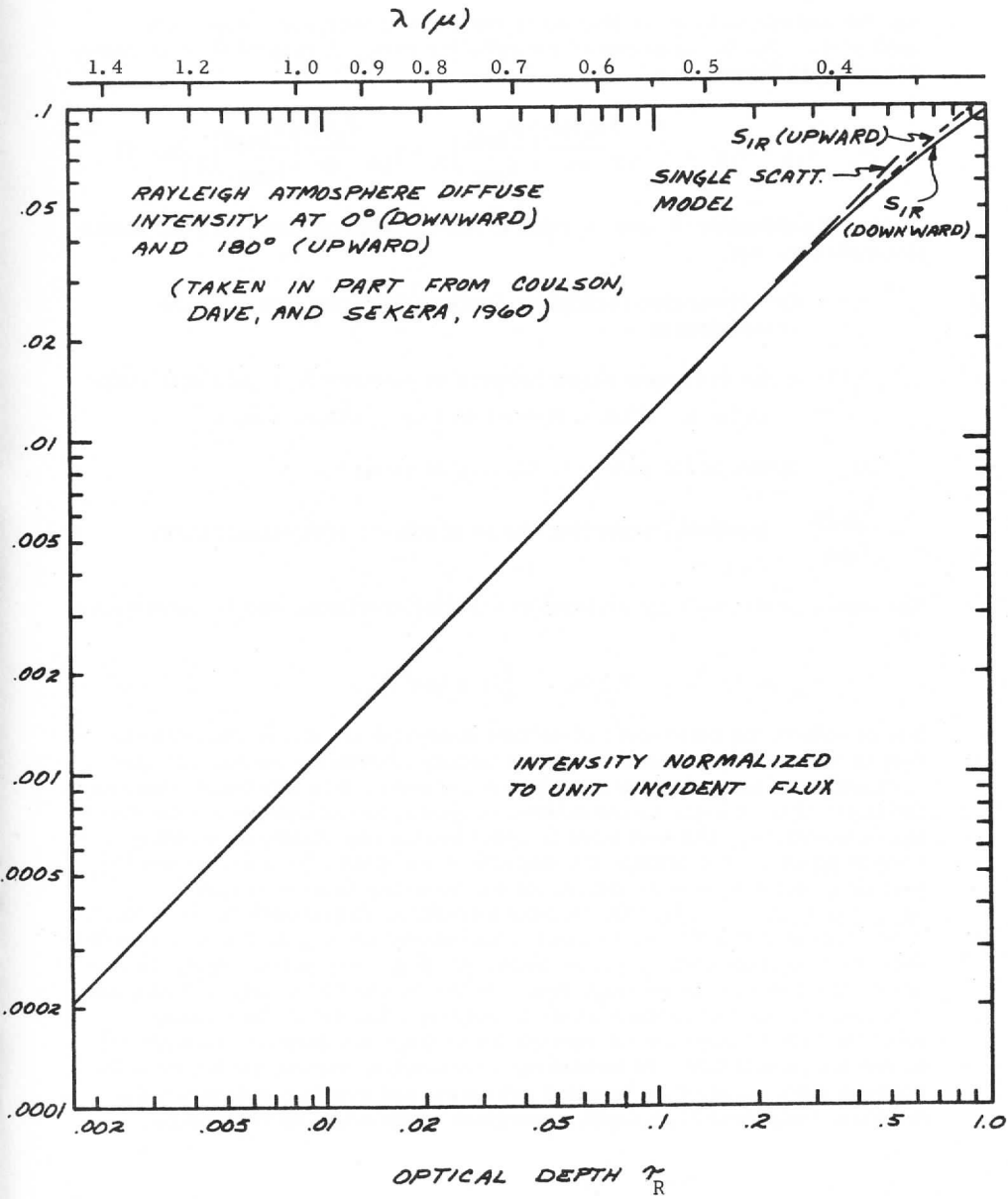

Figure 5. Rayleigh Scattering (exact and single scattering model).

has the advantage of great simplicity and easy inclusion of the aerosol component. For the purposes of a feasibility study, it is more than adequate. According to this model

$$S_1 = S_{1R} + S_{1A} = \left[\tau_{\lambda R} \frac{P_R(\theta)}{4\pi} \left(\frac{\beta_{scat}}{\beta_{ext}} \right)_R + \tau_{\lambda A} \frac{P_A(\theta)}{4\pi} \left(\frac{\beta_{scat}}{\beta_{ext}} \right)_A \right] M, \quad (8)$$

where the subscripts R and A refer to the Rayleigh and aerosol components respectively, and

τ_λ = the attenuation coefficient (optical depth per unit air mass) at wavelength λ

$P_\lambda(\theta)$ = the scattering phase function at wavelength λ and scattering angle θ. (This is defined so that $\int P(\theta) d\Omega = 4\pi$.)

M = number of air masses in the line of sight.

$\frac{\beta_{scat}}{\beta_{ext}}$ = fractional extinction due to scattering (efficiency factor).

The important and well known facts of Rayleigh scattering may be summarized as

$$\tau_{\lambda R} \propto 1/\lambda^4 \quad ; \quad P_{\lambda R}(\theta) = \frac{3}{4}(1 + \cos^2\theta). \quad (9)$$

The corresponding parameters of aerosol scattering are not so well known. Part of the problem results from the variability of both the number and size distribution of aerosol particles. We shall conduct this feasibility study on the basis of what might be considered as typical aerosol properties for maritime environment, although there is considerable uncertainty in deciding what is typical. The attenuation measurements of Volz [6] and Quenzel [7] lead us to believe that we will not be too far wrong to assume that $\tau_{A,\lambda} = 0.1$ for $\lambda = .7\mu$, and that the wavelength dependence of τ_λ (which appears to be fairly flat in the visible region) and of $P_{\lambda A}(\theta)$ are approximately described by Deirmendjian's haze model M [8]. In general, $P_A(\theta)$ is two orders of magnitude larger than $P_R(\theta)$ in the forward direction, and an order of magnitude smaller in the backward direction (Figure 6). This makes aerosols easy to see from the surface (as in the sun's aureole) and difficult to see from a satellite. At increasing wavelengths, aerosol scattering falls off much more slowly than Rayleigh scattering and eventually becomes the dominant component of skylight, regardless of the angle of observation.

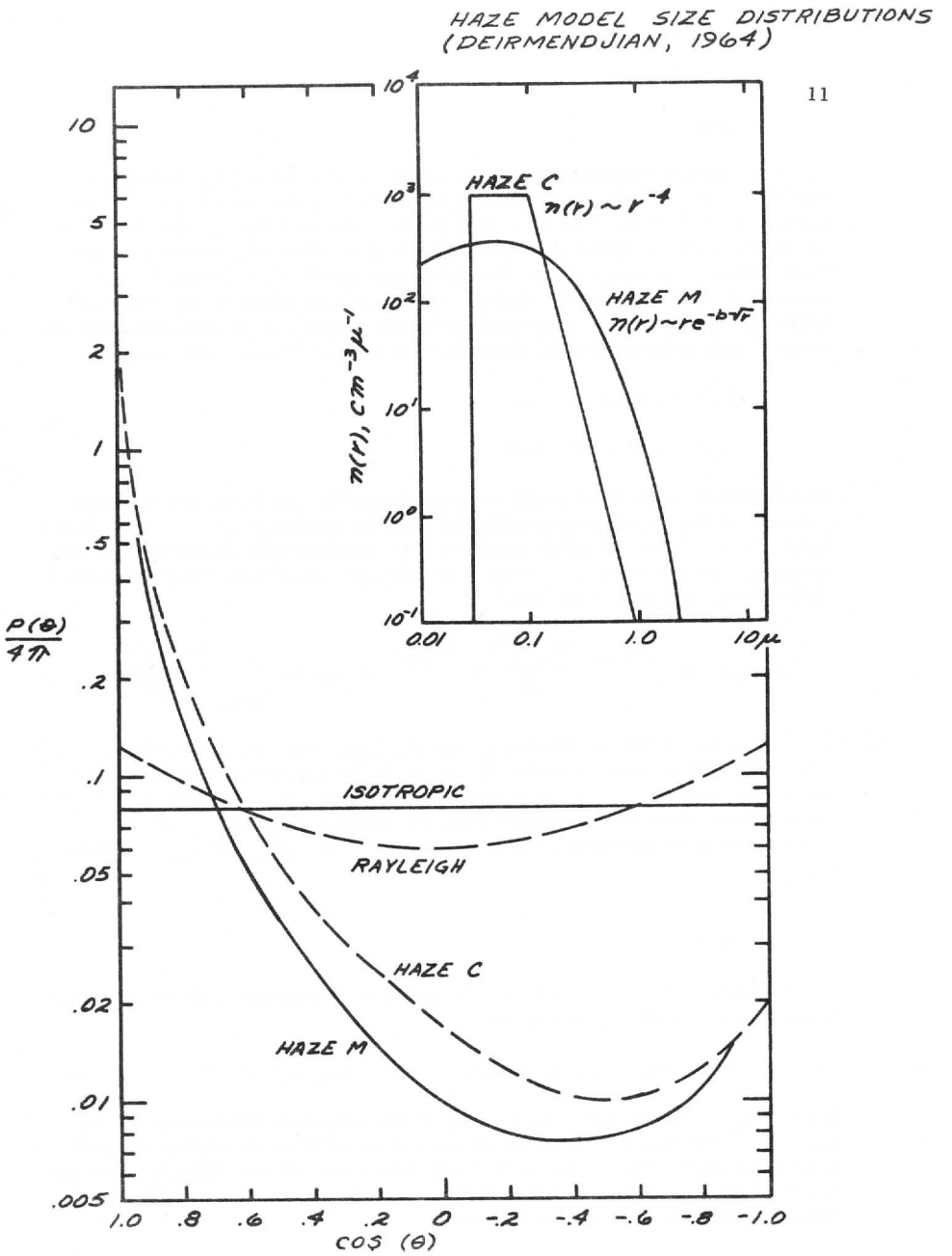

Figure 6. Aerosol and Rayleigh phase functions (from Kattawar and Plass, 1968). Haze models C and M (Deirmendjian, 1964) approximate the size distributions for continental and maritime haze, respectively.

2. Sea Light

The radiant intensity of light leaving the interior (or the effective scattering coefficient S_3) depends not only on the scattering in the interior but also on the character and depth of the underlying surface. Cox and Munk made an estimation of this term from their measurements, but their failure to account for scattering in the atmosphere between their plane at 2,000 feet and the surface makes interpretation of their results difficult. However, a rough estimate of this term can be obtained from the Monte Carlo calculations of Kattawar and Plass [9] which show that

$$\begin{aligned} S_3(\lambda = .46\mu) &\approx .01 \\ S_3(\lambda = .65\mu) &\approx .001 . \end{aligned} \tag{10}$$

This variation with wavelength is consistent with the order of magnitude increase of the absorption coefficient from its minimum at $\lambda = .46\mu$ to its value at $\lambda = .65\mu$. A crude model of this behavior can be made when the scattering cross-section is much less than the absorption cross-section. Under these conditions we have

$$S_3(\lambda, \theta) \approx \int_0^{Z_{max}} \frac{d\sigma_{scat}(\theta)}{d\Omega} e^{-2\beta_{ext} Z} n(Z) dz \propto \frac{1}{\beta_{ext}} \frac{d\sigma_{scat}(\theta)}{d\Omega} \tag{11}$$

where $d\sigma/d\Omega$ is the scattering cross-section, $n(Z)$ is the number of scatterers per unit volume at depth Z, β_{ext} is the extinction coefficient of sea water, and Z_{max} is the ocean depth. Since β_{ext} rapidly increases six or seven orders of magnitude into the infrared (Figure 7), we are led to expect a correspondingly rapid decrease in S_3 ($\beta_{ext} \approx \beta_{abs}$ in this case).

3. Sky Glint

According to Cox and Munk, the radiance of the sea surface due to reflected skylight (N') is given by

$$N' = \sec \mu \iint N_s \rho(\omega) \cos \omega \sec \beta \, p(Z_x, Z_y) \, dZ_x dZ_y , \tag{12}$$

where N_S is the radiance of the sky in the direction determined by Z_x and Z_y. The limits of integration are set to include all visible slopes. For near nadir observation ($\sec \mu \approx 1$) and using Eq. (4) for $P(Z_x, Z_y)$, the integrand in Eq. (12) becomes azimuthally symmetric about the zenith. Under these conditions, Eq. (12) reduces to

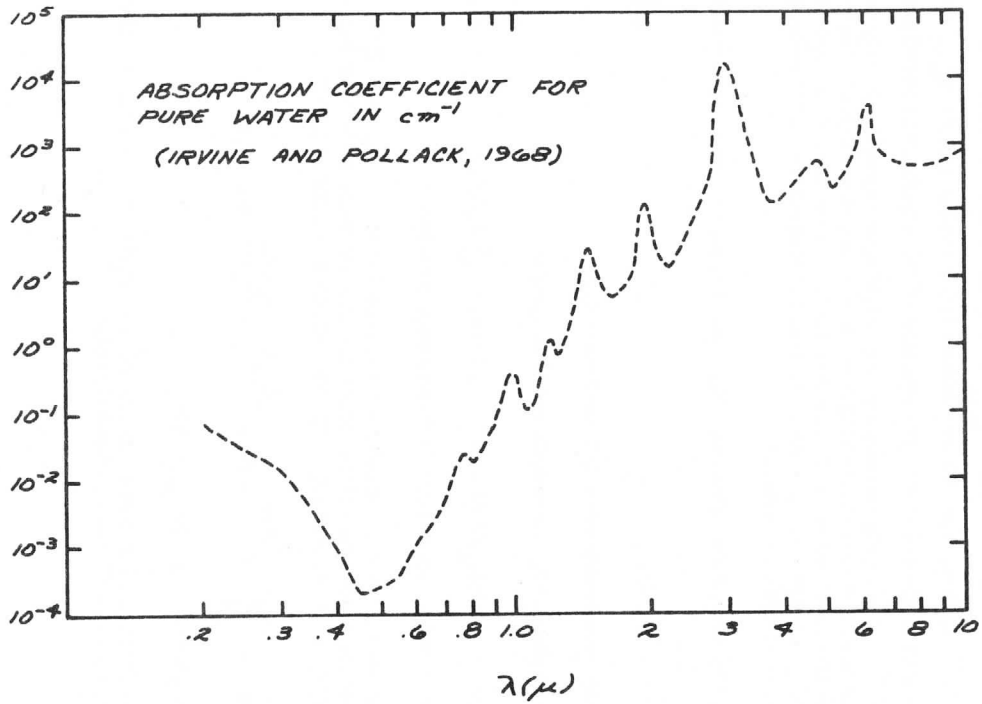

Figure 7. Wavelength dependence of the absorption coefficient for pure liquid water.

$$N' = \int_0^{\eta_{max}} \eta d\eta \frac{2}{\sigma^2} e^{-\eta^2/\sigma^2} \rho(\beta) N_s(2\beta)$$

where $\eta = \tan\beta$. The quantity η_{max} is usually somewhat less than $\tan \pi/4 = 1$. However, even for reasonably large winds, taking $\eta_{max} = \infty$ will not significantly affect Eq. (13) because of the exponential cutoff for large η^2/σ^2. Obviously the sea surface brightness depends not only on the sky radiance but also on its distribution as a function of zenith angle (which has the same value as β in this case). (Since $\rho(\beta)$ is a very weak function of β except near $\beta = 90°$, its angular dependence plays no role for a vertical viewing geometry.)

For a sky of uniform radiance, N_0, Eq. (13) may be integrated exactly to yield

$$N' = N_0 \rho(0°) \tag{14}$$

an eminently reasonable wind independent result.

For a Rayleigh sky the results are very similar:

$$N' = \rho(0°) N_s(0°)[1 + 4\sigma^4 + \ldots] \approx \rho(0°) \frac{\tau_R}{4\pi} P_R(0°) F \tag{15}$$

This shows a small but negligible dependence on wind.

For an aerosol sky the results are quite different. If τ_A and $P_A(\theta)$ are the aerosol scattering optical depth per unit air mass and phase function, respectively, then the aerosol component of the sky glint is given by

$$N' = \frac{2\tau_A \rho}{\sigma^2} \int_0^{\eta_{max}} \eta d\eta [e^{-\eta^2/\sigma^2}] \left[\frac{P_A(2\beta)}{4\pi} \sec 2\beta\right] F, \tag{16}$$

where $\rho = \rho(0°) \approx \rho(\beta)$ for $\beta \lesssim 30°$.

Using Diermendjian's haze model M for $P_A(\theta)$ at $\lambda = .7\mu$, we find the results expressed in the following table:

W(m/s)	σ	$\sigma N'/2\rho\,\tau_A F$
.006	.0577	.089
1.40	.100	.103
5.40	.173	.103
11.40	.245	.096

The mean behavior, for the indicated range of σ, is described by the relation

$$N' \approx \frac{2\rho\,\tau_A}{\sigma} C_\lambda F, \quad \text{haze model M,} \tag{17}$$

where $C_\lambda = .098$ at $\lambda = .7$. This relation does not hold at all wavelengths because $P_A(\theta)$ varies as well as τ_A (Figure 4)

In terms of scattering coefficients we may summarize these results as

$$S_2 = S_{2R} + S_{2a} \text{ where}$$

$$S_{2R} \approx \rho(0°) \frac{\tau_R}{4\pi} P_R(\mu) \tag{18}$$

$$S_{2A} \approx 2\rho(0°) \frac{\tau_A}{\sigma} [.098], \quad \lambda = .7\mu . \tag{19}$$

4. Foam Light

Using data reported by Woods Hole Oceanographic Institute and by the Visibility Laboratory of the Scripps Institute of Oceanography, Duntley has made an empirical fit for the fractional area of the sea surface covered by white water as a function of wind speed [10]. This is shown in Figure 8. To determine the surface radiance due to foam light we must also know the scattering properties of foam (or white water), which may depend upon the wind speed and perhaps other parameters as well. For lack of better information we shall assume that foam is a wavelength independent lambertian reflector with albedo one, which is very probably an overestimate of the scattering power of this source. Under these assumptions we have

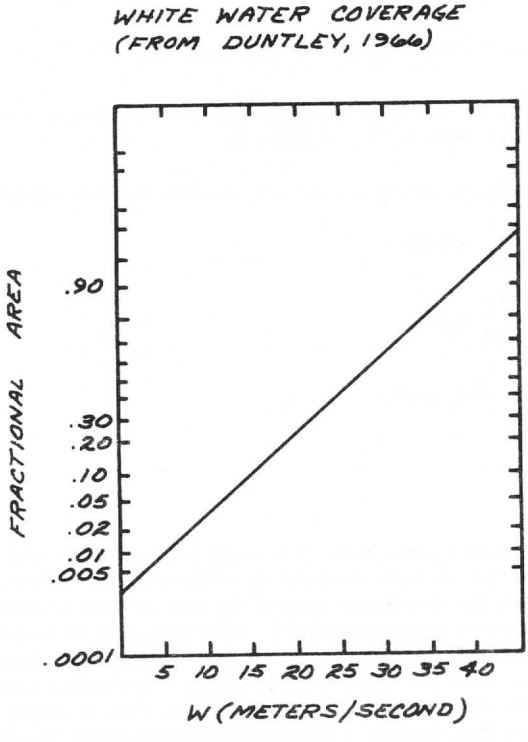

Figure 8. Fractional horizontal area of sea surface covered by white water (foam).

$$S_4 = \frac{f}{\pi} \cos \theta_s \qquad (20)$$

where θ_s = sun zenith angle and f is the fraction of horizontal area covered by foam. It should be noted that S_4 increases rapidly with increasing wind speed, while the sun glint scattering coefficient decreases with increasing wind speed. For high enough winds this source will thus become larger than the sun glint signal.

5. Black Body Radiation

In the absence of incident irradiance, the spectral radiance of a surface of emissivity ϵ_s at absolute temperature T is given by

$$N_B = \epsilon_s B(\lambda, T) = \epsilon_s \frac{c_1}{\lambda^5} [e^{c_2/\lambda T} - 1]^{-1}, \qquad (2\pi)$$

where $c_1 = 1.1909 \times 10^{-12}$ W cm^2 sterad^{-1} and $c_2 = 1.4380$ cm°K. The sea surface may be taken to have an emissivity of one, except when white water is significant. The black body radiation of the sea surface, which $\lambda = 10\mu$ is comparable to reflected solar radiation in the vicinity of $\lambda = 4\mu$. For much longer wavelengths this source is dominant, and for much smaller wavelengths it is negligible. This fact affords us the possibility of calibrating the sun glint by comparing it to the earth's black body radiance, provided the latter can be well determined from satellite (perhaps by measurements in the 10μ region). For a presentation of the concepts involved in such an experiment, see Reference 1.

Summary of Background

A useful summary of the relative sizes of the background sources and the sun glint is presented in Figure 9, which shows the wavelength dependence of all scattering coefficients for typical observing conditions. These conditions are taken to be: a surface temperature of 300°K, a wind speed of 5 m/s, and a vertical viewing geometry (the sun and satellite at the zenith of the observed point). In this figure it is the scattering coefficient at the center of the sun glint pattern which is plotted.

For the most part, skylight is the major source of background radiance. Beyond $\lambda = .7\mu$ sea light and Rayleigh sky glint are completely negligible. Beyond 4μ black body radiation becomes dominant. Atmospheric transmission factors have been included to show the relative background strengths

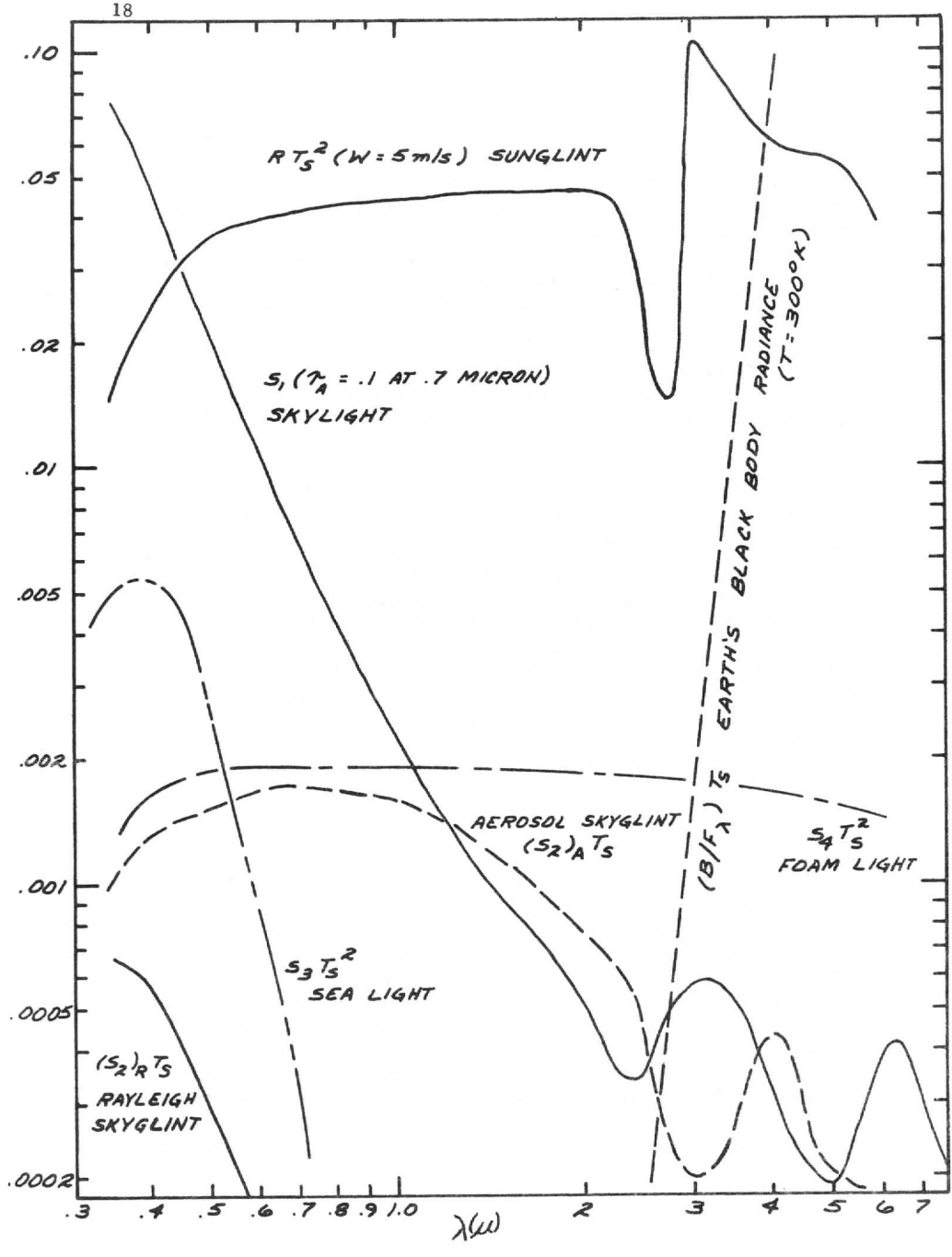

Figure 9. Graphic comparison of sun glint and background sources as a function of wavelength.

as viewed from a satellite. The description of these factors and how they influence sun glint measurements is dealt with in the following section.

The Generalized Sun Glint Experiment

As we have already seen, any measurement of the sun glint radiance contains radiance contributions from other sources. If one could make one measurement with the sun glint on and one with all conditions the same except that the sun glint is "turned off," the background could be removed by subtraction. A crude approximation to this method is to make one measurement at the peak of the sun glint and one where (or when) the sun glint is negligible. This implies two measurements for every sun glint determination.

If one is interested in the wavelength dependence of atmospheric transmission, at least two or more measurements are required—one at a reference wavelength λ, and one at the wavelength of interest λ'. This is necessary to reduce further the effects of background, or to "calibrate" the sun glint. Thus there are generally four measurements in a sun glint experiment: for each of two wavelengths, two measurements with different viewing geometries.

The two measurements with different geometries can be made in basically three different ways, each with its own deficiencies. These are:

a) Sun fixed, satellite fixed; measurements made at two different view angles (and thus at two different points on the surface).

b) Sun fixed, satellite moves; measurements made at two different view angles of the same point on the surface (and at two different times).

c) Satellite fixed, sun moves; measurements made at same view angles of same surface point at two different sun angles (and at two different times).

A diagrammatic presentation of these cases is made in Figure 10. Method a), which corresponds to taking a snapshot of the sun glint pattern, has the disadvantage of looking at two different points on the surface which, at satellite altitude, must be so far apart that local conditions (wind speed, for example) are very likely to be significantly different. In addition, background corrections are more difficult because two different air masses are in view (at different angles as well).

Methods b) and c) both have the advantage of viewing the same surface point. However, in b) different air masses are viewed, and in c) the incident flux travels through different air masses. In addition, c), which is

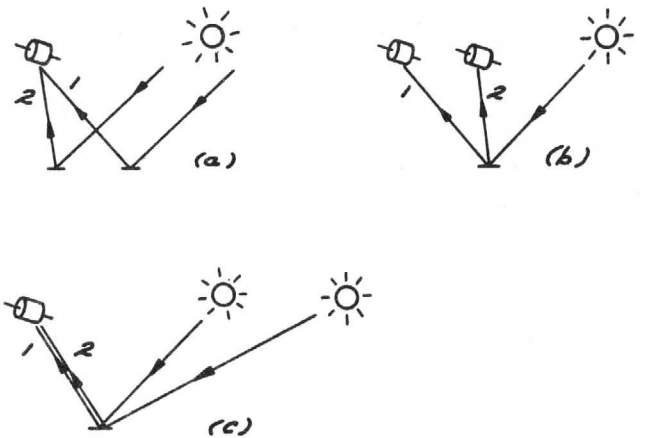

Figure 10. Sun Glint Experimental Geometries.

only possible for a geosynchronous platform, requires that measurements be separated in time by several hours, although Levanon's and Kornfield's work indicates that local variations in this time span are not generally significant.

Transmission Factors

The discussion of atmospheric attenuation, and the corresponding transmission factors, has been delayed until this point because it affects each source in a different way. We shall deal with two fundamentally different transmission factors:

1) T_s describes the attenuation due to scattering (from molecules and aerosols);

2) T_a describes the attenuation due to molecular band absorption. Since these are independent processes in the single scattering approximation, the net one-way transmission of the atmosphere is $T_s T_a$. For two-way transmission we shall use the notation T_{2s} and T_{2a}, in which case the net two-way transmission is $T_{2s} T_{2a}$. When the incoming and outgoing paths are identical (vertical viewing geometry, for example), $T_{2s} = T_s^2$; but $T_{2a} \neq T_a^2$ except for bands of weak nonoverlapping lines. The wavelength dependence of the scattering transmission factors is shown in Figure 11 for a colinear vertical viewing geometry.

Additional notation is needed to describe the effects of molecular absorption on directly-scattered light (i.e., skylight). For this we shall add the subscript s so that the appropriate transmission factors are T_{as} for skylight seen from above, and T_{2as} for skylight reflected by the sea surface. The actual effective optical paths in these cases depend upon the relative optical thicknesses of the Rayleigh and Mie scatterers and their distributions in altitude.

We are now in a position to write down the expressions for the four radiances measured in a general satellite sun glint experiment. These are

$$N_1 = [T_{as} S_1 + T_s T_{2as} S_2 + T_{2s} T_{2a} (S_3 + S_4 + R)]F + T_s T_a B \tag{22}$$

$$N_1' = [T'_{as} S'_1 + T'_s T'_{2as} S'_2 + T'_{2s} T'_{2a} (S'_3 + S'_4 + R')]F' + T'_s T'_a B' \tag{23}$$

$$N_2 = [T^{(2)}_{as} S^{(2)}_1 + T^{(2)}_s T^{(2)}_{2as} S^{(2)}_2 + T^{(2)}_{2s} T^{(2)}_{2a} (S^{(2)}_3 + S^{(2)}_4 + R^{(2)})]F + T^{(2)}_s T^{(2)}_a B^{(2)} \tag{24}$$

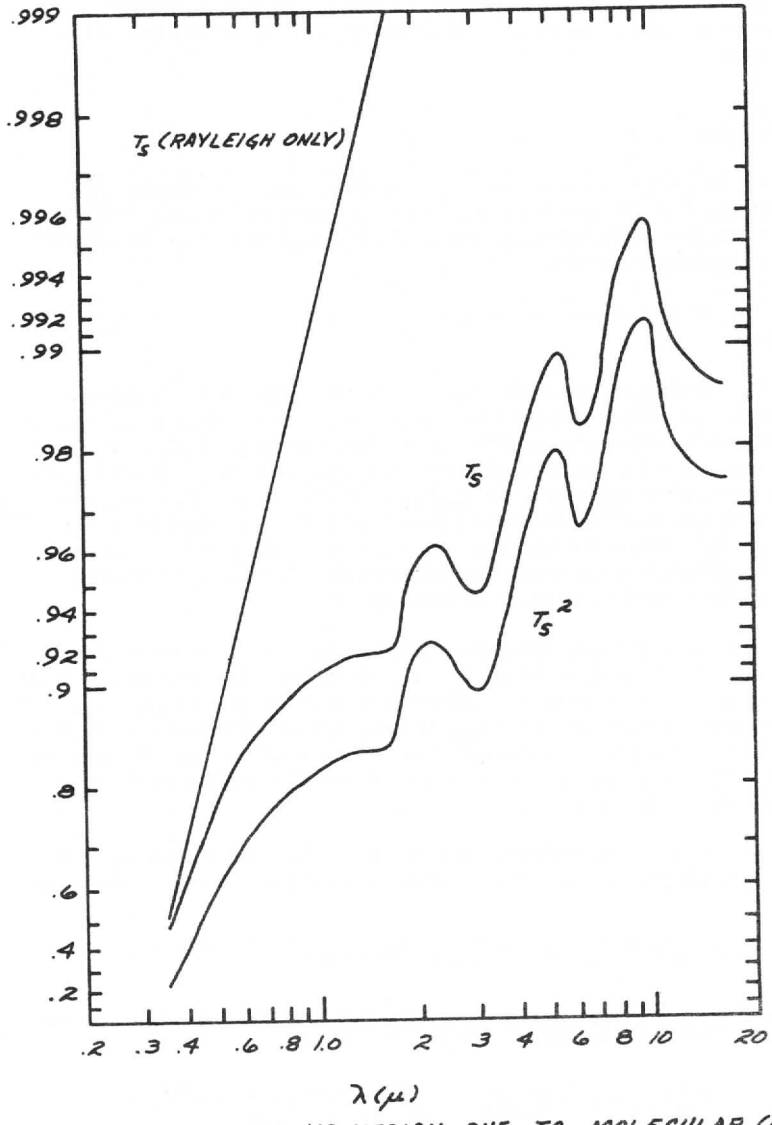

Figure 11. Scattering Transmission Factors.

$$N_2' = [T_{as}^{(2)'} S_1^{(2)'} + T_s^{(2)'} T_{2as}^{(2)'} S_2^{(2)'} + T_{2s}^{(2)'} T_{2a}^{(2)'} (S_3^{(2)'} + S_4^{(2)'} + R^{(2)'})]F' + T_s^{(2)'} T_a^{(2)'} B^{(2)'} \quad (25)$$

where the unprimed measurements are at wavelength λ and the primed at wavelength λ'. Given F and F' we have four equations in fifty-four unknowns. It is obvious that we cannot determine all these factors from satellite-based measurements. However, since the backgrounds are generally small compared to the sun glint, even a relatively crude model for their angular and wavelength dependence can be used to reduce the number of unknowns to a manageable level. The details will be discussed for four separate experiments designed to measure distinctly different parameters.

Determination of R

As an example of techniques which can be used in the visible and near-infrared spectral regions, we shall consider the problem of measuring wind speed from geosynchronous altitude using method c). Actually R is measured and from this the wind speed is determined from Eq. (1) and (3).

Avoiding regions of ozone absorption and molecular band absorption, we may assume $T_a = 1$ and $B = 0$ for $.4\mu \leq \lambda \leq 2.5\mu$. The spectral radiance measurements at two different sun angles are then

$$N_1 = [S_1 + T_s S_2 + T_{2s}(S_3 + S_4 + R)]F \quad (26)$$

$$N_2 = [S_1^{(2)} + T_s^{(2)} S_2^{(2)} + T_{2s}^{(2)} (S_3^{(2)} + S_4^{(2)} + R^{(2)})]F . \quad (27)$$

Let us assume that the second measurement is made at a sun angle sufficiently large so that $R^{(2)} = 0$, and also that the satellite is at the zenith of the observed point. We may also assume that $S_{2A}^{(2)} = 0$. (Because of the highly-peaked forward scattering of aerosols, if the sun's image is out of view, the aureole's image will be also.) Under these conditions, Eq. (26) and Eq. (27) become

$$N_1 = [S_1 + T_s S_{2R} + T_s^2 (S_3 + S_4)]F + [T_s S_{2A} + T_s^2 R]F \quad (28)$$

$$N_2 = [S_1^{(2)} + T_s S_{2R}^{(2)} + T_s T_s^{(2)} (S_3^{(2)} + S_4^{(2)})]F . \quad (29)$$

For reasonably small sun angles $S_1^{(2)}$, $S_{2R}^{(2)}$, $S_3^{(2)}$, $S_4^{(2)}$ are all approximately linear in the cosine of the sun zenith angle. Furthermore, if the optical depth per unit air mass τ is not close to unity $T_s^{(2)}$ will not be much different from T_s. Thus it is reasonable to suppose that we can find a geometrical function $f(1, 2)$ which relates the backgrounds at two different sun angles, i. e.

$$[S_1^{(2)} + T_s S_{2R}^{(2)} + T_s T_s^{(2)}(S_3^{(2)} + S_4^{(2)})] \approx f(1,2)[S_1 + T_s S_{2R} + T_s^2(S_3 + S_4)] \tag{30}$$

(In the case we are discussing, $f(1, 2) \approx \cos(\theta_S)$, where θ_S is the solar zenith angle of the observed point.) Using Eq. (30) it becomes possible to subtract out most of the background terms, i. e.

$$\frac{1}{F}\left[N_1 - \frac{1}{f(1,2)} N_2\right] = T_s S_{2A} + T_s^2 R \tag{31}$$

Since both the sun glint and aerosol sky glint peak at the specular point and fall off rapidly away from this, we have been unable to separate these two components, as shown in Eq. (31). In principle, a detailed study of the angular distribution of the left-hand side of Eq. (31) away from the specular point should make this distinction possible. However, there are some practical difficulties in doing this. Since S_{2A} is relatively small compared to R, the difference between the angular distribution of $T_s^2 R$ and that of $T_s S_{2A} + T_s^2 R$ may very well be negligible, especially in view of the difficulty in determining what the angular dependence of RT_s^2 ought to be.

In the Cox and Munk model (Eq.(1)) knowing the peak value of R determines its angular distribution. However, we cannot directly measure the peak value because of the contamination of aerosol sky glint. Furthermore, since Cox and Munk observed at an altitude of 2, 000 ft and made no explicit correction for aerosols, it is only reasonable to assume that their model itself contains the aerosol sky glint term for an unknown aerosol optical thickness τ_A. Thus, in using the Cox and Munk model to determine winds, it is probably more reasonable to use, instead of Eq. (31), the expression

$$T_s^2 R_{c.m.} = \frac{1}{F}\left[N_1 - \frac{1}{f(1,2)} N_2\right] \tag{32}$$

where

$$R_{c.m.} = \frac{1}{T_s} S_{2A} + R . \tag{33}$$

Note that in principle R is independent of τ_A, while $R_{c.m.}$ depends on τ_A, and thus the two-dimensional gaussian model for $R_{c.m.}$ (which we previously used for R) cannot be expected to hold if τ_A is significantly different from the aerosol optical thickness typical of the Cox and Munk measurements (which is not known). From our knowledge of τ_R and a reasonable estimate of τ_A we can estimate T_s^2 and thus $R_{c.m.}$ (and the wind speed). In principle this description applies to the methods used by Kornfield to correct for background. His results attest to the feasibility of the technique applied to ATS-I measurements.

Determination of Aerosol Extinction

We shall now consider a technique for using the sun glint to measure that component of Ts due to aerosols. Since the Rayleigh optical depth $\tau_{R,\lambda}$ can be calculated, a measurement of $Ts = \exp(-\tau_{R,\lambda})\exp(-\tau_{A,\lambda})$ determines $\tau_{A,\lambda}$, the aerosol optical depth (or extinction coefficient per unit air mass). Consider four measurements, two of the type just described at each of two wavelengths λ, λ'. After the background subtraction techniques (Eq. (31)) are employed, we have the two equations

$$T_s^2\left(\frac{1}{T_s} S_{2A} + R\right) = A \tag{34}$$

$$T'_{2a}T'^2_s\left(\frac{T'_{2as}}{T'_{2a}T'_s} S'_{2A} + R'\right) = A', \tag{35}$$

where A and A' are known from measurements at λ and λ'.

Since $R/R' = \rho_\lambda/\rho'_\lambda$ we may eliminate R and R' from this pair of equations to obtain

$$\frac{T'^2_s}{T_s^2} = \frac{\rho_\lambda}{\rho_{\lambda'}} \frac{A'}{A}\left[\frac{1 - T'_s \frac{S'_{2A}}{A'}}{1 - T_s \frac{S_{2A}}{A}}\right] \tag{36}$$

The contributions from aerosol skylight, S_{2A} and $S_{2A'}$, are typically of the order of a few percent of R (Figure 9). Thus we may neglect second

order products of S_{2A}/A and S_{3A}/A' compared to one. Employing Eq. (17) and (19) also, we may write Eq. (36) as

$$e^{-x} \approx \alpha[1 - x\beta + O(10^{-3})], \tag{37}$$

where

$$x = -2(\tau_A - \tau'_A)$$

$$\alpha = \frac{\rho_\lambda A'}{\rho_{\lambda'} A} e^{-2(\tau_R - \tau'_R)}$$

$$\beta = \frac{1}{\sigma}\left[\frac{\rho_\lambda C_\lambda e^{-(\tau_R + \tau_A)}}{A}\right]_{\text{mean}} \tag{40}$$

The mean indicated is for the two wavelengths λ and λ'. The reflectivities ρ_λ and $\rho_{\lambda'}$ can be obtained from Figure 3. The sea surface slope distribution width σ can be obtained approximately (probably better than 10% accuracy) from Eq. (34) or Eq. (35), even neglecting S_{2A}. The factor C_λ depends on the haze model used (or observed) as well as wavelength, but can probably be estimated to within 10-20%. Since τ_A is of the order of 0.1, the mean of $e^{-\tau_A}$ can be estimated probably to within 10% or 20%. The Rayleigh optical depths are assumed to be well known.

Neglecting for the moment the possible measurement errors in A' and A the major source of error is due to uncertainties in β which may be of the order of 30% or more. Even if uncertainties are considerably larger than this, they may be reduced to this level or below through iteration of Eq. (37). The effect of this uncertainty in β on the determination of X may be obtained from Eq. (37) by differentiation.

$$\frac{dX}{X} = \frac{d\beta}{\beta}\left[\frac{1}{\frac{1}{\alpha\beta}e^{-X} - 1}\right] \tag{39}$$

Under the observing conditions for which Figure 9 applies $\alpha\beta \approx \beta \approx .04$ and $X \approx .1$. Thus we have

$$\frac{dX}{X} \approx \frac{d\beta}{\beta} \times .05, \tag{40}$$

which means that a 30% error in β results in a 1.5% error in X. This would correspond to changes in aerosol optical thickness as function of

wavelength of about .002 out of .1. Even a factor of two error in β would lead to an error in $\tau_A - \tau_A'$ of only .005 (or 5%). Thus we see that any reasonable uncertainty in β will not lead to significant errors in the determination of $\tau_A - \tau_A'$. Errors resulting from imperfect background subtraction, spectral radiance measurement errors, and, in some cases, uncertainties in the ratio $\rho_\lambda/\rho_\lambda'$ will be most significant.

Returning to equations (28) through (31), we may estimate the effects of uncertainties in the background subtraction techniques. This effect is most important in the visible region of the spectrum since the background is largest there (Figure 10). For our standard observing conditions (those for which Figure 10 applies), the total background contribution other than aerosol skylight is roughly 25% of RT_s^2 at $\lambda = .6\mu$. At $\lambda' = 1.0\mu$ this amounts to only about 3%. If the function $f(1, 2)$ which relates the backgrounds at two different observing geometries (Eq. (30)) describes background variations only to within 10% of the total background (which is a considerable error), the effect would show up on the right-hand side of Eq. (31) as 2.5% radiance change at $\lambda = .6\mu$ and .3% change at $\lambda' = 1.0\mu$. For the two wavelengths chosen as examples here, this effect could be seen in Eq. (38) as a 3% (approximately) error in α. Taking differentials of X and α we find (ignoring β variations) that

$$dX \approx d\alpha \tag{41}$$

Since $\alpha \approx 1$, a 3% error in α corresponds to $d\alpha \approx .03$, and similarly the error in $X = \tau_A - \tau_A'$ is approximately .03 out of .1, or about 30%. This may seem like a large error, but this can still be useful in detecting large changes in aerosol concentration (which are quite frequent) [6]. It is also likely that errors in background subtraction will be considerably smaller than we have assumed here.

The effect of errors in the spectral radiance measurements are related to the error in X through Eq. (31), (34), (35), (36), (37), and finally (41). We have, neglecting the other errors present,

$$dX \approx d\alpha \approx 4\frac{dN}{N} \tag{42}$$

where dN/N is the average percentage r. m. s. error for the four radiances used in these computations. Thus a 1% error in radiance measurements produces an error in $X = \tau_A - \tau_A'$ of approximately .04 out of a probable variation of .1 (from λ to λ'). This indicates that instrumental requirements will be severe. We hope to deal with this aspect of the problem in a later report.

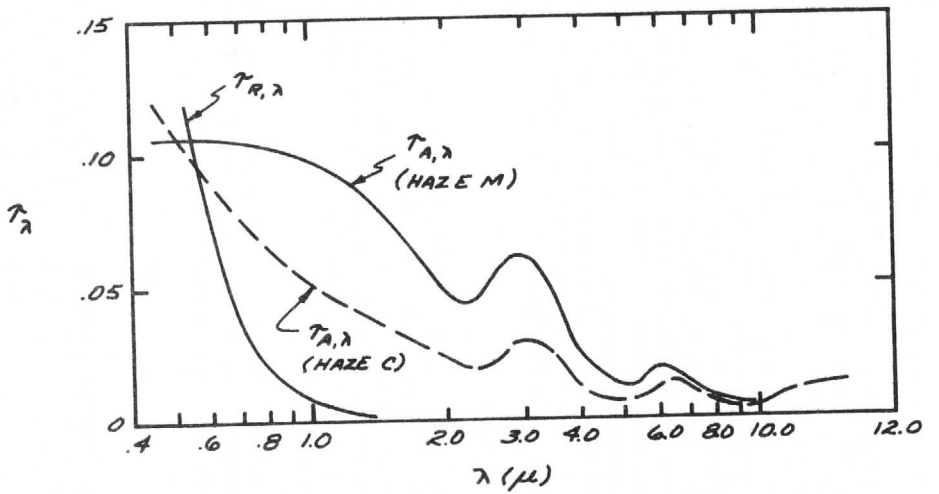

Figure 12. Aerosol and Rayleigh extinction coefficients as a function of wavelength (Deirmendjian, 1964). Haze C and haze M are as in Figure 6.

Thus we conclude that measurement of aerosol optical thickness changes with wavelength ($\tau_A - \tau_{A'}$) is theoretically feasible using the sun glint. For typical observing conditions (Figure 10), this change should be measurable to within .02 to .03 if adequate instrumentation is available (spectral radiance measurement error no greater than about .25%).

Determination of $\tau_{A,\lambda} - \tau_{A,\lambda'}$ does not, of course, determine the absolute values of either $\tau_{A,\lambda}$ or $\tau_{A,\lambda'}$. To determine this directly, an absolute calibration of the sun glint would be required. Since this presents considerable difficulties, it is fortunate that there are indirect methods. First, one can choose λ' large enough to insure that $\tau_{A,\lambda'}$ is small on theoretical grounds (Figure 12) and then $\tau_{A,\lambda} - \tau_{A,\lambda'}$ is very nearly $\tau_{A,\lambda}$. This works better for large values of τ than for small values, and also better for haze C than for haze M. This can be improved on by using the wavelength dependence of $\tau_{A,\lambda} - \tau_{A,\lambda'}$ to identify the type of aerosol and use theory than to estimate the absolute size of $\tau_{A,\lambda}$ from the size of the wavelength variations. Of course, one must be careful to measure over a wavelength range in which significant variations of τ_λ can be expected for those aerosols which one is attempting to detect.

Near-Infrared Measurements of Molecular Band Absorption

In discussing this region of the spectrum we shall assume a near-vertical viewing geometry and a geosynchronous platform, as before. From the results displayed in Figure 9 we may make the following approximations

$$S_{2R} = S_3 = B = 0 \tag{43}$$

for $.6\mu \leq \lambda \leq 2.5\mu$. Making the previously discussed background subtraction measurements at two different wavelengths (both in the infrared region) we have

$$\frac{1}{F}\left(N_1 - \frac{1}{f(1,2)} N_2\right) = T_s T_{2as} S_{2A} + T_{2s} T_{2a} R \tag{44}$$

$$\frac{1}{F'}\left(N'_1 - \frac{1}{f'(1,2)} N'_2\right) = T'_s T'_{2as} S'_{2A} + T'_{2s} T'_{2a} R' \tag{45}$$

where we have assumed

$$R^{(2)} = R^{(2)'} = 0 \tag{46}$$

$$S_{2A}^{(2)} = S_{2A}^{(2)'} = 0 \tag{47}$$

$$T_{as}^{(2)} S_1^{(2)} = f(1,2) T_{as} S_1 \tag{48}$$

$$T_{as}^{(2)'} S_1^{(2)'} = f'(1,2)\, T'_{as} S_1' , \tag{49}$$

and also a reasonably accurate knowledge of f and f'.

We shall now consider the problem of using the set of measurements (41) and (42), to determine the absorption at the center of molecular band, specified by λ'. We shall assume that T_{2a} and T_{2as} are both unity at the reference wavelength λ. Furthermore, since the forward scattered radiation traverses nearly the same atmospheric path as the unscattered radiation, we may assume that $T'_{2a} = T'_{2as}$. Under these assumptions and conditions, (41) and (42) become

$$X = T_s^2 R + T_s S_{2A} \tag{50}$$

$$X' = T'_{2a}(T_s^{2'} R' + T'_s S'_{2A}) \tag{51}$$

where X and X' are the left-hand sides of (41) and (42), respectively. Solving this system for the absorption at wavelength λ', we have, assuming $\rho_\lambda \approx \rho_{\lambda'}$,

$$A_{2,\lambda'} = 1 - T'_{2a} = \frac{\left[\frac{T_s^{2'}}{T_s^2} X - X'\right] + \frac{T'_s}{T_s}\left[T_s S'_{2A} - T'_s S_{2A}\right]}{\frac{T_s^{2'}}{T_s^2} X + \frac{T'_s}{T_s}\left[T_s S'_{2A} - T'_s S_{2A}\right]} \tag{52}$$

where the subscript (2) on $A_{2,\lambda'}$ refers to the double traversal of the atmosphere. Let us assume at this point that Rayleigh scattering is negligible in influencing T_s and T'_s. In most cases in the infrared the aerosol sky glint component $T_s S'_{2A} - T'_s S_{2A}$ may be neglected relative to either X or X' (Figure 10). However, the difference $(T_s^{2'}/T_s^2)X - X'$ may not be large compared to the sky glint term. This arises when the fractional absorption at λ' is small compared to one. The smallest absorption that can be

measured thus depends upon the size of the scattered background and on how well it can be estimated. For the case in which λ is very close to λ' and $T_s/T'_s \approx 1$, Eq. (49) takes the simpler form

$$A_{2,\lambda'} = \frac{X - X'}{X} . \tag{53}$$

For $\lambda = 1.0\mu$, $\lambda' = .94\mu$ and with $f(1,2)$ accurate to 10%, we find that the absorption (due to water vapor in this case) for a double traversal of the atmosphere is related to the quantities X and X' by

$$A_{2,\lambda'} = \frac{X - X'}{X} - .009\frac{X'}{X} \pm .015 . \tag{54}$$

Thus we could use (50) without a significant loss of accuracy and obtain the water vapor absorption to within approximately .02, which is an adequate sensitivity to be useful (changes greater than .25 precipitable cm. could be observed with a spectrometer of .03μ resolution). It appears that water vapor absorption measurements from a satellite using the sun glint are easily feasible.

Calibration at 4μ

We have already noted that the sun glint and earth's black body spectral radiances are comparable near $\lambda = 4\mu$. It has been suggested that since this region is also an atmospheric window, a measure of the sea surface temperature (which determines B) could be used to calibrate the sun glint (McClintock, 1970) [11]. Measurements of B ($\lambda = 10\mu$) from a satellite can be used to infer B ($\lambda = 4\mu$) through Planck's equation. At $\lambda = 4\mu$ equations (20) and (22) reduce to

$$N_1 = [T_{as}S_{1A} + T_sT_{2as}S_{2A} + T_{2s}T_{2a}(S_4 + R)]F + T_sT_aB \tag{55}$$

$$N_2 = [T^{(2)}_{as}S^{(2)}_{1A} + T^{(2)}_{2s}T^{(2)}_{2a}S^{(2)}_4]F + T^{(2)}_sT^{(2)}_aB \tag{56}$$

where we have assumed a geometry such that $R^{(2)} = S^{(2)}_{2A} = 0$, and a sea surface emissivity which is independent of view angle. We may also assume that $T_{2s} = T_s^2$ and $T_{2as} = T_{2a}$, the latter applying best for a near-vertical viewing geometry. Dividing by F we thus have

$$N_1/F = [T_a S_{1A} + T_s T_{2a} S_{2A} + T_s^2 T_{2a}(S_4 + R)] + T_s T_a B/F \quad (57)$$

$$N_2/F = [T_a^{(2)} S_{1A}^{(2)} + T_s^{(2)2} T_{2a}^{(2)} S_4^{(2)}] + T_s^{(2)} T_a^{(2)} B/F \quad (58)$$

How we proceed from here depends on the size of the background terms. For $W \leq 2m/sec$ and $\tau_A \leq .1$ the background term (in brackets) is less than 1% of the sun glint signal or B/F. In this case, (52) and (53) reduce to

$$X_1 = N_1/F = T_s^2 T_{2a} R + T_s T_a B/F \quad (59)$$

$$X_2 = N_2/F = T_s^{(2)} T_a^{(2)} B/F \quad (60)$$

Solving this system for R in terms of the known quantities $X_1, X_2, B,$ and F we have

$$R = \frac{[T_s^{(2)} T_a^{(2)}]^2}{T_s^2 T_{2a}} \left[X_1 - \frac{T_s T_a}{T_s^{(2)} T_a^{(2)}} X_2\right] \frac{(B/F)^2}{X_2^2} \quad (61)$$

Because of the low wind speed assumed here the sun glint pattern is very small. Thus the viewing geometries 1 and 2 may be taken close enough together to assume $T_s^{(2)} = T_s$ and $T_a^{(2)} = T_a$. Then (58) reduces to

$$R_{\lambda=4\mu} = \frac{T_a^2}{T_{2a}} [X_1 - X_2] \frac{B^2}{X_2^2 F^2} \quad (62)$$

The ratio T_a^2/T_{2a} is a few percent larger than unity and can probably be approximated to within 1%. Assuming all measured quantities are absolutely accurate, our assumptions (required by ignorance) led to an error of approximately one or two percent in the value of R at $\lambda = 4\mu$. While this appears to be usable, a number of practical problems must also be considered.

(1) Sea surface emissivity variations with wavelength may interfere with determination of B $(\lambda = 4\mu)$ from B $(\lambda = 10\mu)$.

(2) Even without relative emissivity variations the percent error in B $(\lambda = 4\mu)$ inferred from B $(\lambda = 10\mu)$ is 2.5 times the percent error in B $(\lambda = 10\mu)$.

(3) Current uncertainty in the wavelength dependence of $\rho_\lambda(\omega)$ is relatively large in the 4μ region ($\sim$ 5%) (Figure 3) and degrates the accuracy of the calibration at other wavelengths.

Adding to these factors, instrumental limitations may make this method of sun glint calibration completely unworkable. The usefulness of transmission measurements of 5% accuracy (assuming perfect instrumentation) is questionable in itself.

Conclusions

We have attempted to present here a detailed framework of analysis for estimating the feasibility of sun glint experiments, specifically concentrating on the effect of uncertainties in theory on possible determinations of atmospheric transmission and absorption. Accurate evaluation of experiments depends on the particulars in the method and in the instrumentation. We have not dealt with the latter factors in detail in the report.

We have found that the sun glint can be used without absolute calibration to determine the following:

1) changes of aerosol optical thickness with wavelength with an accuracy of approximately .02 to .03 in optical depth from the visible to near $\lambda = 2.5\mu$ wherever atmospheric windows permit;

2) molecular band absorption for a two-way traversal of the atmosphere with an accuracy of approximately .02 in fractional absorption. (This could be very useful in determining precipitable water vapor from satellites.)

We have found that the above determination can probably not be improved by calibrating the sun glint at $\lambda = 4\mu$, since the errors in this calibration are very likely to be too large for the calibration to be useful.

These conclusions are applicable for the observing conditions we have specified as typical. Included in this specification is a wind speed of 5 m/s. For lower wind speeds the accuracies cited will be conservative. For higher wind speeds the suggested determinations will at some point no longer be feasible. Significant variations of viewing geometry and aerosol loading will also modify these conclusions to varying degrees. To describe the effects of all possible variations of the numerous parameters involved in this study would introduce a degree of complexity which would produce, at this point, more confusion than enlightenment. Instead we have

examined a small, but very probable, region of the multidimensional space of variations and have concluded that the sun glint shows promise as an experimental tool for the determination of atmospheric transmission and absorption.

References

1. Cox, Charles C. and Walter Munk, "Measurement of the Roughness of the Sea Surface from Photographs of the Sun's Glitter," J. Opt. Soc., Am. 44, 838 (1954).

2. Levanon, N., "Determination of the Sea Surface Slope Distribution and Wind Velocity Using Sun Glitter Viewed from a Synchronous Satellite," Meteorological Satellite Instrumentation and Data Processing, Final Scientific Report on NASw-65 (1968).

3. Kornfield, J., Ph.D. thesis, University of Wisconsin, Madison, unpublished (1971).

4. Friedman, D., "Infrared Characteristics of Ocean Water (1.5 - 15μ)," Applied Optics, 8, 2073 (1969).

5. Coulson, Dave and Sekera, Tables Related to Radiation Emerging from a Planetary Atmosphere with Rayleigh Scattering, Univ. of California Press (1960).

6. Volz, F. E., "Spectral Skylight and Solar Radiance Measurements in the Caribbean: Maritime Aerosols and Sahara Dust," J. Atmos Sci., 27, 1041 (1970).

7. Quenzel, H., "Determination of Size Distribution of Atmospheric Aerosol Particles from Spectral Solar Radiation Measurements," J. Geophys. Res., 75, 2915 (1970).

8. Deirmendjian, D., "Scattering and Polarization Properties of Water Clouds and Hazes in the Visible and Infrared," Applied Optics, 3, 187 (1964).

9. Plass, G. N. and G. W. Kattawar, "Radiative Transfer in an Atmosphere-Ocean System," Applied Optics, 8, 455 (1969).

10. Duntley, S. Q. and C. F. Edgerton, The Use of Meteorological Satellite Photographs for the Measurement of Sea State, U. S. Navy, Bureau of Ships, Project FAMOS, Contract NObs-86012 Lot 11, Final Report No. 11-2 (1966).

11. McClintock, M., T. A. Hariharan, and A. McLellan IV, "Studies on Techniques for Satellite Surveillance of Global Atmospheric Pollution," annual report to the National Air Pollution Control Administration, UWI-SSEC-GAP-70-001, September 30, 1970.

Additional Bibliography

Irvine, William M. and James B. Pollack, "Infrared Properties of Water and Ice Spheres," ICARUS, 8, p. 324-360 (1968).

Pontier, L. and C. Dechambenoy, Annals of Geophysics, 633 (1966).

THE USE OF CUMULONIMBUS ANVIL GROWTH DATA FOR INFERENCES ABOUT THE CIRCULATION IN THUNDERSTORMS AND SEVERE LOCAL STORMS

B. Auvine and C. E. Anderson

Abstract:

The cumulonimbus anvil, studied by means of geosynchronous satellite, is used to reveal the circulation characteristics of local storms. Data is given for volume flux and divergence at the top of the storm, and these are compared with previous results by other investigators. Agreement is good, suggesting that satellite study of local storms is both useful and reliable. In regard to thunderstorm anvil outflow, a simple model of a point source in a uniform stream is shown to be a close approximation to observed anvil growth. Some evidence suggesting the interaction of proximate local storms with one another and with the environmental wind shear is presented.

Introduction

The cumulonimbus anvil, an easily detectable feature of a growing thunderstorm, has come to be used by many investigators as a means of studying the circulation characteristics of local storms. These characteristics include the updraft velocities and the upward fluxes of mass, volume and energy in the main storm column, as well as the rate of storm growth and development. Before proceeding to illustrate the use of the anvil in such studies, we should note here for purposes of later comparison the general methods utilized in previous investigations of thunderstorm fluxes.

Such methods can be divided into three main groups: those relying on terrestrial or aerial photogrammetic techniques, those using aerial or ground-based instrumental means, and those employing the use of a geosynchronous

satellite such as ATS-III. The first of these techniques has been used successfully by Anderson (1960), who was able to deduce the volume fluxes in a storm by photographically measured cloud anvil growth, by Reuss (1961), who determined the volume, height, vertical velocities, and a movement of a storm by means of a series of anvil photographs, and by Fujita and Byers (1962), who used photogrammetry to determine the updraft intensity and detailed structure of a storm.

Instrumentation has also proved useful in studying the cumulonimbus. Research tools have ranged from aircraft (Fujita and Arnold, 1963) and rawinsonde (Newton, 1966), to radar anvil studies by Hitschfeld (1960).

Finally, and most recently, we have the satellite as a means of quantitatively measuring severe storm circulation. Work in this area has been done primarily by Fujita and Bradbury (1968) and Ninomiya (1971) (mass fluxes and divergence at anvil level deduced from upper level cloud motions) and Sikdar (1969), whose method of measuring anvil growth was used in our own study.

It is the intent of this paper to show that this latter means is a reliable method of studying severe local storm circulation, even in areas from which no data other than satellite photographs are available. This will be done, first, by comparing our own results with those of others, and, second, by showing that satellite data is capable of resolving certain other characteristics of severe storm circulation not ordinarily apparent from conventional data.

Data Analysis Techniques

According to Sikdar's model (1970), expansion of cumulonimbus cloud tops aloft in the form of an anvil should be the direct result of convergence at the surface, vertical motion, and subsequent divergence at the top of the convective towers. Implicit in such a model is the question of what proportion of the upward convected air finds its way into the outflow layer. We know that for well-developed storms, a considerable amount of air is involved in the cold downdraft (about 60% of the updraft volume according to Newton) and it is necessary to know the source of this air. Newton (1966) argues that the downdraft is air whose origin is in the mid-troposphere, based on equivalent potential temperature observations and thus his conclusion is that "essentially all the air originating in the updraft remains in the upper troposphere, spreading out mainly in the anvil plume downshear but appreciably also on the upshear side." The mid-tropospheric origin of the cold downdraft finds some observational support by Fankhauser (1968) who found that chaff distributed upwind from a storm is incorporated within the storm at the 500 mb level.

Newton's work used the concept of a steady-state storm and he employed the tilted updraft model proposed by Bates (1961) and Browning (1963). A recent study by Dennis et al. (1970) raises some doubts as to the applicability of this model to the hailstorms observed in northeast Colorado and South Dakota. Dennis found that new cell development in the form of feeder clouds at the trailing edge seemed to characterize the majority of hailstorms of the northern Great Plains. In these storms, he feels the appropriate model is that suggested by Byers and Braham (1949), wherein the formation of precipitation within the updraft acts as a brake and eventually leads to the collapse of the individual cell. New cell formation acts to perpetuate the storm as an entity. Thus this mode of behavior should lead to quasi-periodic variations in the anvil growth, but such periodic growth does not invalidate the argument that the air in this anvil originates from lower tropospheric air. A recent study by Sikdar et al. (1970), using ATS-III satellite data taken at fourteen-minute intervals of tornado-producing severe storms over Oklahoma and adjacent regions on April 19, 1968 (see figure 1), does show that at least on this occasion one could not characterize these storms as steady state. One can draw similar conclusions from Newton and Bates's (1960) radar observation of a pulsating storm and the report of Knoll et al. (1959) describing a pulsating anvil in a very large storm.

If we accept the concept that the anvil expansion is a legitimate tool for measuring the volume flux in a storm or a group of storms, we may proceed to examine how such an anvil expansion may be measured. While one may, of course, attempt to measure the rate of anvil expansion by eye directly from the satellite photograph, a far more accurate method of measurement consists of using the digitized satellite tapes to produce a computer plot of the isopleths of equal brightness (figure 2). Such a plot gives a detailed portrait of the anvil and by following the expansion of a particular brightness line from one plot to the next, we may thus determine the expansion of the anvil itself. We are assuming here that the brightness line we are following remains associated with the same cloud material during the interval between measurements. To assure this we must remove the effect of sun angle change which was responsible for steadily decreasing illumination of the anvils during the period of observation. This was done by normalization of the reflectance values according to the cosine of the zenith angle of the sun. This method assumes, of course, that the cloud is behaving as a Lambertian surface. Sekera suggests that this is true for cirrostratus associated with turbulent outflow as would be the case in a thunderstorm cirrus shield. Martin and Suomi (1972) also note that cumulonimbus tops and cloud clusters show evidence of Lambertian behavior, at least for small solar angles. Accordingly, our measurements have been confined primarily to the middle of the day (11:00 am to 4:00 pm LST), when non-Lambertian behavior should be at a minimum.

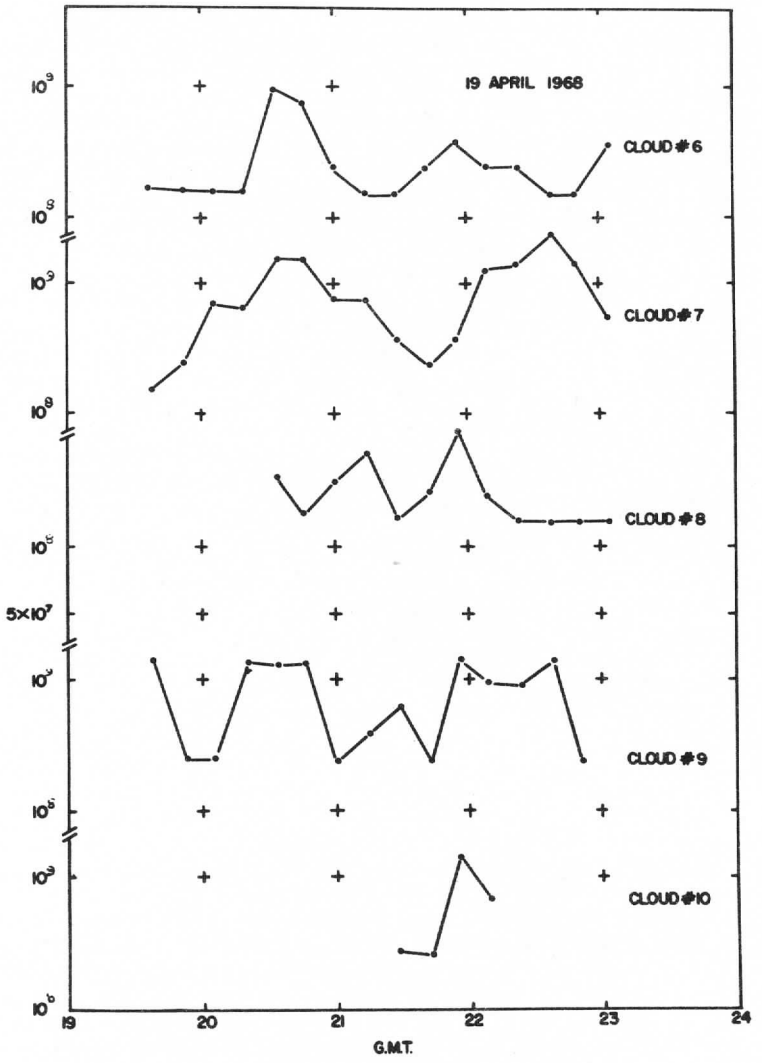

Figure 1. (After Sikdar, et al., 1971) Mass influx at the subcloud layer as a function of time.

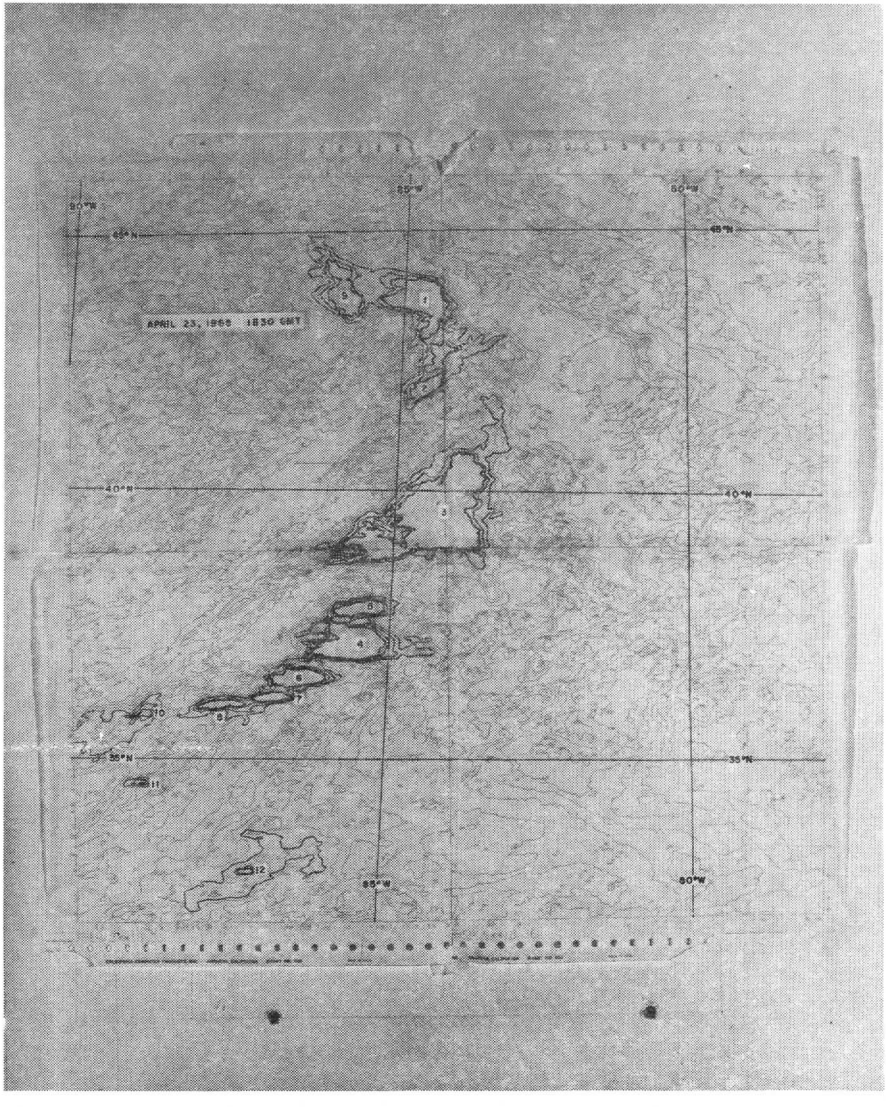

Figure 2. Brightness contour plot of an ATS-III satellite photograph, 6:30 pm GMT, April 23, 1968.

We have also assumed that the cloud material of the anvil as it moved outward did not experience significant changes during the intervals between measurement.

Finally, if we wish to convert the area growth of our anvil into a volume flux, we must assume some thickness for the anvil itself. One guide to this thickness would be the albedo of the anvil. The values of brightness for the anvil divided by the maximum possible brightness gives an albedo of about 80% for our plots which would seem to indicate, according to Neiburger (1949) and Kondrat'yev (1964), clouds having a near maximum albedo and a thickness of better than a half-kilometer. Ludlum (1966), in addition, has found that the anvils he investigated were an average of one kilometer thick. Thus an anvil thickness of one kilometer was chosen for our calculations. Conversion of other investigators' results from mass to volume flux was accomplished by means of the standard atmospheric density at 300 mb (3.16×10^{11} g/km^3).

In addition to determining volume flux from the anvil expansion, it was also possible to determine the divergence at the top of the storm from the equation:

$$(1/A)(dA/dt) = \text{horizontal divergence},$$

where A is the anvil area and t is time.

In all calculations computer plots spaced 45 minutes apart were used to determine area change with time and a planimeter was used to measure areas.

Discussion of Results

After converting those results given in terms of mass flux to volume flux, we note in tables I and II a surprisingly good agreement among these various investigators and also a good correspondence between the inflow and outflow volumes for storms of similar intensity. Judging by these data, one would estimate that there is an order of magnitude difference in the fluxes between storms of severe and moderate strength. The great size and intensity of the updrafts found in severe storms would seem to account for this difference.

Tables I and II, then, would seem to establish the validity of the method detailed in this paper. In particular, our assumption that air inflow approximates the air outflow at the top of the storm seems justified.

Table I — Anvil Deduced Volume Outflows (km^3 sec^{-1})

Storm Intensity	Volume Outflow	Investigator
Moderate	.26	Anderson (1962)
Giant Cell	1.25	Reuss (1961)
Severe	3.2	Sikdar et al. (1970)
Severe (tornado producing)*	4.6	Auvine (1970)
Severe (hail producing)**	1.1	Auvine (1970)
Severe	6.0	Fujita & Arnold (1963)
Severe	10.0	Fujita & Bradbury (1969)

*Several storms contributed to the anvil measured
**Anvils produced by single storms

Table II — Volume Fluxes (km^3 sec^{-1})

Storm Intensity	Inflow	Outflow	Investigator
Light to moderate	.16	---	Braham (1952)
Moderate	---	.26	Anderson (1962)
Light	.04 (est)		Weickmann (1963)
Moderate	.46 (est)	---	Weickmann (1963)
Severe	4.6 (est)	---	Weickmann (1963)
Hailstorm (S. D.)	.51	---	Dennis et al. (1970)
Hailstorm (S. D.)	.41	---	Auer & Marwitz (1968)
Hailstorm (Colo.)	.98	---	Auer & Marwitz (1968)
Hailstorm (Okla.)	1.3	---	Auer & Marwitz (1968)
Giant Cell	---	1.25	Reuss (1961)
Severe	---	2.2	Newton (1966)
Severe	---	3.2	Sikdar et al. (1970)
Severe	---	4.6	Auvine (1970)
Severe	6.0	6.4	Fujita & Arnold (1963)
Severe	---	10.00	Fujita & Bradbury (1969)
Hailstorm (Colo.)	.63	---	Goyer (1971)

Another approach towards establishing the soundness of using anvil growth measurements to estimate severe storm properties is to compare our derived values of divergence with those of others. Ninomiya (1969), Sikdar et al. (1970), and our own studies have used ATS-III data to gain estimates of the horizontal divergence associated with the storm cloud outflow. Ninomiya used wind fields estimated from cloud displacement vectors instead of anvil area change to compute his values, however. Table III shows good agreement between all investigators. It is noteworthy that the divergence values obtained by satellite compare favorably with the value of divergence obtained by Arnett (1962) from aircraft-based wind measurements, and with the average value Fankhauser (1971) obtained from the radar-observed expansion of the anvil.

Table III — Estimates of Divergence as Deduced from Anvil Growth

Divergence (sec^{-1})	Investigator
4.6×10^{-4}	Arnett (1962)
3.0×10^{-4}	Sikdar et al. (1970)
1.6×10^{-4}	Ninomiya (1969)
5.0×10^{-4}	Auvine (1970)
1.3×10^{-4}	Fankhauser (1971)

It should be emphasized that although these techniques measure the average divergence within a given area, it is not valid to assume that all parts of the area are equally divergent. This point is illustrated in figure 3, where 1/A versus divergence is shown for a number of different severe storm complexes over the Ohio River Valley and adjacent areas, as observed by ATS-III on April 23, 1968. The areas and divergence were measured from computer plots as described earlier. Figure 3 illustrates that as the area increases the divergence decreases proportionately. Thus for a given severe storm or severe storm complex, the divergence computed will depend on the size of the area included in the measurement. This conclusion is in accord with the observation of many investigators that surface patterns of convergence will depend to a large extent on the scale chosen. Methods using Gauss's theorem to compute the difference, therefore, give results applicable to the area used for computation only.

Figure 4 shows the rapid decay of divergence with time for these storms when we use the concept of the average divergence measured over the entire anvil area. The reason for this behavior is explained by the formula used in our calculation:

Average divergence = (1/A)(dA/dt).

It is obvious that if dA/dt is constant or only slightly increasing, then the divergence has to decrease with area. Figure 5 shows dA/dt to be fairly constant for a given cloud complex. This is consistent with our findings in figure 4, since if the area is proportionate to time (figure 5) and the rate of area change is constant, then the divergence must vary inversely with time. These results suggest that we are dealing with a highly divergent core region surrounded by a region of nondivergent flow as seen in figure 6. This model, when reduced to its most simplistic form, gives the flow pattern associated with a simple two-dimensional point source (e.g., Milne-Thompson, 1969, pp. 192-201), with a velocity distribution which may be derived as follows:

dA/dt = constant = $(2\pi r)(dr/dt) = 2\pi r u$ or $u = \text{constant}/r$,
where u is the radial velocity away from the point source and
r is the radial distance.

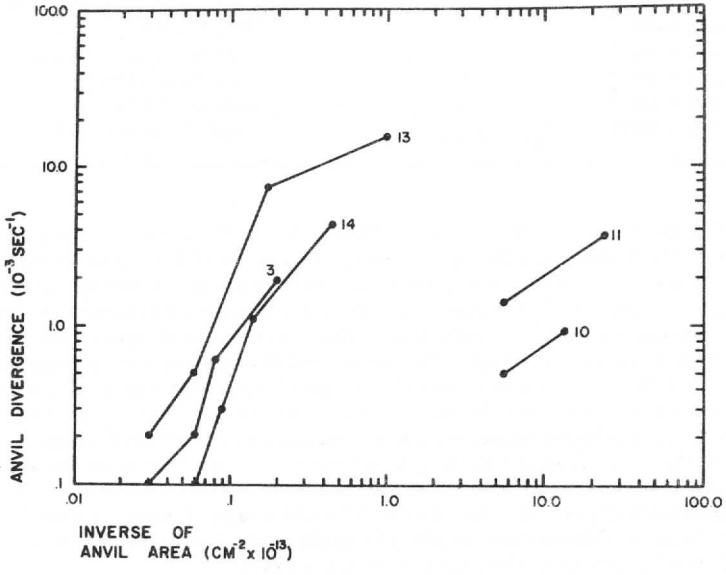

Figure 3. The log of the anvil divergence as a function of the inverse of the anvil area for various storms on April 23, 1968. The numbers next to the curves refer to the clouds numbered in figure 7.

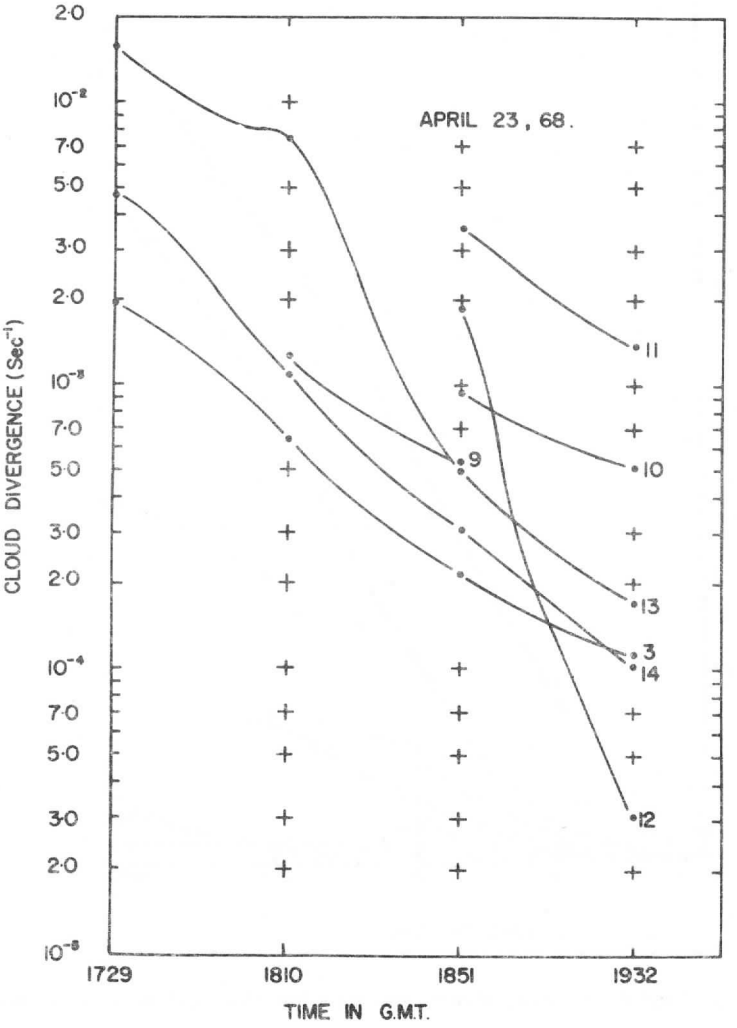

Figure 4. Divergence in the cloud shield as a function of time.

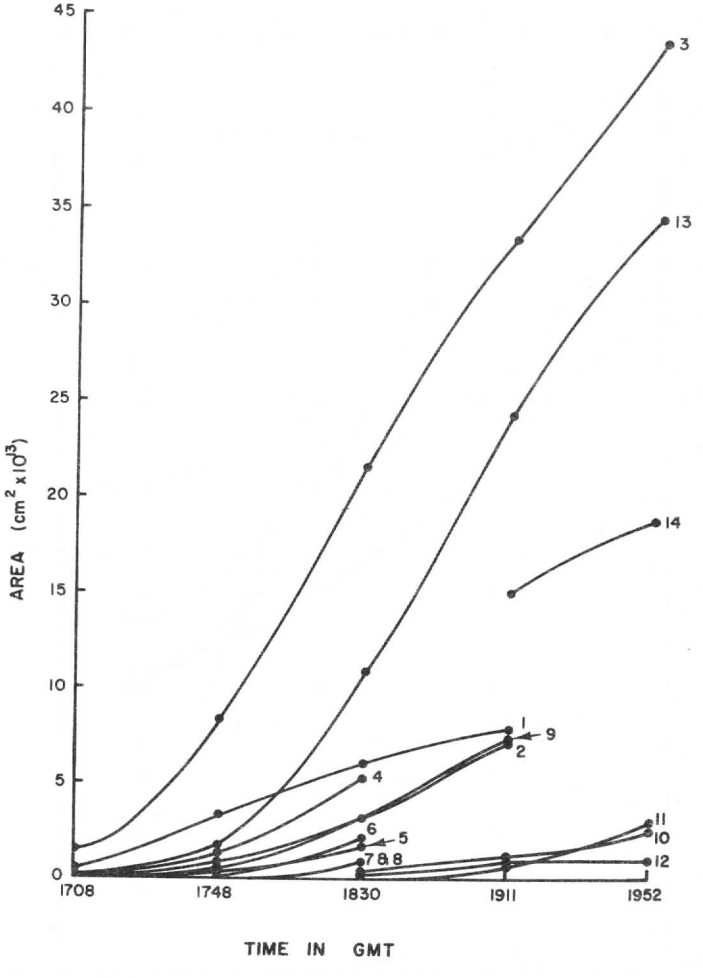

Figure 5. Cloud shield area as a function of time.

We suggest that there is some merit to applying this concept to the expanding anvil shield.

For satellite photos of April 23, 1968, individual cells (10, 8, 7, 6, 5, 11, 12)—in figure 7 appear to be single storms, whereas 3 and later 13 are conglomerates of several storms, as we have determined by transposing simultaneously observed radar precipitation echoes into the satellite depiction. Storm 13 results from the combination of storms 4, 6, 7, 8, and 5 into a single entity for purposes of computing anvil areas. The photographs show the clouds in plumes very similar in shape to the hailstorm cloud described by Fujita and Byers (1962), where their anvil plume spread downstream at 32,000 feet for at least 100 miles. Fujita and Byers show the outline of the plume in a form which could be roughly described as

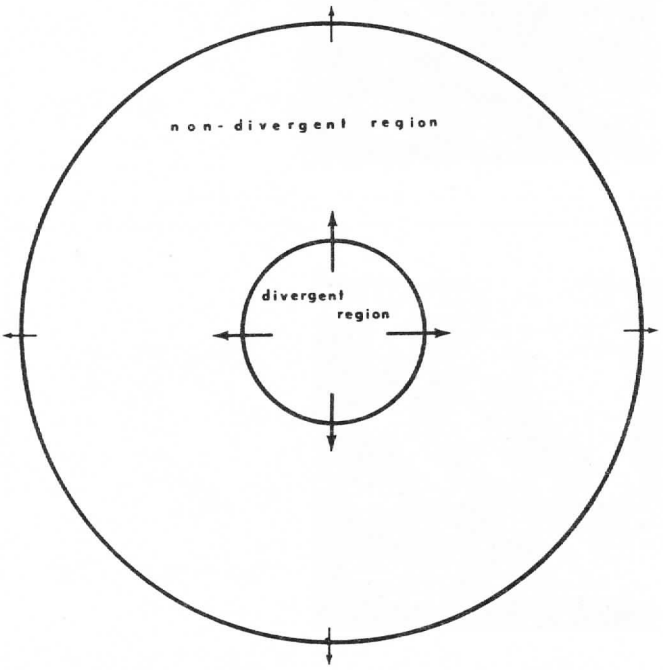

Figure 6. A model of airflow within the thunderstorm anvil assuming calm environmental winds. A divergent core is surrounded by a ring of nondivergent cloud.

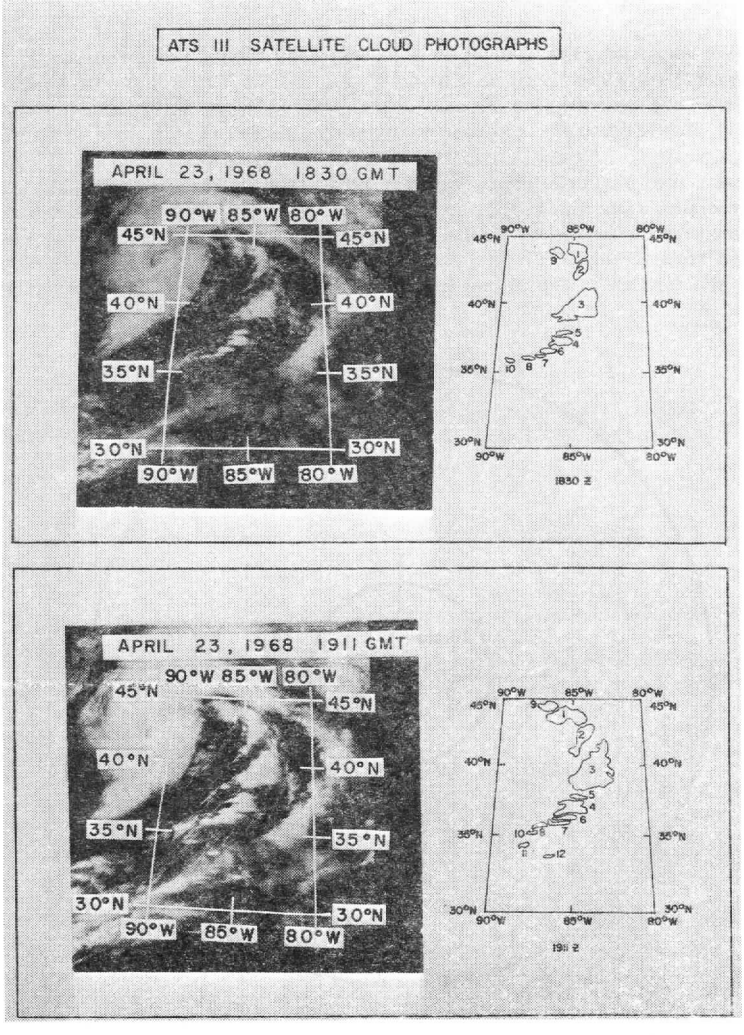

Figure 7. (After Sikdar, et al., 1971) Severe storm clouds over the United States on April 23, 1968.

elliptical or tear-drop shaped with the pointed end at the extreme downstream position. If one considers the results of figure 5, that is, $A = A_0 + kt$, as a fair approximation, then the rate of growth of the areas of the plumes may be taken as constant. If we equate the rate of growth with the rate of production of area in the region of divergence, we may draw the analogy of a simple source of strength, $2\pi m$, to characterize these plumes, where the source strength is given by m, or dA/dt. McLean (1961) suggests that one can describe the flow field in the upper part of a large severe storm (penetrated by a B-47) as a combination of divergence and translation with a divergent annulus surrounding a calm core and nondivergent flow in the external regions—very similar in description to what we show in figure 6.

Using the simple idea of considering the shape of the anvil to be the result of divergence and translation, or, in other terms, using the model of a point source in a uniform stream (Milne-Thompson), the outlines of the material boundary have been generated as shown in figure 8. As an approximation, the outline resembles very closely those seen in the satellite photographs and those described by radar (Hitschfeld, 1962). If this model has any validity, then one should expect a nearly symmetrical anvil when the wind is almost calm at anvil formation levels. This is observed and strikingly obvious in Reuss's study (figure 9).

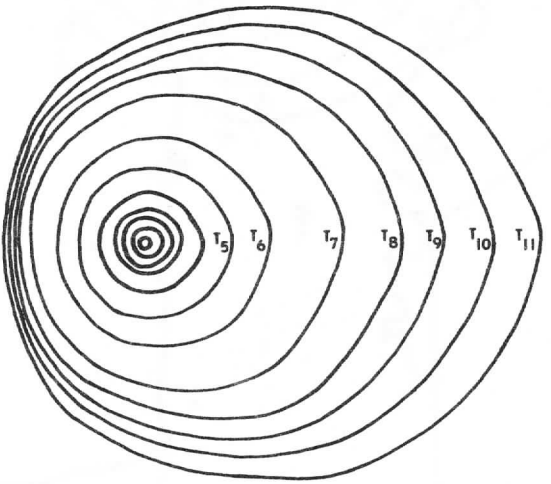

Figure 8. The material outline of a cumulonimbus anvil assuming its growth to be the result of a point source in a uniform stream.

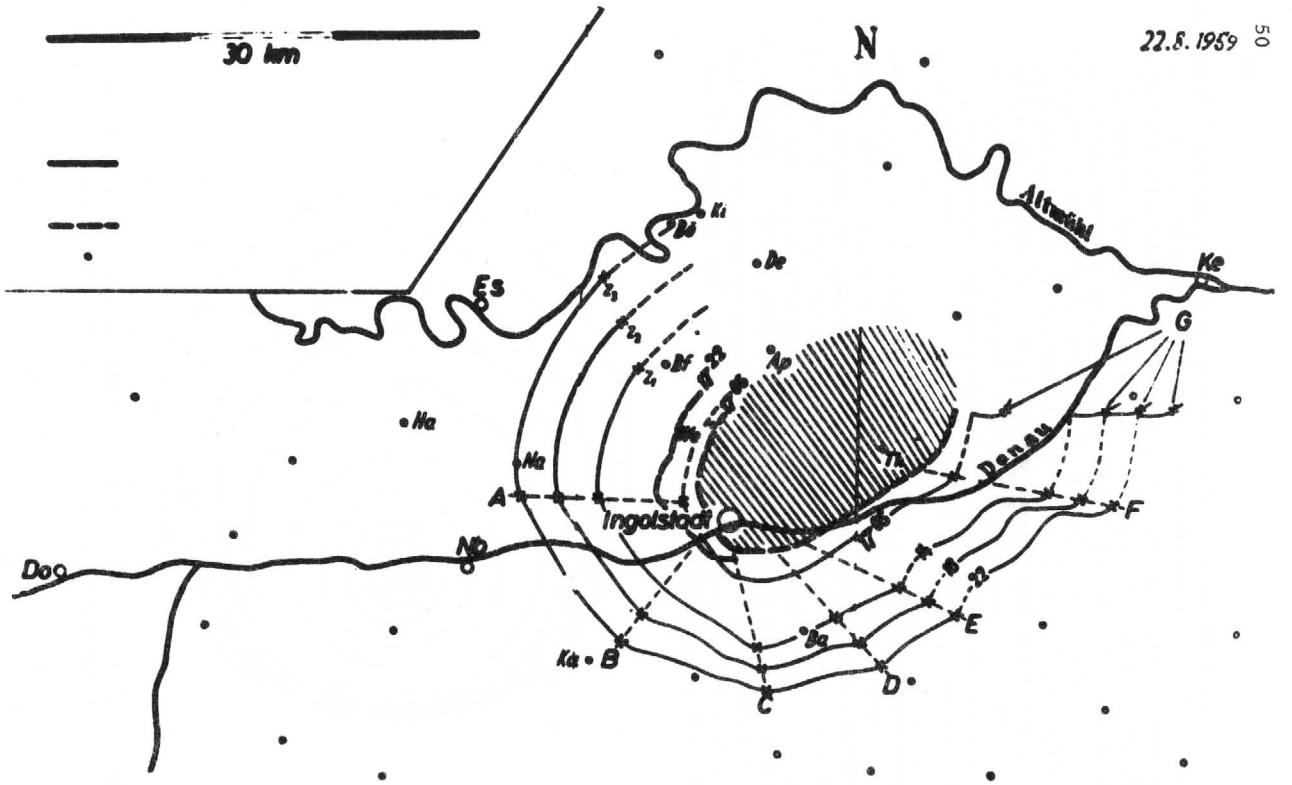

Figure 9. (After Reuss, 1961) The growth of a cumulonimbus anvil observed over Germany on August 8, 1959.

Of course this model is applicable only to anvils generated from a single storm. As can be seen from figure 7, there are two cloud masses, 3 and 13, which are composed of several single storms all during the period of observation and their shapes are therefore a composite of several anvils.

It is perhaps significant that according to figure 4, faster growth of anvil area occurs when storms join into one anvil than when they existed as clearly separate entities prior to 6:30 pm GMT. This hypothesis is evidenced by a change in slope in the area versus time curve in the early stages of storm growth (see figure 8). Thus while clouds 3 and 13 at first exhibit a growth rate similar to the smaller, single-point source storms (such as 10), later growth as a conglomerate take place at a greater rate. This increase in growth rate suggests some sort of synergistic interaction between the point sources when they come in sufficient proximity to one another.

Finally, the relationship between the rate of production of the anvil (source strength) and the wind speed at anvil level was investigated to determine whether the idea of "venting" by the wind had any validity. Many authors in the past (e.g. Newton (1966)) have suggested such a relationship as a necessary condition for the formation of severe storms. Jih-Ping and Cheng-Li-Shoo (1964) have shown in their numerical model that growth rates of cumulus are encouraged by wind shear, although other modeling experiments (Takeda (1966); Asai (1964)) suggest that convective activity is suppressed if the wind shear becomes too strong. In figure 10 the cloud outflow is plotted as a function of wind velocity at the anvil level. This graph clearly suggests that the stronger outflows are associated with stronger winds at the outflow level. Whether or not this indicates a cause-and-effect relationship between anvil level winds and anvil outflow is a question for later investigation. However, Johnson and Sechrist (1970) have made the suggestion recently that the vertical wind shear, particularly in the jet stream, acts on sloping isentropic surfaces to cause a destabilization of the lower atmosphere when momentum convergence is produced by the translating jet core. They applied this concept to the region in which the severe storms of April 23, 1968, occurred and found good evidence to substantiate this hypothesis.

Conclusion

The preceding discussion should indicate that anvil expansion data is a reliable method of obtaining upper tropospheric fluxes and divergence from some storms. Such a method relies only on satellite data and therefore should be of great use in areas lacking conventional ground instrumentation.

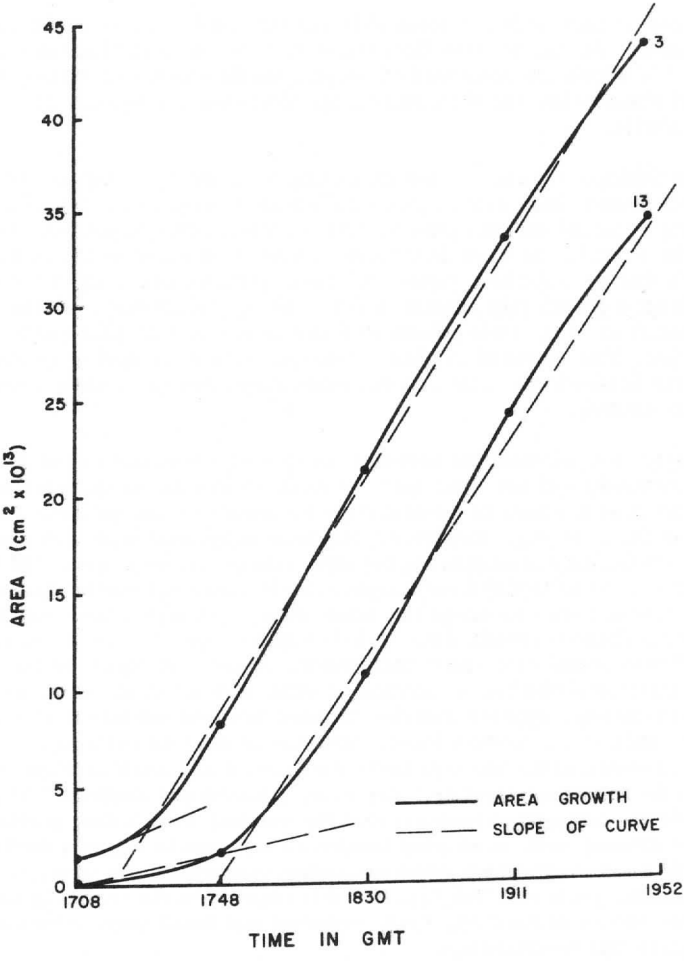

Figure 10. The change in slope of anvil growth curves for two thunderstorm cloud complexes.

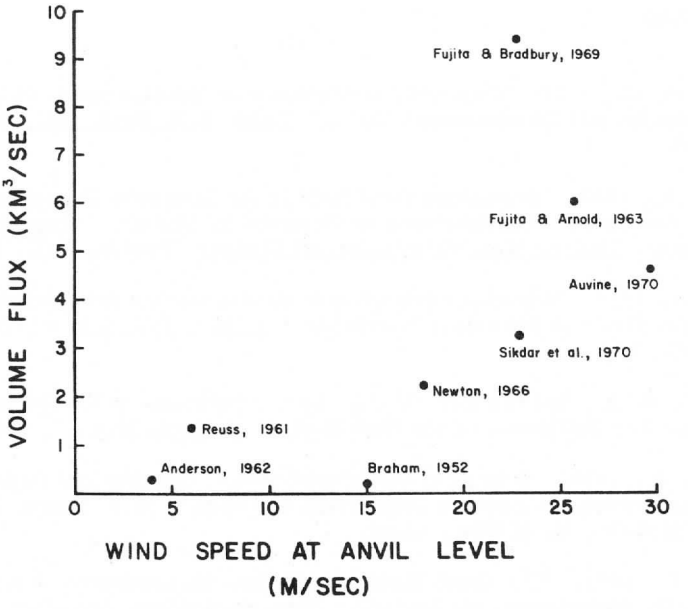

Figure 11. Volume fluxes as a function of wind speed at the anvil level for various storms.

In addition, we have shown that a point source concept of a growing cumulonimbus anvil conforms well with the observations and is useful in explaining the shape of anvils observed by satellite. We have also raised the questions of (i) possible interaction between proximate point sources to give nonlinear growth rates, and (ii) the relationship between individual storms and the wind shear. Further studies on these interactional phenomena are needed. Such studies, using satellite data, should provide new insight into the flow properties of severe storms.

Acknowledgments

The authors wish to thank Dr. Verner E. Suomi for use of the Space Science and Engineering satellite tape library and other facilities, and Dr. D. N. Sikdar for his critical review of this paper and for his kind permission to reprint figures 1 and 7.

References

Anderson, C., 1962: "Observational Evidence on the Kinematics of Growing Cumulus and Thunderstorm Clouds." Trans. N.Y. Acad. Sci., 24, 898-929.

Arnett, A., 1962. "Anomalous Wind Field in the Immediate Environments of Two Severe Thunderstorms as Observed by Aircraft." Proc. 2nd Annual Conf. on Wea. Effects Aircraft Systems, Trenton, N.J., 71-80.

Asai, T., 1964. "Cumulus Convection in the Atmosphere with Vertical Wind Shear: A Numerical Experiment." J. Met. Soc. Jap. 42, 245-259.

Auer, A. H. Jr., and Marwitz, J. D., 1968. "Estimates of Air and Moisture-Flux into Hailstorms on the High Plains." J. Appl. Met., 7, 196-198.

Auvine, B., 1970. "A Study of the Interrelation of Satellite and Surface Observations in a Severe Local Storm Situation." M. S. thesis, Dept. of Meteor., U. of Wis., 38 pp.

Bates, F., 1961. "The Great Plains Squall-Line Thunderstorm: A Model." Ph. D. dissertation, St. Louis U., Univ. Microfilms, Ann Arbor, Mich. #61-6455, 164 pp.

Bates, F., and Newton, C., 1965: "The Forms of Updrafts and Downdrafts in Cumulonimbus in a Sheared Environment." NCAR Tech. Rep. #5, 16 pp.

Braham, R. R. Jr., 1952. "The Water and Energy Budgets of the Thunderstorm and Their Relation to Thunderstorm Development." J. Met., 9, 227-242.

Browning, K., 1963. "The Growth of Large Hail within a Steady Updraft." Quart. J. of R. M. S., 89, 490-506.

Byers, H., and Braham, R.R., Jr., 1949: The Thunderstorm. Washington, Govt. Print. Off., 287 pp.

Cunningham, R., 1960. "Hailstorm Structure Viewed from 32,000 Feet." Monograph #5, Amer. Geo. Union., 325-332.

Dennis, A. S., 1971. "Additional Data on Hailstorms of Western South Dakota." Bull. AMS, 51, 1072.

Dennis, A. S., Schock, C., and Koscielski, A., 1970: "Characteristics of Hailstorms of Western South Dakota." J. Appl. Met., 9, 127-135.

Fankhauser, J. C., 1968: "Thunderstorm-Environment Interaction Revealed by Chaff Trajectories in the Mid-troposphere." Nat. Severe Storm Lab. Tech. Mem. ERLTM-NSSL, 39, 14 pp.

Fankhauser, J. C., 1971: "Thunderstorm Environment Interactions Determined from Aircraft and Radar Observations." Mon. Weath. Rev., 99, 171-192.

Fujita, T., and Bradbury, D., 1968: "Determination of Mass Outflow from a Thunderstorm Complex Using ATS-III Pictures." Proc. Severe Wea. Conf. 1969, 38-43.

Fujita, T., and Byers, H., 1962: "Model of a Hail Cloud as Revealed by Photogrammetric Analysis." Tech. Rep. #3, U. of Chicago, 9 pp.

Fujita, T., and Arnold, J. E., 1963: "Development of a Cumulonimbus under the Influence of Strong Vertical Wind Shear." Proc. 10th Wea. Radar Conf., 178-186.

Goyer, G., 1971: The Joint Hail Research Project—Summer 1970, March, 1971, NCAR, pp. 29.

Hitschfeld, W., 1960: "The Motion and Erosion of Convective Storms in Severe Vertical Wind Shear." J. Met., 17, 270-282.

Jih-Ping, C., and Li-Shoo, C., 1964: "On the Effects of the Vertical Wind Shear on the Development and Structure of Convection." Acta. Meteor. Sinica, 35, 94-102.

Johnson, D., and Sechrist, F., 1970: "On the Isentropic Representation of Storms, Dynamic Destabilization and Squall Line Formation." EOS, Trans, AGU, 51, 294.

Knoll, K. H., Neumann, H. G., and Reuss, J. H., 1959: "Ein Symmetrischer Cumulonimbus." Beitrage Phy. Atmos., 32, 65-77.

Kondrat'yev, K., Minorova, Z., and Otto, A., 1964: "Spectral Albedo of Natural Surfaces." Pure and Appl. Geophys., 59, 207-216.

Ludlum, F., 1966. "Cumulus and Cumulonimbus Convection." Tellus, 4, 687.

Martin, D. and Suomi, V., 1972: "A Satellite Study of Cloud Clusters over the Tropical North Atlantic Ocean." Bull. AMS, 53.

McLean, G., 1961: "Observation of Severe Convective Activity in a Squall Line." Bull. AMS., 42, 252-264.

Milne-Thompson, L., 1969. Theoretical Hydrodynamics. 5th ed., New York, McMillan Co., 600 pp.

Newton, C., 1966: "Circulations in Large Sheared Cumulonimbus." Tellus, 18, 699-713.

Neiburger, M., 1949: "Reflection, Absorption, and Transmission of Insolation by Stratus Cloud." J. Met., 6, 98-104.

Ninomiya, K., 1969: "Meteorological Satellite Study on the Development of Tornado-Producing Thunderstorms." Proc. Severe Wea. Conf. 1969, 202-207.

Reuss, J., 1961: "Ein Gewitter bei Windstille." Beitrage Phy. Atmos., 34, 259-273.

Sekera, Z., Private communication.

Sikdar, D. N., 1969: "Convective Heat Transport over the Tropical Mid-Pacific as Estimated from a Geosynchronous Satellite Altitude." Ph. D. thesis, U. of Wisconsin, Madison.

Sikdar, D., Suomi, V., and Anderson, C., 1970: "Convective Transport of Mass and Energy in Severe Storms over the United States: An Estimate from a Geostationary Altitude." Tellus, 22, 521-532.

Takeda, T., 1966: "Effects of the Prevailing Wind with Vertical Shear on the Convective Cloud Accompanied with Heavy Rainfall." J. Met. Soc. Jap., 44, 129-144.

Weickmann, H., 1963: "A Realistic Appraisal of Weather Control." Zeitschrift. Angew. Math. Phys., 14, 528-543.

A NEW VORTEX MODEL BASED ON A ZERO LAPLACIAN OF VORTICITY

F. H. Nicholson and D. R. Johnson

Abstract:

A new model for the tangential velocity profile for a laboratory vortex is proposed and tested. The model is superficially similar to the Rankine vortex. In both models, an inner and outer regime exists and the horizontal Laplacian of the vertical component of vorticity is zero. Here the resemblance ends. Frictional forces are not considered in the Rankine vortex solution. The new model takes into account the frictional forces due to lateral and vertical wind shear and reconciles the dynamics of this force to the mass, vorticity and angular momentum distributions.

The tangential velocity profile for the new model, $U_\theta = R(C_1 + C_2 \ln R + C_3 R^{-2})$ contains an eye, a wind maximum and a gradually tapering outer wind regime. In the analysis the model profile correlates very well with Wilkins' (1964) tangential velocity profile.

The new model is divided by the presence of the mass sink into the inner and outer regimes. The inner regime where the mass sink is present contains the eye, the wind maximum, a vorticity maximum and is governed predominantly by friction due to lateral wind shear. The outer vortex, where the mass sink is absent, is characterized by a gradually tapering wind regime, constant vorticity, and a frictional sink of momentum through vertical wind shear. In the vorticity budget the convergence of vorticity flux due to the mean flow exactly counterbalances the turbulent diffusion of vorticity out of the vortex through frictional forces. The convergence of angular momentum exactly counterbalances the frictional torque. This torque is due to vertical wind shear in the outer regime and lateral and vertical shear in the inner regime.

Partially supported by National Science Foundation Grant GA 30978X and National Oceanic and Atmospheric Administration Grant 136036.

Symbols

$\underset{\sim}{F}$	Vector frictional force
g	Gravity
g_a	Absolute angular momentum
H	Height of the cage
P	Pressure
r	Distance from axis of symmetry
r_I	Distance from axis of symmetry to edge of mass sink at the top of the vortex cage
r_0	Distance from axis of symmetry to boundary of the vortex cage
R	Nondimensional radius
$\underset{\sim}{U}$	Vector velocity
U_r	Radial component of velocity
U_θ	Tangential component of velocity
$U_{\theta'}$	Nondimensional tangential component of velocity
$\underset{\sim}{W}$	General vector
w	Vertical velocity, dz/dt
z	Height in cylindrical coordinates

Mathematical Symbols

∇	Three-dimensional vector operator, $\approx \frac{\partial}{\partial r} + \frac{\underset{\sim}{\theta}}{r}\frac{\partial}{\partial \theta} + \underset{\sim}{k}\frac{\partial}{\partial z}$
∇_z	Two-dimensional vector operator, $\underset{\sim}{r}\frac{\partial}{\partial r} + \frac{\underset{\sim}{\theta}}{r}\frac{\partial}{\partial \theta}$
∇^2	Three-dimensional Laplacian

∇_z^2 Two-dimensional Laplacian

Unit Vectors for Cylindrical Coordinates

$\underset{\sim}{r}$ radial vector

θ tangential vector

$\underset{\sim}{k}$ vertical vector

Greek Symbols

α Specific volume

ζ Vertical component of vorticity equal to $\frac{1}{r}\frac{\partial}{\partial r} rU_\theta$ in a symmetric vortex

η Radial component of vorticity equal to $\partial U_\theta/\partial z$ in a symmetric vortex

θ Angular velocity, $d\theta/dt$

ι (Iota) Derivative of the vorticity, $\frac{\partial \zeta}{\partial r}$

ν Coefficient of viscosity

τ_0 Shear stress at the lower surface of the cage

τ_H Shear stress on the upper surface of the cage

ψ Stream function

1. Introduction

One of the phenomena which has always aroused the interest of man has been the origin of the wind. The Latin phrase for Holy Spirit, Spiritus Sanctus, literally means the divine wind. The infamous Japanese fighter bomber which went on suicidal missions was called the Kami-kaze (神風) which means the same thing. Modern science has made remarkable advances in the understanding of this ethereal phenomenon. The greater the advances, however, the more intricate and marvelous the workings of the atmosphere and the realization of its motion seem. Only in those few instances where the nature of the wind is also simple may its history be traced to the originating forces. In this study the distribution of the wind in a laboratory vortex is derived from a simple relationship for the vorticity, and the origin of the wind is determined from the balance of forces established in the analysis.

Vortices are mysterious entities accompanied by a host of exceptional phenomena. Kuo (1960) says, "One of the oddest phenomena in tropical storms is the existence of a central core, across whose boundary precipitation ceases abruptly and the wind subsides suddenly from the highest velocity to a very light or even calm condition." This phenomenon is common to a wide range of vortices. According to Hoecker's measurements (1960), it is present in tornadoes, and an interpretation of the data supplied by Sinclair (1960) indicates that this is the case with dust devils. Kuo, among others, has studied this phenomenon in hurricanes, and the data of Rubin and Ford (1968) reveals that the eye and wind maximum has an analogue in the movement of stars in spiral galaxies. Of course, the causes of these properties common to such diverse phenomena may be as varied as the phenomena themselves. Each case should be considered on its own merit. The point of interest is the widespread occurrence of what is superficially at least a striking similarity. If we can understand the reason for this occurrence in one case, light may be shed upon the other cases.

Depending upon the kind of vortex modeled, friction is sometimes of importance and sometimes not. In his laboratory experiment on tornadoes, Wilkins (1964) discounted frictional influence and utilized the combined Rankine vortex model (Rankine, 1886). In contrast, Kuo (1960) assigned a significant role for friction in his explanation of the hurricane vortex. Since the tornado is a more intense vortex with stronger shears, these two results are contradictory.

The combined Rankine vortex consists of an outer regime where angular momentum of inspiralling parcels is conserved and an inner regime of solid angular rotation. From the utilization of the Navier-Stokes formulation of friction and the equation of motion, one readily verifies that both regimes must be frictionless. Since Wilkins' radial profiles of experimental tan-

gential velocity data displayed the characteristic features of the profile of the Rankine vortex, he applied the Rankine model to explain his laboratory vortex and also concluded that friction was unimportant.

In his hurricane model, Kuo (1960) claims that friction plays a key role in explaining the eye and the convection that surrounds the eye. He postulated the necessity of an eye phenomenon from considerations of the maximum kinetic energy available to the parcel and the effect of the frictional torque upon the angular momentum of the parcel. The existence of a minimal radius attainable by the parcel is inferred from angular momentum considerations that the relative velocity of a parcel moving towards the hurricane eye will increase and require a source of kinetic energy. Since kinetic energy is proportional to the square of the relative velocity, the available kinetic energy must increase rapidly as the hurricane's center is approached. Frictional torque will reduce the magnitude of the relative velocity realized and also the kinetic energy that is needed to satisfy energy principles. Since the minimal radius attainable by the parcel is directly proportional to the angular momentum of the parcel and inversely proportional to the maximum available kinetic energy, it follows that the minimal radius is strongly modified by the action of frictional torque. The greater this torque, the less kinetic energy need be available to the parcel for it to attain a given radius. Thus the frictional torque imposes more livable conditions for the thermal forcing of the vortex by relaxation of the bonds of what would otherwise constitute an angular momentum straight-jacket.

In modeling the hurricane vortex, Kuo holds the coefficients of horizontal and vertical eddy viscosity to be spatial constants. This is a procedure which Lilly (1969) criticized. Scientists who create numerical models of atmospheric motion seldom employ this concept as such, due in part to the truncation properties of the finite differencing computations. Discussion of finite differencing, as opposed to diffusion, can be found in Smagorinsky (1963) among others. This also is a classical controversy and the situation in which eddy viscosity can be treated as a constant are by no means universally accepted.

The rationale for the neglect of friction in many vortex studies is that the velocity profile of the Rankine vortex is at least roughly approximate to what is observed in nature, and, second, the order of magnitude considerations of the frictional force in the free atmosphere tends to indicate the reasonableness of neglecting such small terms. For instance, the role of friction in the free atmosphere is frequently overshadowed by the other terms in the equations of motion. It has been common practice in dynamical meteorology [Panofsky (1968), Haltiner and Martin (1957)] to delete these effects of friction in the free atmosphere. This seems to be the case in the study of tornado modelling [Hoecker (1960), Ying and Chang (1970), Lilly (1969)]. This is not the case in the modelling of tropical cyclones [Rosenthal (1970a, Anthes (1970), Kuo (1960)].

The neglect of friction is a risky procedure for the following two reasons. First, the nature of friction is not well understood so that estimates of its magnitude as well as which components of the force are important vary widely. Secondly, even if it were small, in a steady flow a small force may have a significant effect over a long term. Order of magnitude considerations are sometimes misleading under these circumstances. A steady state solution must adjust to even very small effects over a long period for the small effects will slowly but surely change the flow. The final adjustment to these effects will constitute the steady solution.

The neglect of friction has other difficulties inherent in it. According to Schlichting (1955), frictionless flow in a real fluid cannot satisfy the necessary boundary conditions for the behavior of the fluid. For the flow to be frictionless it must either be a potential flow or the coefficient of molecular, not to mention eddy viscosity, must be zero. Kinetic theory requires that a real fluid must have a nonzero coefficient of molecular viscosity. No real fluid can therefore satisfy the second condition, or, conversely, for the real fluid to be in potential flow it must be frictionless. This imposes impossible physical and mathematical constraints. As soon as the normal component of the potential flow is satisfied along the boundary, then the tangential component is determined so that the no-slip condition cannot be satisfied at the same time. When the flow is rendered frictionless, the degrees of freedom in satisfying physical constraints are reduced, hence the above dilemma.

From the mathematical point of view, the vorticity transport equation for very large Reynolds numbers cannot be simplified by neglecting the frictional terms. The neglect of the viscous terms in the vorticity transport equation given below

$$\frac{\partial \nabla_z^2 \psi}{\partial t} + \frac{\partial \psi}{\partial y}\frac{\partial \nabla_z^2 \psi}{\partial x} - \frac{\partial \psi}{\partial x}\frac{\partial \nabla_z^2 \psi}{\partial y} = \nu \nabla_z^4 \psi \qquad (1)$$

(where ψ is the streamfunction, ∇_z is the del operator on a horizontal surface in Cartesian coordinates, and ν is the molecular coefficient of kinematic viscosity) reduces the equation from a fourth-order differential equation to a third-order one in space, so that it is no longer possible to satisfy the boundary conditions of the original equation (Schlichting, 1955). The result is that no matter how small the frictional force is, it cannot be neglected in a realistic solution.

The objective of this dissertation is the creation of an improved steady-state vortex model which also includes the distribution of the frictional forces coincident with the vorticity field. Even though the Rankine vortex is frictionless and has the property that the Laplacian of the tangential velocity field is zero, the new model includes lateral friction

explicitly and has the property that the Laplacian of its vorticity field is zero, a subtle but nonetheless important shift of emphasis. Thus the Rankine vortex is a particular case of the more general model. The realism of the new model will be established by a reanalysis of Wilkins' (1964) experimental data from a tornado created in a rotating Dines vortex cage.

This new model for the tangential velocity profile of a vortex is developed in several steps. First, the Rankine vortex model is reviewed. Then, a summary of Wilkins' experimental results and his application of the Rankine vortex model are presented. In the subsequent section, theoretical support for the new model is developed from the basic equations along with its application to Wilkins' vortex data. Finally, the tangential velocity profile predicted by the new model is applied to other vortex data to show that the results are not inconsistent with the new model presented in this thesis.

2. A Review of the Rankine Vortex and Its Application to Wilkins' Laboratory Vortex

In this section the combined Rankine vortex (Rankine, 1886) is developed from the equations of motion to demonstrate its applicability, its strengths and its weaknesses. After the model is discussed, Wilkins' laboratory experiment is examined to gain familiarity with the apparatus, the measurements, and his application of the Rankine model to his experimental data.

The Governing Equations

The component equations of motion and the equation of continuity are now presented in cylindrical coordinates. The assumptions of steady state, incompressibility, constant viscosity and axial symmetry are employed to simplify the development of the new model and its application to Wilkins' (1964) laboratory experiment. The assumptions of axial symmetry and steady state are legitimate since the vortex formed in the experiment achieves steady state and axial symmetry. The simplified governing equations for the steady, axially symmetric vortex are the equation of continuity

$$\frac{1}{r}\frac{\partial}{\partial r}(rU_r) + \frac{\partial w}{\partial z} = 0, \tag{2}$$

the radial, azimuthal and vertical component equations of motion

$$U_r\frac{\partial U_r}{\partial r} - \frac{U_\theta^2}{r} + w\frac{\partial U_r}{\partial z} = -\alpha\frac{\partial P}{\partial r} + \nu\left[\frac{\partial}{\partial r}\left(\frac{1}{r}\frac{\partial}{\partial r}rU_r\right) + \frac{\partial^2 U_r}{\partial z^2}\right] \tag{3}$$

$$U_r \frac{\partial U_\theta}{\partial r} + \frac{U_r U_\theta}{r} + w \frac{\partial U_\theta}{\partial z} = \nu \left\{ \frac{\partial}{\partial r} \left[\frac{1}{r} \frac{\partial}{\partial r} (r U_\theta) \right] + \frac{\partial U_\theta^2}{\partial z^2} \right\} \tag{4}$$

$$U_r \frac{\partial w}{\partial r} + w \frac{\partial w}{\partial z} = - \alpha \frac{\partial P}{\partial z} - g + \nu \left[\frac{1}{r} \frac{\partial}{\partial r} \left(r \frac{\partial w}{\partial r} \right) + \frac{\partial^2 w}{\partial z^2} \right] \tag{5}$$

and the angular momentum equation

$$U_r \frac{\partial g_a}{\partial r} + w \frac{\partial g_a}{\partial z} = r\nu \left\{ \frac{\partial}{\partial r} \left[\frac{1}{r} \frac{\partial}{\partial r} (r U_\theta) \right] + \frac{\partial^2 U_\theta}{\partial z^2} \right\} \tag{6}$$

Although the angular momentum equation may be derived from the azimuthal equation of motion, it is included to display the simple form of the advective terms and to aid in the application of basic principles.

The Rankine Vortex

The Rankine model used by Wilkins (1964) in an attempt to explain the data observed in his experiment is a combination of solutions for two different regimes of a vortex. In his book, Rankine (1886) attributes the combined solution to Professor James Thompson of Belfast. The combination consists of a "free vortex" beyond the region of maximum wind and a "forced vortex" up to that region. Rankine defined the free vortex to be a fluid field in which the tangential component of the flow field is inversely proportional to the distance of the wind from the vortex axis. Thus, beyond the region of maximum tangential wind the profile of tangential velocity is

$$U_\theta = U_{\theta_0} r_0 / r \tag{7}$$

A free vortex is by definition devoid of frictional forces and a region where angular momentum is conserved.

Rankine defined the "forced vortex" to be a rotating fluid field in which the velocity of revolution of the particles follows any law different from that of the free vortex. He pointed out that it is useful to consider one in which particles revolve in solid rotation. This particular solution for a forced vortex is the one utilized to describe the tangential velocity distribution within the region of the maximum tangential wind in the combined vortex model and is given by

$$U_\theta = r \dot{\theta}_0 \tag{8}$$

The tangential velocity profiles for the free and forced regimes of the combined Rankine model presented in figure 1 display the wind maximum and

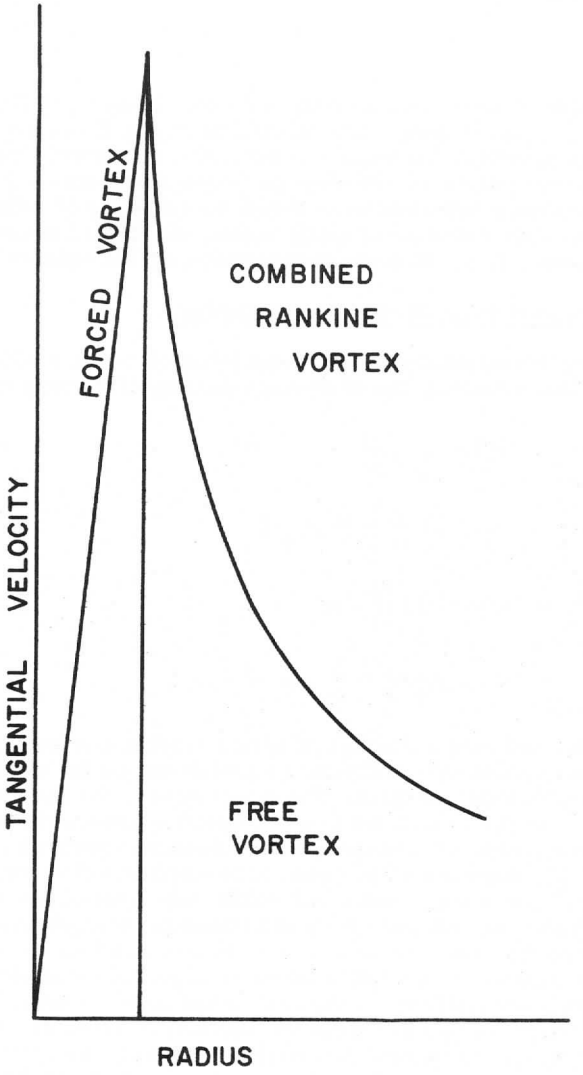

Figure 1. Combined Rankine Vortex. Inner regime is forced vortex; outer regime is free vortex.

velocity profile characteristic of many vortices. In the forced regime, the vorticity, $2\hat{\theta}_0$, is constant, while in the free regime the vorticity must be zero from the condition that angular momentum is conserved. Now the tangential velocity profiles from the Rankine Vortex Model are studied with the aid of the governing equations to ascertain the influence of radial motion. In this study of the influence of radial motion, the flow is assumed to be two-dimensional, i.e., all vertical derivatives are set equal to zero.

Rankine Combined Vortex Without Radial Motion

The simplest solution for the Rankine Model is a vortex without radial motion. In this situation, the governing equations (3) through (6) reduce to

$$U_\theta^2/r = \alpha \frac{\partial P}{\partial r} \tag{9}$$

$$0 = \nu\left[\frac{\partial}{\partial r}\frac{1}{r}\frac{\partial}{\partial r}(rU_\theta)\right] \tag{10}$$

$$0 = -\left[\alpha \frac{\partial P}{\partial z} + g\right] \tag{11}$$

$$0 = r\nu\left[\frac{\partial}{\partial r}\frac{1}{r}\frac{\partial}{\partial r}(rU_\theta)\right] \tag{12}$$

The tangential component equation of motion reduces to a balance between the pressure gradient and centripetal accelerations and the vertical component to the hydrostatic equation. The substitution of the tangential velocity relations (7) and (8) for both the free and forced regimes verifies that both the radial component (10) and the angular momentum equations (12) are satisfied, i.e., there are no frictional accelerations. This solution establishes that if such a two-dimensional vortex were created, its equilibrium existence is the characteristic state of hydrostatic-gradient balance. From the knowledge that many vortices seem to be characterized by hydrostatic and gradient balance by negligible friction and possess a maximum in their tangential velocity profiles, the Rankine vortex model is attractive. This attractiveness stems from the virtue of simplicity. Moreover, the Rankine model presents an approximate description of the tangential velocity, and even though radial motion may be present, the magnitude of the radial motion is often of lower order than that of the maximum tangential velocity.

Rankine Combined Vortex with Radial Motion

In his description of vortex motion, Rankine considered the free spiral vortex with both radial and tangential motion. In this case, the equations of motion are complicated. However, it is well to remember that in order

to simplify the equations to their maximum possible extent, all vertical derivatives and the vertical motion are assumed to vanish in order to focus upon the two-dimensional structure of the deep vortex. With these assumptions, the governing equations (2) through (6) become

$$\frac{1}{r}\frac{\partial}{\partial r}(rU_r) = 0 \tag{13}$$

$$U_r\frac{\partial U_r}{\partial r} - \frac{U_\theta^2}{r} = -\alpha\frac{\partial P}{\partial r} + \nu\left\{\frac{\partial}{\partial r}\left[\frac{1}{r}\frac{\partial}{\partial r}(rU_r)\right]\right\} \tag{14}$$

$$U_r\frac{\partial U_\theta}{\partial r} + \frac{U_r U_\theta}{r} = \nu\left\{\frac{\partial}{\partial r}\left[\frac{1}{r}\frac{\partial}{\partial r}(rU_\theta)\right]\right\} \tag{15}$$

$$0 = -\left[\alpha\frac{\partial P}{\partial z} + g\right] \tag{16}$$

$$U_r\frac{\partial g_a}{\partial r} = r\nu\left\{\frac{\partial}{\partial r}\left[\frac{1}{r}\frac{\partial}{\partial r}(rU_\theta)\right]\right\} \tag{17}$$

Integration of the equation of continuity (13) reveals that the radial velocity is

$$U_r = U_{r_0} r_0/r \tag{18}$$

Now the free and forced regimes of the Rankine vortex are considered separately.

In the free vortex the relationships for the radial and tangential velocity (7) and (18) are identical. Since the ratio of these two velocities is a constant, the trajectories will be logarithmic spirals, hence Rankine's designation—the free spiral vortex. The direct substitution of (7) and (18) verifies that all frictional terms vanish and the three component equations of motion simplify to

$$U_r\frac{\partial}{\partial r}U_r - \frac{U_\theta^2}{r} = -\alpha\frac{\partial P}{\partial r} \tag{19}$$

$$U_r\frac{\partial U_\theta}{\partial r} + \frac{U_r U_\theta}{r} = 0 \tag{20}$$

$$0 = -\alpha\frac{\partial P}{\partial z} - g \tag{21}$$

while the angular momentum equation integrates to

$$g_a = g_{a_0} \tag{22}$$

The velocity field for the free vortex with radial motion is still free of vorticity. There are no dynamical inconsistencies and the attractive nature of this solution is that it typically describes fluid motion in the sink-free outer portion of a vortex. However, a sink of mass must exist at one of the lateral boundaries and a source at the other for the steady radial circulation to be maintained.

Now attention is focused on the forced vortex. The substitution of the radial velocity (18) and tangential velocity (8) into the component equations yields

$$\frac{\partial}{\partial r}\left(\frac{U_{r_0} r_0}{r}\right)^2/2 - \frac{\theta_0}{r} = -\alpha \frac{\partial P}{\partial r} \tag{23}$$

$$2U_r \dot{\theta}_0 = 0 \tag{24}$$

$$0 = -\alpha \frac{\partial P}{\partial z} - g \tag{25}$$

The only solution that satisfies (24) is for the radial velocity to vanish, i.e., a frictionless vortex characterized by constant angular velocity cannot exist in the presence of radial motion.

In summary, the combined Rankine vortex is frictionless and consists of a free vortex outside of and a forced vortex within a given cylindrical surface. The cylindrical surface and the juncture of the velocity profiles from the two regimes are the surface of maximum tangential wind. At the juncture the first and all higher derivatives are discontinuous. Now, if one attempts to form the Rankine model from the combination of the free spiral vortex with radial motion and the forced vortex without radial motion, a second dynamical inconsistency also exists. There must be a region between the two regimes to allow for a transition between the lateral mass sink and the radial motion of the spiral vortex and the condition of zero radial motion within the forced vortex.

Wilkins' Laboratory Experiment

Wilkins' purpose was to test in the laboratory a hypothesis advanced by Vonnegut (1960) that electrical phenomena play an important role in the life cycle of the tornado. His findings were negative.

His apparatus, schematically illustrated in figure 2, consisted of a modified Dines (1896) vortex cage with an opening at the top through which air could be drawn by a fan. The cage could rotate at different speeds

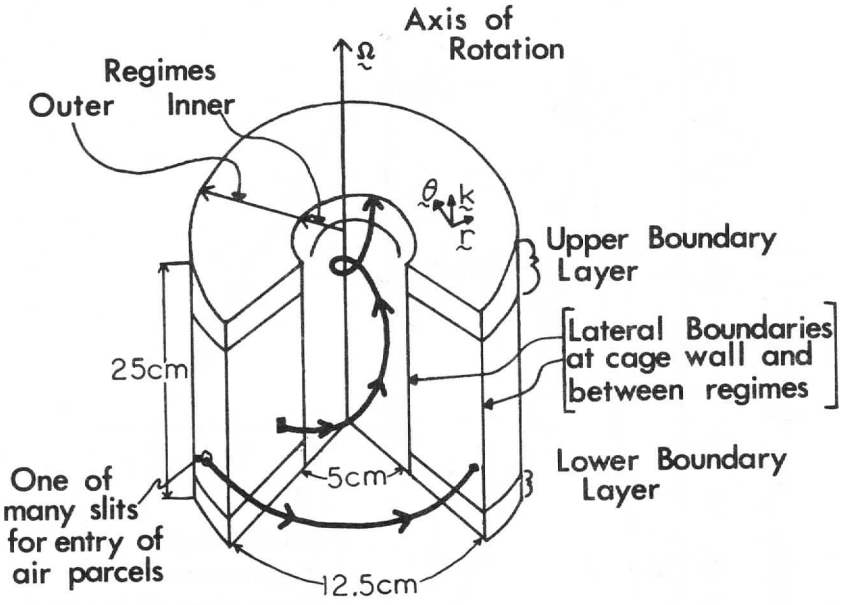

Figure 2. Schematic Diagram of Wilkins' Experiment

although the fan withdrew air at only one rate, 7.08×10^4 cm^3 sec^{-1}. This would support a radial flow at the cage edge of 36 cm sec^{-1}. The cage height and diameter are both 25 cm and the diameter of the orifice is 10 cm. The cage has side vents through which air was allowed to enter. Wilkins performed three experiments. With the fan on, the cage was rotated at high speed, low speed and not at all. The results were vortices in the first two instances and simple radial flow in the case of the third. The vortices had tangential velocity profiles which were similar. The maximum in each case occurred at 2.5 cm. The high rotation rate produced the fast vortex and the low rate a slower one. The measurements for the slow vortex were a constant percentage of the fast vortex.

The strength of the vortex was measured by two different instruments. These measurements are shown in figure 3. The first set was by a small two-cup anemomenter positioned in the center of the vortex (indicated by circles). The anemometer has telescoping arms so that readings were made at different radii by means of a stroboscope. The second set was estimated

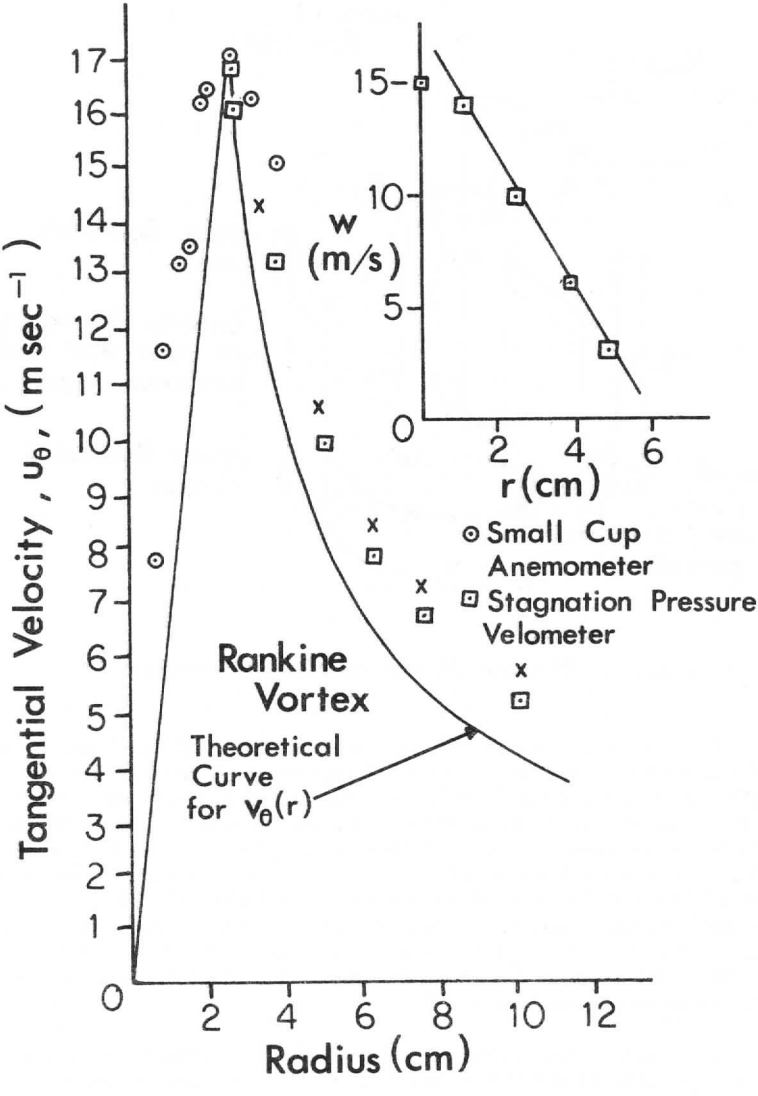

Figure 3. Wilkins' data fitted with Rankine Model. X's are corrected velometer readings.

from a stagnation pressure velometer (the squares). The calibration of the stagnation pressure velometer requires that the vortex' pressure be known. A manometer with an opening into the oncoming air stream measures the dynamic pressure of the wind in addition to the ambient pressure which is measured by another manometer which does not have an opening facing into the wind. By Bernoulli's equation the dynamic wind pressure is obtained from the total pressure by subtracting the ambient pressure from the total pressure measured by the first manometer. From the dynamic pressure the wind speed is obtained. A small error is introduced if the ambient pressure outside the vortex is substituted for the ambient pressure within the vortex. From Wilkins' personal communication it seems that this is the case. Order of magnitude considerations, however, reveal that the error introduced is negligible.

Wilkins measured the total horizontal velocity from the velometer and calculated the tangential velocities from the assumption utilized in the Rankine vortex that the flow in his vortex was frictionless and that the angular momentum of the inspiralling air in the outer regime was conserved. Through the angular momentum assumption, Wilkins noted that both the tangential and radial velocities would be hyperbolic functions beyond the radius of maximum tangential wind and that the ratio of their velocities would be a constant, K. He measured this ratio at 2.5 cm and found it to be 0.36. On this assumption the streamlines make an angle of 21° with a circle concentric with the center of the vortex and the radial and tangential components are readily determined from the velocity information.

Wilkins attempts to fit these data points for the tangential velocity with a combined Rankine vortex indicated by the heavy solid lines in figure 3. Note that the model with a core of solid rotation, its velocity maximum and an outer regime where the tangential velocity is an hyperbolic function of radius, appears reasonable. However, this fit is approximate since only the three points at the wind maximum out of 16 points lie on the profile, and the other 13 points display systematic departures. The largest systematic departure is approximately 5 - 6 m sec^{-1}. If the profile were shifted upward to remove the systematic departure for the maximum number of points, then the predicted maximum of the Rankine vortex would be about 3.5 m sec^{-1} too high, or 20% off.

Although the data does not unequivocally contradict the existence of the first order discontinuity in the tangential velocity profile of the Rankine vortex model, the four observations from the cup anemometer (small circles) suggest that the profile is smooth and continuous across the velocity maximum. In the upper right corner of figure 3, Wilkins' measurements show upward vertical motion from a radius of zero to 5 cm. Upward vertical motion across the tangential velocity maximum requires inward radial motion throughout the entire inner regime of the cage.

In the earlier discussion of the forced vortex it was established that a steady state solution for Rankine's model could only be realized if the radial motion were zero. The data contradicts this dynamical constraint. Furthermore, the existence of inward radial motion across the velocity maximum is combined with the feature of undefined derivatives in the combined Rankine model, i.e., the advection of momentum across the velocity maximum is undefined. Thus the combination of the tangential velocity discontinuity and the observed radial motion lead to a serious inconsistency.

Even apart from the problem of the discontinuity, the existence of a mass sink and upward vertical motion through the inner regime of the cage is not accounted for by the combined Rankine model.

Analysis of the Tangential Velocity in the Outer Regime

There is reason to believe that Wilkins did not correctly deduce the tangential velocity profile from stagnation velometer data in the outer region of the vortex. The original data can be retrieved by re-examination of the assumptions used by Wilkins.

Wilkins assumed that the Rankine model was valid and subsequently used the model to determine the magnitude of the tangential component from the total velocity measured by the velometer. Since a new model is being proposed, this procedure is no longer justifiable and the original data must be retrieved. The assumptions which govern the presentation of his data must therefore be examined. Once this is accomplished it will become evident that Wilkins' tangential velocity estimates and the measured total velocity are not consistent with the principle of conservation of mass.

From his assumption that both the tangential and the radial velocities are a hyperbolic function in the free spiral vortex beyond the wind maximum, the relation of the measured velocity, U, to the calculated tangential velocities, U_{θ_c}, is

$$U = U_{\theta_c} \sqrt{(1 + K^2)} = 1.063\, U_{\theta_c} \qquad (26)$$

where K is the experimentally determined constant, 0.36. The actual total velocity given by the X's in figure 3 is somewhat larger than Wilkins' calculated tangential velocities. Later it will be shown that angular momentum was not conserved, thus the constant K could not be independent of radius. Nevertheless, the actual radial velocity may be calculated without making the assumption that angular momentum is conserved and K constant.

The horizontal motion must be nondivergent in the outer regime due to its solid upper and lower boundaries. Thus, the radial motion is already

determined by (18) from the equation of continuity and the total transport through the vortex cage. Wilkins states that the air intake rate of the blower is 7.08×10^4 cm^3 sec^{-1}. Dividing by the area of the cylindrical surface of the outer regime, the radial velocity of the outer lateral boundary of 12.5 cm is calculated to be 0.36 m sec^{-1}.

The relation between the total, tangential and radial velocities is

$$U^2 = U_\theta^2 + U_r^2 \tag{27}$$

Thus the new estimate of U_θ determined from the measured total velocity by the pressure velometer and the solution for the radial motion from the equation of motion is

$$U_\theta = (U^2 - U_r^2)^{1/2} \tag{28}$$

Since U_r^2 is so small compared to U^2, U_θ is nearly equal to U. For example, the actual velocity is 10.5 m sec^{-1} at 5 cm. The highest possible value of U_r is 1.08 m sec^{-1} at 5 cm. The actual tangential velocity from the square-root of the differences of (23) is 10.45 m sec^{-1}. The difference between the actual tangential velocity, U_θ, and the total velocity, U, cannot be plotted accurately on this figure so that for all practical purposes the plot of the total U given by the X's in figure 3 is equivalent to the tangential velocity U_θ. Although Wilkins did not present the rotation rate of the cage, it may be estimated from the assumption that the tangential velocity at 12.5 cm is equal to the cage velocity. It is calculated to be approximately 6.14 revolutions per second.

A Critique

There are four important reasons why the Rankine vortex model is insufficient to describe the data of Wilkins' experiment. First, the model's wind maximum is a first-order discontinuity, which is not supported by the data and is dynamically meaningless in the presence of radial motion. Secondly, the mass sink exists throughout the inner regime of the cage and across the velocity maximum that is supposed to represent the boundary between the free and forced vortices. These first two reasons have already been discussed in detail.

The third objection to the Rankine model concerns the lack of hydrostatic balance in the inner regime of the cage. Vertical velocities in the inner regime exceed 10 m sec^{-1}. An estimate of the inertial terms in dw/dt reveals that the use of the hydrostatic relation is invalid.

The fourth reason is the presence of systematic departures between the Rankine model and the data. At a radius of 2 cm in the inner regime, the

discrepancy is as high as 5 - 6 m sec^{-1}. The departues in the outer regime are not as spectacular but no less significant, for they increase in a systematic fashion. Parcels spiralling into the center of the vortex must cross isopleths of angular momentum toward lower values which is only possible in the presence of a frictional torque, a concept antithetical to the Rankine model. Actually, the data in the outer regime indicates that vorticity is constant since the systematic departure of the data from isopleths of constant angular momentum is linear with radius. This velocity departure is the rotational component of the flow, characterized by constant angular velocity. This is possible only if friction destroys angular momentum on the one hand and creates vorticity on the other.

Evidently, then, the Rankine model is not adequate to account for either the magnitude or the physics of the vortex in the cage. From this standpoint the Rankine formulation merits further study.

3. The New Model

In this section a new model of the tangential velocity profile in a vortex is derived. For the initial development, the assumptions of steady-state, axial symmetry, incompressibility and a constant viscosity, identical to those in the Rankine model are employed. Through the use of identical assumptions, comparison with the Rankine model is facilitated, and the principle that only the absolute force of friction governs the equilibrium distribution of the tangential velocity field is emphasized. The emphasis on the role of friction in a vortex represents the major difference between the Rankine model and the new model. This emphasis on friction is developed from the hypothesis for the new model that the horizontal Laplacian of the vertical component of vorticity is zero. Such a hypothesis demands that the vertical component of the curl of the frictional force vanish in a vortex. Support for this hypothesis is developed from the vorticity equation and its application to Wilkins' experimental data. Later we shall see that the presence or absence of a mass sink with the concommitant stretching of vortex tubes is a primary factor in determining the form of the tangential velocity profile.

In the first two parts of this section, the governing equations are presented for the new model. One set of equations governs the equilibrium velocity distribution in the outer regime of Wilkins' experiment, and the other governs the inner regime of Wilkins' experiment. The development of the vorticity equation to support the new model and its application to Wilkins' data follows in subsequent parts.

The Governing Equations for the Outer Regime

In the outer regime of Wilkins' vortex cage, the flow is two-dimensional except for the existence of turbulence. Mass enters the outer boundary at a

radius of 12.5 cm and exits through the internal boundary at a radius of 5 cm. Vertical motion is suppressed by the solid upper and lower boundaries. With the conditions that w equals zero, the governing equations for the outer vortex from (2) through (6) are

$$\frac{1}{r}\frac{\partial}{\partial r}(rU_r) = 0 \tag{29}$$

$$U_r\frac{\partial U_r}{\partial r} - \frac{U_\theta^2}{r} = -\alpha\frac{\partial P}{\partial r} + \nu\left\{\frac{\partial}{\partial r}\left[\frac{1}{r}\frac{\partial}{\partial r}(rU_r)\right] + \frac{\partial^2 U_r}{\partial z^2}\right\} \tag{30}$$

$$U_r\frac{\partial U_\theta}{\partial r} + \frac{U_r U_\theta}{r} = \nu\left\{\frac{\partial}{\partial r}\left[\frac{1}{r}\frac{\partial}{\partial r}(rU_\theta)\right] + \frac{\partial^2 U_\theta}{\partial z^2}\right\} \tag{31}$$

$$0 = -\left[\alpha\frac{\partial P}{\partial z} + g\right] \tag{32}$$

$$U_r\frac{\partial g_a}{\partial r} = r\nu\left\{\frac{\partial}{\partial r}\left[\frac{1}{r}\frac{\partial}{\partial r}(rU_\theta)\right] + \frac{\partial^2 U_\theta}{\partial z^2}\right\} \tag{33}$$

From the comparison with these equations and the basic equations (2) through (6), the terms which vanish from the conditions of w equal to zero are easily identified. Note by (29) and (32) that the mass transport is still nondivergent and the vortex is hydrostatic. In general, the only difference between governing equations for Rankine's spiral vortex and the solution for the outer regime is the retention of the frictional terms. However, this is an important difference since all real fluids are viscous.

In a symmetric vortex, the vertical component of vorticity is

$$\zeta = \frac{1}{r}\frac{\partial}{\partial r}(rU_\theta) \tag{34}$$

Wilkins' data for the outer regime showed that the vertical component of velocity is independent of radius, thus

$$\zeta_0 = \frac{1}{r}\frac{\partial}{\partial r}(rU_\theta) \tag{35}$$

From this result the tangential velocity distribution determined by integration is

$$U_\theta = [(rU_\theta)_0 + \frac{\zeta_0}{2}(r^2 - r_0^2)]/r \tag{36}$$

Now both the tangential and radial velocities are specified for the governing equations (29) through (33). Because the vorticity is independent of radius, the frictional terms associated with lateral shears vanish and only the radial pressure gradient and the frictional terms associated with the vertical shears are undetermined.

The distribution of the stress for the tangential component is now determined from the angular momentum equation. Combining the definition of the angular momentum

$$g_a = (rU_\theta) \tag{37}$$

with (35) provides

$$\zeta_0 = \frac{1}{r}\frac{\partial}{\partial r}(g_a) \tag{38}$$

From integration the radial distribution is

$$g_a = (g_a)_0 - (\zeta_0/2)(r^2 - r_0^2) \tag{39}$$

Thus the angular momentum decreases with decreasing radius. This feature, expressed by (38), when combined with the definition of the tangential component of stress

$$\tau_{z\theta} = \nu\frac{\partial U_\theta}{\partial z} \tag{40}$$

and the angular momentum equation (33) yields

$$U_r r\zeta_0 = r\frac{\partial \tau}{\partial z} \tag{41}$$

In the outer regime the mass transport factor $(U_r r)$ determined by the equation of continuity is independent of radius. Thus the radial distribution of the derivative of the stress is

$$\frac{\partial \tau}{\partial z} = (U_r r)_0 \zeta_0 / r \tag{42}$$

When this equation is integrated vertically from the base $(z = 0)$ to the top $(z = H)$ of the cage, the result becomes

$$(\tau_0 - \tau_H) = \left[\int_0^z \zeta_0 (U_r r)_0 \, dz\right] \Big/ r \tag{43}$$

On the condition that the magnitude of the stress at the upper and lower boundaries are equal, i.e., $\tau_0 = -\tau_H$, the radial distribution of the

surface stress is a hyperbolic function of the radius and is determined by boundary values of vorticity and vertically integrated mass transport.

Now that the influence of friction is specified, the pressure distribution is determined from the radial component equation of motion (3) given in a modified form by

$$\frac{\partial}{\partial r}(U_r^2/2) - U_\theta^2/r = -\alpha\frac{\partial P}{\partial r} + \frac{\nu}{r}\frac{\partial^2}{\partial z^2}(rU_r) \tag{44}$$

Since both the radial and tangential velocities are already determined in the viscous term, the radial distribution of the pressure gradient is unique. The pressure distribution given by integration is

$$P = P_0 - \rho\left\{\int_r^{r_0}[U_\theta^2 + \nu\frac{\partial^2}{\partial z^2}(rU_r)_0]/r\,dr + (U_r^2 - U_{r_0}^2)/2\right\} \tag{45}$$

Through this result, the pressure profile is determined from the density, the viscosity, and the radial and tangential velocities. All are specified by boundary values at the outer wall of the cage.

The governing equations for the outer regime are summarized by

$$\frac{1}{r}\frac{\partial}{\partial r}(rU_r) = 0 \tag{46}$$

$$U_r\frac{\partial U_r}{\partial r} - \frac{U_\theta^2}{r} = -\alpha\frac{\partial P}{\partial r} + \frac{\nu}{r}\frac{\partial^2}{\partial z^2}(rU_r)_0 \tag{47}$$

$$U_r\frac{\partial U_\theta}{\partial r} + \frac{U_r U_\theta}{r} = \frac{\partial \tau}{\partial z} \tag{48}$$

$$0 = -[\alpha\frac{\partial P}{\partial z} + g] \tag{49}$$

$$U_r\frac{\partial g_a}{\partial r} = r\frac{\partial \tau}{\partial z} \tag{50}$$

where the profile solutions are

$$U_r = (U_{r_0})/r \tag{51}$$

$$U_\theta = [(rU_\theta)_0 - \zeta_0(r^2 - r_0^2)/2]/r \tag{52}$$

$$(\tau_0 - \tau_H) = [\int_0^z \zeta_0 (U_r r)_0 \, dz]/r \tag{53}$$

$$P = P_0 - \rho\left\{ \int_r^{r_0} U_\theta^2 + \nu \frac{\partial^2}{\partial z^2} (rU_r)_0]d(\ln r) + (U_r^2 - U_{r_0}^2)/2 \right\} \tag{54}$$

The entire solution for the outer regime to the governing differential equations is determined by density, viscosity, the surface stress on the upper and lower boundary and the vertical distribution of the mass transport $(rU_r)_0$ on the lateral boundary of the symmetric vortex. Friction exerts its influence by the destruction of angular momentum and the coincident creation of vorticity which may be determined from the observed difference of the angular momentum at the lateral boundaries. Since air is exhausted by a suction fan through the top of the inner regime, the vertical distribution of the mass transport $(rU_r)_0$ is free to be determined by the equilibrium solution the fluid seeks, i.e., the vertical distribution of the mass transport through the lateral boundary is not arbitrarily forced. In the boundary layers, $(rU_r)_0$ should be zero on the upper and lower surfaces and increase to a maximum value midway between the upper and lower surfaces. If the cage depth is large compared to the vertical extent of the upper and lower boundary layers, the mass transport should be uniform in the interior. However, this feature cannot be isolated from the information presented by Wilkins.

In the new model, as opposed to the two-dimensional solution of the Rankine model, the full three-dimensionality of the solution to the governing equations is retained. The solution for the outer regime is determined on the assumption that the vertical motion vanished and the vorticity was independent of radius. While the first was a logical consequence of the upper and lower boundaries (disregarding the vertical turbulent transfer), the second was based on Wilkins' data for the tangential velocity profile in the outer regime. Later in the vorticity development presented in this chapter, it is established that the vorticity must be independent of radius for a steady-state symmetric vortex to be realized in the outer regime—a dynamical constraint in agreement with the observed vorticity distribution in Wilkins' data. This solution is in agreement with the hypothesis of the new model that the horizontal Laplacian of the vertical component of vorticity in a steady symmetric vortex is zero.

The Governing Equations for the Inner Regime

In the application of the hypothesis for the new model to the inner regime, several differences must be noted. Both vertical motion and a horizontal gradient of vorticity exist in the inner regime. In the vertical component equation of motion, the pressure gradient acceleration dominates gravity and the hydrostatic assumption is invalid. Thus, in seeking a solution for the inner regime, no "a priori" simplifications can be ascertained

from the data or design of the vortex cage and the full set of governing equations (2) through (6) are designated to be the appropriate differential equations for the inner regime. Furthermore, since Wilkins only presented two profiles—one for the tangential velocity and the other for vertical motion—it is impossible to ascertain the details of a solution in this regime. However, some general conditions that must be satisfied in the solution are discussed.

The mass transport through the top of the inner regime must equal the mass transport through the outer regime. In the interior, lateral mass convergence $(\frac{1}{r}\frac{\partial}{\partial r}(rU_r))$ will balance the vertical divergence $(\frac{\partial w}{\partial z})$. From the basic difference of convergent lateral flow in the inner regime and nondivergent motion in the outer regime, one can anticipate that the solution for the equilibrium tangential velocity must be different. Horizontal convergence leads to stretching of the vortex tubes in the fluid with the result that the vorticity of parcels flowing towards the center of the inner regime will tend to experience an exponential increase. The vorticity of the parcels is further modified by tilting and friction. The result is that the solution must admit gradients of vorticity in the interior of the vortex.

Since a source for the vertical component of vorticity is admitted through horizontal convergence, the frictional terms in the angular momentum and tangential velocity equations are modified. Stresses associated with lateral shears must occur. The viscous terms in the radial and vertical components are linked through the shears in the radial and vertical velocities that develop to satisfy mass continuity, while the similar terms in the angular momentum and tangential velocity equations evolve from the realization of vorticity through the horizontal mass convergence.

The detailed solution of the full three-dimensional vortex in the inner regime is not attempted in this research due to the complexities introduced by the nonlinear nature of the inertial redistribution of momentum and the lack of information on the vertical structure in Wilkins' experiment. The primary hypothesis set forth in this study that that the horizontal Laplacian of the vertical component of the vorticity is zero. From this hypothesis the tangential velocity profile is specified, a solution which admits stresses from both vertical and lateral shears in both the tangential velocity and angular momentum equations. The solution for the outer regime that is established in some detail in this study is a special case. The solution for the Rankine combined vortex is still more restricted. For the inner regime the primary support of the hypothesis will rest on the fit of the model's tangential velocity profile (determined by this hypothesis) to Wilkins' data and the complete solution to the outer regime. However, before the new model and data are compared, the vorticity equation is developed to study the vorticity distribution and to establish that vorticity will vary in the inner regime but be constant in the outer regime.

The Vorticity Theorem

Since the governing equations for the inner regime are so general, a unique solution cannot be established to ascertain the validity of the hypothesis for the new model. As an alternative, the basic premise on the role of friction in a vortex is studied through the vorticity framework in order to gain insight into the dynamics of the vortex. The three-dimensional vorticity equation is developed to ascertain the simplifications introduced by the steady-state and symmetric conditions. Homogeneity and incompressibility are also assumed to facilitate the development.

In 1885 Helmholtz initiated the vorticity concept to elucidate the conservation principle that vorticity was a conservative property in a homogeneous, incompressible and inviscid fluid. Bjerknes (1898) produced a more general theorem by removing the restrictions of incompressibility and developing the general circulation theorem for gases. A general theorem for the viscous fluid has yet to be developed.

The vector equation of motion is expressed by

$$\frac{\partial}{\partial t}\underset{\sim}{U} + (\nabla\times\underset{\sim}{U})\times\underset{\sim}{U} + \nabla(\underset{\sim}{U}\cdot\underset{\sim}{U}/2) = -\alpha\nabla p + \underset{\sim}{F} \tag{55}$$

From the definition of vorticity, the curl of $\underset{\sim}{U}$, its local time rate of change given by the curl of (55) is

$$\frac{\partial}{\partial t}(\nabla\times\underset{\sim}{U}) + \nabla\times[(\nabla\times\underset{\sim}{U})\times\underset{\sim}{U})] = -\nabla\alpha\times\nabla p + \nabla\times\underset{\sim}{F}\ . \tag{56}$$

Use of the vector relation

$$\nabla\times[(\nabla\times\underset{\sim}{U})\times\underset{\sim}{U}] = \underset{\sim}{U}\cdot\nabla(\nabla\times\underset{\sim}{U}) - (\nabla\times\underset{\sim}{U})\cdot\nabla\underset{\sim}{U} + (\nabla\times\underset{\sim}{U})\nabla\cdot\underset{\sim}{U} \tag{57}$$

in (56) yields

$$\frac{\partial}{\partial t}(\nabla\times\underset{\sim}{U}) + \underset{\sim}{U}\cdot\nabla(\nabla\times\underset{\sim}{U}) - (\nabla\times\underset{\sim}{U})\cdot\nabla\underset{\sim}{U} + (\nabla\times\underset{\sim}{U})(\nabla\cdot\underset{\sim}{U}) \tag{58}$$
$$= -\nabla\alpha\times\nabla p + \nabla\times\underset{\sim}{F}\ .$$

The first term is the local rate of change of vorticity, the second is the advection of vorticity, the third is a term which deals with the tilting and/or stretching of vortex tubes, and the fourth represents changes from compressibility. The influence of the absolute forces are through the solenoidal and frictional terms on the right hand side.

From the steady-state, incompressible and homogeneous assumptions, the vorticity equation reduces to

$$\underset{\sim}{U} \cdot \nabla(\nabla \times \underset{\sim}{U}) - (\nabla \times \underset{\sim}{U}) \cdot \nabla \underset{\sim}{U} = \nabla \times \underset{\sim}{F} \tag{59}$$

In an axially symmetric vortex without vertical shear, the vorticity $\nabla \times \underset{\sim}{U}$ is confined to a single component parallel to the axis of symmetry. With the presence of boundary layers in a symmetric vortex, a component of vorticity about the radial coordinate also exists due to the vertical shear of the tangential velocity. However, since the hypothesis for the new model focuses on the lateral stresses, only the vertical component of this vector equation is considered.

The scalar product of $\underset{\sim}{K}$ and (59) produces

$$\underset{\sim}{U} \cdot \nabla\zeta - \underset{\sim}{k} \cdot [(\nabla \times \underset{\sim}{U}) \cdot \nabla \underset{\sim}{U}] = \underset{\sim}{k} \cdot \nabla \times \underset{\sim}{F} \tag{60}$$

The effects of tilting and stretching in the symmetric vortex may be represented by splitting the second term into parts given by

$$\begin{aligned} \underset{\sim}{k} \cdot [(\nabla \times \underset{\sim}{U}) \cdot \nabla \underset{\sim}{U}] &= \eta \frac{\partial w}{\partial r} - \zeta \frac{\partial w}{\partial z} \\ &= \eta \frac{\partial w}{\partial r} + \zeta \frac{1}{r} \frac{\partial}{\partial r}(rU_r) \end{aligned} \tag{61}$$

The first right-hand term represents the tilting of the radial component of vorticity by differential vertical motion into the vertical component of vorticity while the second right-hand term expresses the effect of stretching of the vortex tubes by convergence of the radial mass transport. The combination of (60) and (61) yields

$$\underset{\sim}{U} \cdot \nabla\zeta - \eta \frac{\partial w}{\partial r} + \zeta \frac{1}{r} \frac{\partial}{\partial r}(rU_r) = \underset{\sim}{k} \cdot \nabla \times \underset{\sim}{F} \tag{62}$$

With the use of the Navier-Stokes formulation of friction, the curl of friction is given by

$$\nabla \times \underset{\sim}{F} = \nu \nabla \times \nabla^2 \underset{\sim}{U} \tag{63}$$

From the vector identity (Phillips, 1933)

$$\nabla^2 \underset{\sim}{W} = \nabla(\nabla \cdot \underset{\sim}{W}) - \nabla \times (\nabla \times \underset{\sim}{W}) \tag{64}$$

the curl of the Laplacian of the velocity in (60) becomes

$$\nabla \times \nabla^2 \underset{\sim}{U} = \nabla \times [\nabla(\nabla \cdot \underset{\sim}{U}) - \nabla \times (\nabla \times \underset{\sim}{U})] \tag{65}$$

With the curl of the gradient equal to zero, (65) reduces to

$$\nabla \times \nabla^2 \underset{\sim}{U} = -\nabla \times [\nabla \times (\nabla \times \underset{\sim}{U})] \tag{66}$$

The successive application of the vector identity (64) to the right-hand side of (66) yields

$$\nabla \times \nabla^2 \underset{\sim}{U} = \nabla^2 (\nabla \times \underset{\sim}{U}) \tag{67}$$

The combination of (62), (63) and (67) yields

$$\underset{\sim}{U} \cdot \nabla \zeta - \eta \frac{\partial w}{\partial r} \quad \zeta \frac{1}{r} \frac{\partial}{\partial r} (r U_r) = \nu \nabla^2 \zeta \tag{68}$$

This equation governs the distribution of the vertical component of vorticity in the inner and outer regimes of the axially symmetric vortex for incompressible and homogeneous fluids.

The Vorticity of the Outer Regime

In the outer regime of Wilkins' cage, the radial mass transport was nondivergent and the vertical motion vanished. With these two simplifications, the equation for the time rate of change of ζ reduces to

$$\underset{\sim}{U} \cdot \nabla_z \zeta = \underset{\sim}{k} \cdot \nabla \times \underset{\sim}{F} \tag{69}$$

and the advection of vorticity must balance the frictional component. Closer examination of this equation reveals that each term must vanish in the outer vortex. Since the horizontal mass transport is two-dimensional, the mass continuity equation in Cartesian coordinates satisfies the differential relations

$$u = -\frac{\partial \psi}{\partial y} \; ; \; v = \frac{\partial \psi}{\partial x} \tag{70}$$

where ψ is the stream function. With this definition for the velocity components, the advection of vorticity expressed by the Jacobian of ψ and ζ with respect to x and y is

$$\underset{\sim}{U} \cdot \nabla_z \zeta = J\left(\frac{\psi, \zeta}{x, y}\right) \tag{71}$$

The Jacobian also represents the transformation of incremental areas between two coordinate systems, in this case between (x, y) coordinates and (ψ, ζ) coordinates. However, since the isopleths of ψ and ζ are coincident, the Jacobian vanishes—a result for two-dimensional flows noted by both Dryden (1960) and Batchelor (1967). With this reduction the vorticity relation in the outer regime reduces to

$$0 = \underset{\sim}{U} \cdot \nabla_z \zeta \tag{72}$$

and

$$0 = \nu \nabla^2 \zeta \tag{73}$$

For (72) and (73) to be satisfied, the vorticity must be independent of radius throughout the entire region of the outer regime, which is exactly the result needed to establish the validity of the hypothesis for the new model and the governing equations for the outer regime. The radial distribution of vorticity inferred from Wilkins' tangential velocity profile is constant. Thus, in (74) the horizontal component $\nabla_z^2 \zeta$ vanishes. The vertical component of Laplacian of vorticity, $\nabla^2 \zeta$, must also vanish if (74) is to be satisfied. In the equations for the new model, stresses due to vertical shear are present in the outer regime. To resolve the relation of the vertical stress to the vertical diffusion of vorticity, note from the definition of vorticity (34) that

$$\nu \frac{\partial^2 \zeta}{\partial z^2} = \nu \frac{\partial^2}{\partial z^2} \left[\frac{1}{r} \frac{\partial}{\partial r} (r U_\theta) \right] \tag{74}$$

$$= \frac{1}{r} \frac{\partial}{\partial r} \left(r \frac{\partial \tau_{\theta, z}}{\partial z} \right) \tag{75}$$

From (42), $\frac{\partial \tau}{\partial z}$ is a hyperbolic function of radius. Therefore $(r \frac{\partial \tau}{\partial z})$ equals the constant $(U_r r)_0 \zeta_0$ and its radial derivative in (75) vanishes. With this result for (74), the frictional stresses destroy angular momentum and induce a rotational component of velocity; however, the parcel's vorticity is not influenced by friction. For example, in the steady vortex the parcel's vorticity, which is

$$d\zeta/dt = \underset{\sim}{U} \cdot \nabla_z \zeta = 0 \tag{76}$$

is conserved throughout the boundary layer as well as in the interior of the fluid in the outer regime.

The Vorticity of the Inner Regime

In the inner regime of Wilkins' cage, the radial motion is convergent, and differential vertical motion exists. The existence of the mass sink at the top of the cage in the inner regime forces vertical stretching of the vortex tubes and the differential vertical motion implies the possibility of tilting. There are no a priori reasons to simplify the vorticity equation.

The hypothesis that the horizontal Laplacian of the vertical component of vorticity vanishes, i.e., $\nabla_z^2 \zeta = 0$, requires that the vorticity equation for the inner regime be satisfied by

$$U_r \frac{\partial}{\partial r} \zeta + w \frac{\partial \zeta}{\partial z} - \frac{\partial w}{\partial r} + \zeta \frac{1}{r} \frac{\partial}{\partial r} r U_r = \nu \frac{\partial^2 \zeta}{\partial z^2} \tag{77}$$

In this equation the vertical diffusion of vorticity through the frictional term is balanced by vertical and horizontal advection, as well as the effects from tilting and mass convergence. Very likely, in the interior of the inner regime each plays a role in the redistribution of vorticity. However, each term is not necessarily independent of the others.

The radial component, η, in the symmetric vortex is $(-\frac{\partial U_\theta}{\partial z})$. Use of this definition, a multiplication of (77) by r and combination of terms, produces

$$\frac{\partial}{\partial r}(rU_r\zeta) + \frac{\partial}{\partial r}(rw\frac{\partial U_\theta}{\partial z}) = \nu\frac{\partial^2\zeta}{\partial z^2} \tag{78}$$

An integration with respect to radius from the center of the cage to r_I, the radius of the internal boundary between the inner and outer regimes, yield

$$(rU_r\zeta)_{r_I} + (rw\frac{\partial U_\theta}{\partial z})_{r_I} = \int_0^{r_I} \nu\frac{\partial^2\zeta}{\partial z^2}\,dr \tag{79}$$

at the internal boundary, w is zero and with the definition of stress (40), (79) simplifies to

$$(rU_r\zeta)_{r_I} = \int_0^{r_I} \frac{\partial}{\partial z}[\frac{1}{r}\frac{\partial}{\partial r}(r\tau)]dr \tag{80}$$

The integrated form of the vorticity equation (80) shows that there cannot be a net sink of vorticity in the inner regime through the combined effects of tilting and vertical advection. If (80) is integrated over the vertical extent of the cage, the result is

$$\int_0^H (rU_r\zeta)_{r_I}\,dz = \int_0^{r_I} \frac{1}{r}\frac{\partial}{\partial r}(r\tau)\Big|_0^H dr \tag{81}$$

This relation shows that the transport of vorticity through the lateral boundary of the inner regime must equal an integral of the derivative of frictional stress at the upper and lower surfaces. If τ_H is negligible across the open mass sink, then the inward transport balances this term on the lower boundary.

The contrast between this result for the inner regime and the one for the outer regime is interesting. In the outer regime, τ_0 was a hyperbolic function (53) and this term vanished. In the inner regime this term does not vanish, since the transport $(rU_r\zeta)_{r_I}$ is inward to balance the sink of vorticity at the lower boundary.

The governing equations for the new model in the outer regime and the vorticity development established that the frictional influence in vorticity at the lower boundary vanishes. In the solution for the inner regime, the transport of vorticity is inward. In this regime, the mass sink at the upper boundary concentrates vorticity by vertical stretching of vortex tubes, which ultimately diffuses to the lower boundary. Thus the transport of vorticity,

its concentration by horizontal convergence and diffusion to the lower boundarey by frictional stresses are closely linked.

The Tangential Velocity Profile

An exact solution for the tangential velocity profile in the outer vortex is given by $\nabla^2 \zeta = 0$. This solution is also applied to the inner vortex. Now this differential equation is integrated to determine the radial profile of the tangential velocity. In the next sections, the model for the velocity profile is fitted to Wilkins' data to test the hypothesis.

The differential equation represented by the hypothesis in component form is

$$\nabla^2 \zeta = \frac{1}{r} \frac{\partial}{\partial r}(r\iota) = 0 \tag{82}$$

where ι (iota) is the shear of the vorticity, $\partial\zeta/\partial r$. An integration from an arbitrary radius to a definite value r_0 shows that the shear of the vorticity is a hyperbolic function of the radius given by

$$\iota = r_0 \iota_0 / r \tag{83}$$

where the subscripts identify boundary values. The radial distribution of the vorticity determined from the definition of ι and an additional integration is

$$\zeta = \zeta_0 + r_0 \iota_0 \ln \frac{r}{r_0} \tag{84}$$

which shows that the vorticity is a logarithmic function of the radius. Since

$$\zeta = \frac{1}{r} \frac{\partial}{\partial r} (r U_\theta) \tag{85}$$

the tangential velocity profile prescribed by the integration of (85) is

$$U = \frac{1}{r}\left\{ r_0 U_{\theta_0} + \frac{1}{2}\left[\zeta_0 - \frac{r_0 \iota_0}{2}\right](r^2 - r_0^2) + \frac{r_0 \iota_0}{2} r^2 \ln \frac{r}{r_0} \right\} \tag{86}$$

From a rearrangement of (86) the simpler form for the tangential velocity becomes

$$U_\theta = r[c_1 + c_2 \ln \frac{r}{r_0} + c_3 r^{-2}] \tag{87}$$

where the constants determined by the boundary conditions are

$$c_1 = \frac{1}{2}(\zeta_0 - \frac{r_0 \iota_0}{2}) = \frac{1}{2}(\zeta_0 - c_2) \tag{88}$$

$$c_2 = r_0 \iota_0 / 2 \tag{89}$$

$$c_3 = r_0 U_{\theta_0} - c_1 r_0^2 \tag{90}$$

The solution for the Laplacian of the vorticity being equal to zero shows that the velocity profile is the sum of several terms—a linear term, a hyperbolic term and the product of a linear and logarithmic term.

The Fit of the New Model to Wilkins' Data

The ultimate test of the new model is how well the predicted profiles fit Wilkins' data. In fitting the data, the profile is divided into two segments at 5 cm to correspond to the inner and outer regimes. The predicted profile indicated by the dashed line is portrayed in figure 4. In the outer regime the dashed line passes through the four X's, the corrected velometer readings. In the inner regime, the fit by the dashed line is also good since there appears to be little systematic deviation.

The values for the constants for the new model which determine the profile for the two regimes are presented in table 1. In the outer regime the derivative of the vorticity ι (thus c_2) is zero. With c_2 equal to zero, c_1 is one-half the constant value of the vorticity ζ_0 . See (88). This constant vorticity in the outer regime is easily determined from (38) by the values of the absolute angular momentum at 5 and 10 cm. After the vorticity is determined, c_3 is computed by (90). The computed vorticity is 11.4 sec^{-1} in the outer regime. From this result the predicted tangential velocity at the outer boundary of 12.5 cm is 4.8 m sec^{-1}, at 10 cm where Wilkins' data begins the tangential velocity is approximately 5.7 m sec^{-1} and increases to 11.3 m sec^{-1} at 5 cm.

This profile of tangential velocity determined by c_1 and c_2 satisfied the governing equations in the outer regime for the new model and Wilkins' data. It is consistent with the constraint from upper and lower boundaries that the vorticity remains constant since there is no stretching or tilting of vortex tubes and the effect of frictional shears and vorticity vanish.

The parameters for the inner vortex were calculated by plotting the angular velocity determined from (87)

$$\dot{\theta} = c_1 + c_2 \ln \frac{r}{r_0} + c_3 r^{-2} \tag{91}$$

against the logarithm of the radius scaled by $1/r_0$ where r_0 is 5 cm. This is shown in figure 5. Since the data for $r \leq 5$ cm plots as a straight line in these coordinates it appears that the contribution from the last term is negligible in the inner vortex. If it is significant for very small radii, we do not have sufficient data (very likely due to the limitations of the instrumentation) to establish whether or not this is the case. The slope of the line,

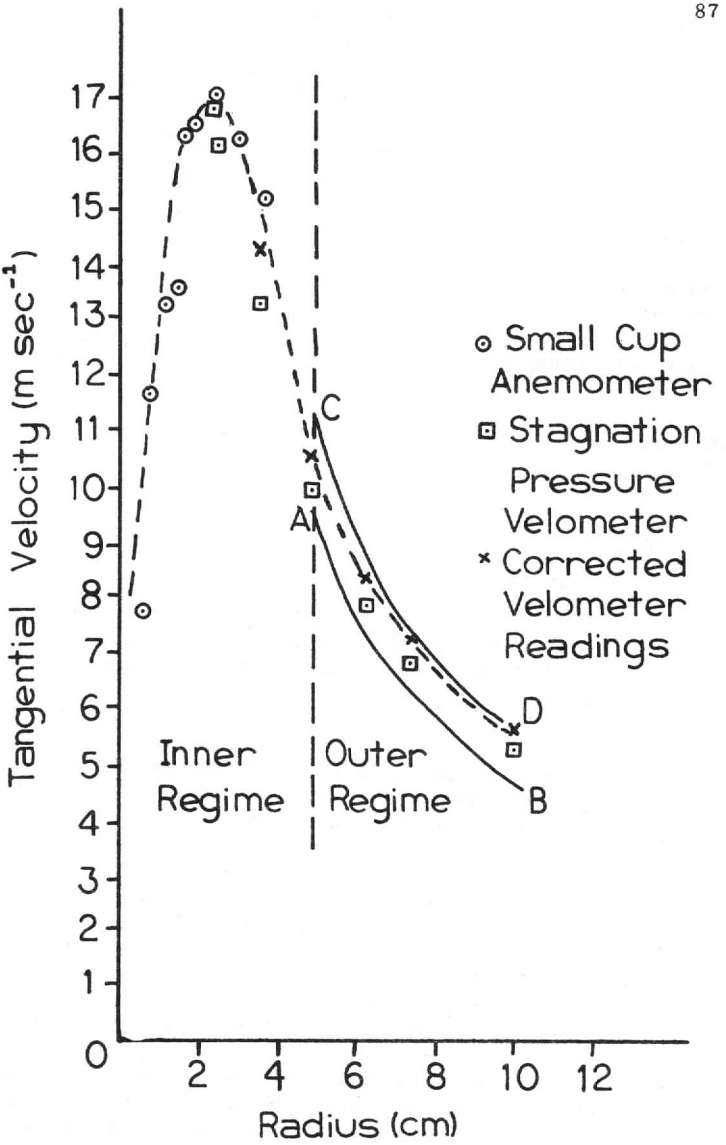

Figure 4. New Model Fitted to Wilkins' Data. Solid lines are hyperbolic segments, isopleths of angular momentum.

Table 1

Vortex Parameters and Boundary Values of the New Model for Wilkins' Data

	Inner Regime ($0 \leq r \leq 5$ cm)	Outer Regime ($5 \leq r \leq 12.5$ cm)	
r_0 - radius (cm)	5	5*	12.5
ζ_0 - vorticity (sec^{-1})	10	10*	10
ι_0 - gradient of vorticity ($cm^{-1}\ sec^{-1}$)	172	0*	0
V_{θ_0} - tangential velocity ($m\ sec^{-1}$)	10.5	10.5*	4.8
Coefficients			
c_1 - (sec^{-1})	-425	10	
c_2 - (sec^{-1})	432	0	
c_3 - ($cm^2\ sec^{-1}$)	0	47.5	

*Note. Values at the edge of the mass sink from solution for outer regime to illustrate continuity between regimes for tangential velocity and vorticity and the discontinuity for the gradient of vorticity.

c_2, and the ordinate intercept, c_1, are read directly from the semilog plot. The slope, c_2, is proportional to the derivative of the vorticity at the boundary of 5 cm and c_1 is a combination of the vorticity and ι.

For the outer regime, one cannot state conclusively that the predicted profiles from the hypothesis satisfy the governing equations for the new model since a unique solution is not determined. Support for the hypothesis is given by the excellent fit of the model and the data. However, the data provide the observed solution for the tangential velocity profile from the governing equations and in the sense that the predicted profile describes the data rather well, the hypothesis for the model appears to be verified.

If the profile predicted by the new model and the one from the Rankine vortex are compared, several factors must be noted. Although both models have two regimes, the velocity and vorticity profile remain continuous in

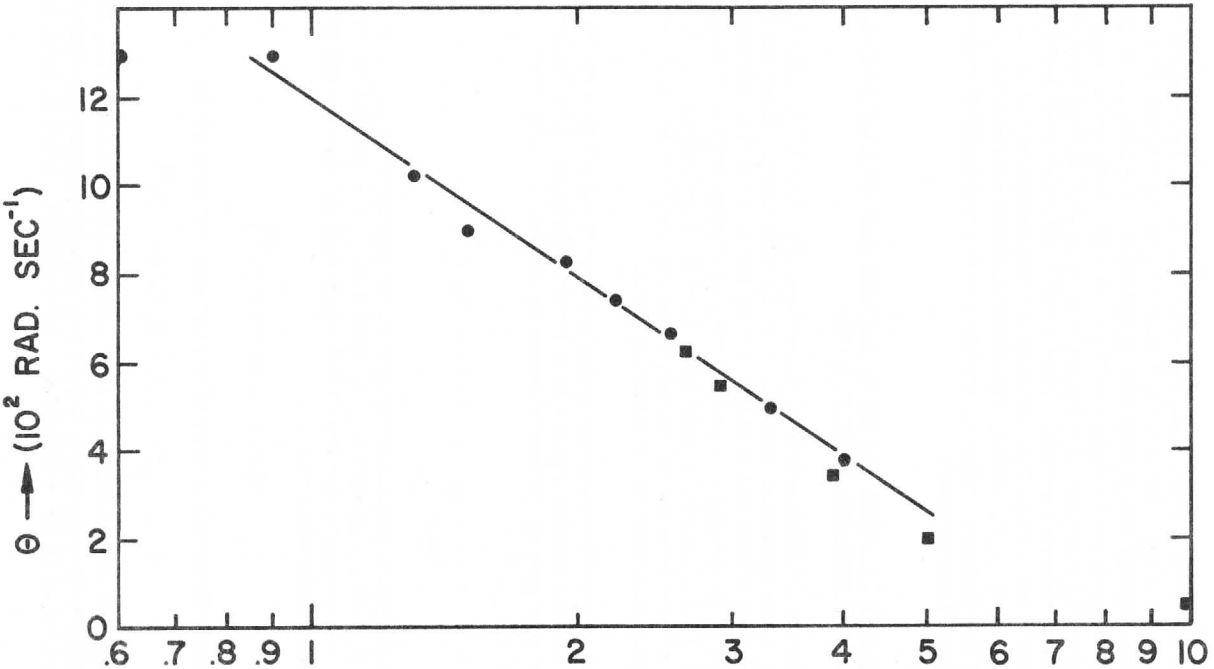

Figure 5. Profile of angular velocity, $\dot{\theta}$, versus logarithm of the nondimensional radius for the model fitted to Wilkins' (1964) data. Solid circles portray anemometer data and squares are for stagnation pressure velometer.

the new model while the vorticity was discontinuous at the velocity maximum in the Rankine model. The velocity maximum predicted by the new model is smooth and continuous and there are no systematic deviations. In the Rankine model there is no provision for the mass sink at the upper boundary. In the new model the mass sink extends to 5 cm, a factor which is consistent with Wilkins' observed vertical motion profile. Although verification of the new model for the vortex cage can only be ascertained with data on the vertical structure of the vortex, one can tentatively conclude from the excellent fit of the tangential velocity profile that the new model is superior to the combined Rankine model.

4. An Application of the New Model to Other Data Sets and A Comparison with the Results from Wilkins' Vortex

Before the completion of this discussion the scope of the new model is broadened by an application to data other than Wilkins'. There are five additional sets of data which will be subjected to analysis. There are the data of one other laboratory model by Ying and Chang (1970), data from Sinclair's (1960) dust devil, data from Lamberth's dust devil (1966), data from Anthes' (1970) numerical model of the tropical cyclone, and Rubin and Ford's (1968) data from the constellation M31.

The data from these various examples is best compared with the new model by using a nondimensional form for the tangential velocity profile (87). The nondimensional form obtained by setting $R = r/r_0$ and $U_\theta' = U_\theta/U_{\theta\ max}$ is

$$U_\theta = R\frac{r_0}{U_{max}}[c_1 + c_2 \ln R + c_3(Rr_0)^{-2}] \tag{92}$$

where the maximum tangential velocity of the profile is $U_{\theta\ max}$. If the products of $(r_0/U_{\theta\ max})$ with c_1, c_2 and $c_3 r_0^{-2}$ are denoted by C_1, C_2 and C_3, respectively, the final nondimensionalized form for the tangential velocity profile simplifies to

$$U_\theta = R[C_1 + C_2 \ln R + C_3 R^{-2}] \tag{93}$$

The corresponding nondimensional angular velocity is given by

$$\dot{\theta} = U_\theta/R = C_1 + C_2 \ln R + C_3 R^{-2} \tag{94}$$

Data points for Sinclair, Lamberth, Anthes and Rubin and Ford, on a nondimensional semilog graph, Figure 6 of angular velocity vs. radius, display a general linear relationship. Some scatter occurs at small values

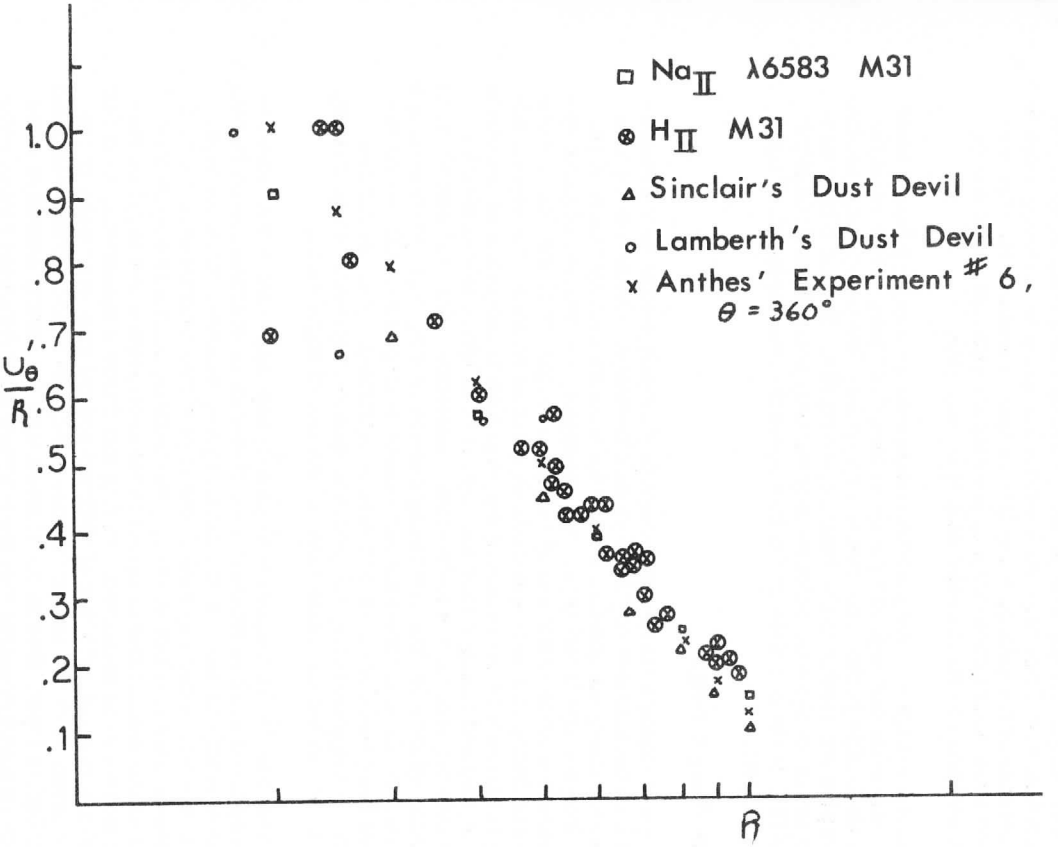

Figure 6. Nondimensional Plot of Five Vortices Other Than Wilkins'.

R, indicative of an inverse (hyperbolic function of radius) noise to signal ratio in the calculation of angular velocities from the measurement of tangential velocities. A good deal of the scatter can be attributed to the information from M31 since the data contains a larger error component due to the remoteness of the galaxy. Since the boundary constants for each data set, even when nondimensionalized, are slightly different, some scatter must be attributed to the different slopes of each line.

A closer analysis of the individual data sets on a case-by-case basis is now presented. The velocity profile of Ying and Chang (1970) is analogous to the profile in the outer regime of Wilkins' experiment, whereas the other profiles are similar to the inner regime profile. Each is briefly summarized in turn to show the relation between the observed results and the applicability of the principle of the new model that the Laplacian of the vorticity is zero.

Ying and Chang's Vortex

Ying and Chang's (1970) experiment is generally similar to the experiment of Wilkins but there are three major differences. These are the size of the vortex cage, the relative size of the mass sink of the vortex cage, and the rotation rate of the cage. The dimensions of Ying and Chang's vortex cage is 196 cm in diameter and 157 cm in height. Thus the cage volume of Ying and Chang is nearly 400 times as great as Wilkins. The second difference is the ratio of the radius of the mass sink to the radius of the vortex cage. In Ying and Chang's cage the ratio is 0.11 which is considerably smaller than the ratio of 0.4 for Wilkins' experiment. The third difference is the angular velocity of Ying and Chang's which is also much smaller—12 rpm as opposed to 367 rpm. Thus the experiment of Ying and Chang can be expected to have characteristics different from Wilkins. Yet, for the new model to have applicability, the principle that the Laplacian of the vorticity is zero in the vortex must also hold in Ying and Chang's model.

In Ying and Chang's model there is only one data point in the inner regime as opposed to 12 in Wilkins' data; therefore no function can be fit with confidence in this regime. In the outer regime, however, there are eight points in the fast vortex and nine in the slow vortex illustrated in figure 7. These points illustrate that the tangential velocity profile is a hyperbolic function of the radius (dashed curve) in the outer regime and suggests that angular momentum is conserved. In Ying and Chang's experiment, their fast rotation rate is about 1/33 that of Wilkins' and the amount of mass is 400 times as great. With the slower rotation rates, one would predict less shear in the boundary layer. This in combination with the greater amount of mass and mass transport suggests that the boundary layer frictional sink of angular momentum is too small to be a measurable effect. Thus the vortex is irrotational with both vorticity and lateral friction being zero. In an irrotational

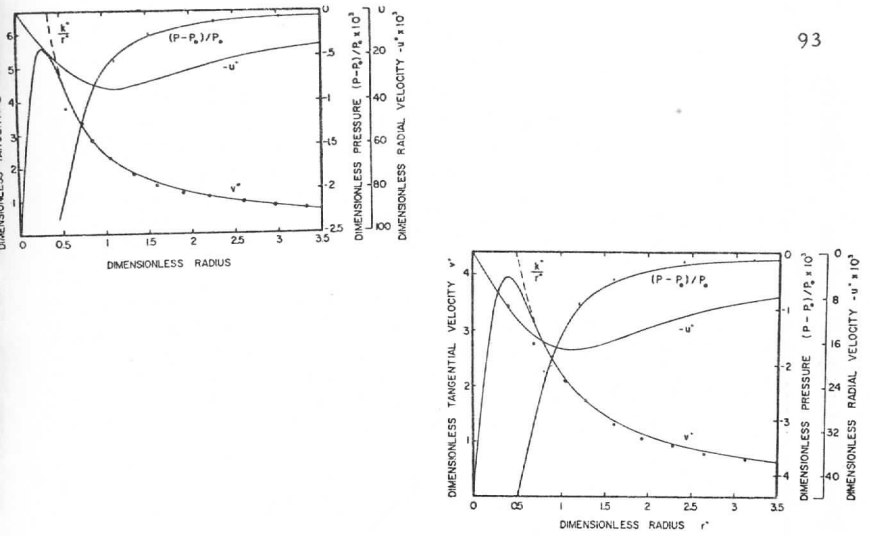

Figure 7. Ying and Chang's Vortex Profiles. Upper profile is for 8 rpm; lower profile is for 12 rpm.

vortex, C_1 and C_2 are zero in (94) and C_3 is nonzero. Since vorticity is zero, it follows that the Laplacian of vorticity is also zero as in the case of the classic Rankine vortex. The new model describes the velocity profile for an irrotational vortex as well as one in which there is vorticity.

Sinclair's Dust Devil

This set of data is extracted from measurements taken by Sinclair (1960) of a dust devil as it passed over his mobile measuring unit. Sinclair describes it as an intense dust devil, but does not give any further pertinent information on its dimensions other than what may be inferred from the data. If the translation velocity of the dust devil is assumed to be constant, then time may be transformed into radial distance.

A nondimensional plot of the angular velocity vs. the logarithm of time at every half-second, shown in figure 8, reveals that there exists a decreasing linear relationship, the condition for the tangential velocity to conform to (92) in the presence of a mass sink, and friction due to lateral shear. Thus the coefficients C_1 and C_2 are nonzero, while C_3 is zero in Sinclair's vortex, a solution similar to the inner regime of Wilkins.

The last three points deviate slightly at the far end of the time scale and suggest the presence of an outer regime. A detailed analysis is ques-

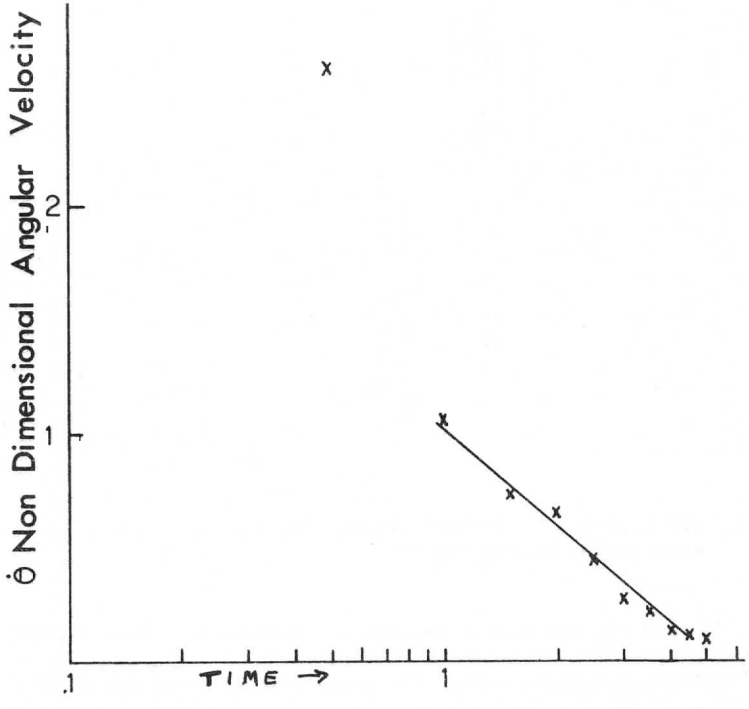

Figure 8. Semilog Plot of Angular Velocity vs. Log of Time of Sinclair's Dust Devil (raw data).

tionable, however, due to the paucity of this data. The innermost point is exorbitantly high for the fitted function. However, the noise to signal ratio of the angular velocity calculation is a hyperbolic function of radius making innermost data less reliable.

Lamberth's Dust Devil

Lamberth's (1966) data is from measurements of a dust devil as it passed over a network of stationary sensors. Using the same assumptions between time and radial distance in Lamberth's dust devil as in Sinclair's, the plot of angular velocity versus the logarithm of the time is shown in figure 9. As in Sinclair's dust devil, a decreasing linear relationship exists between the two, and the tangential velocity conforms to the new

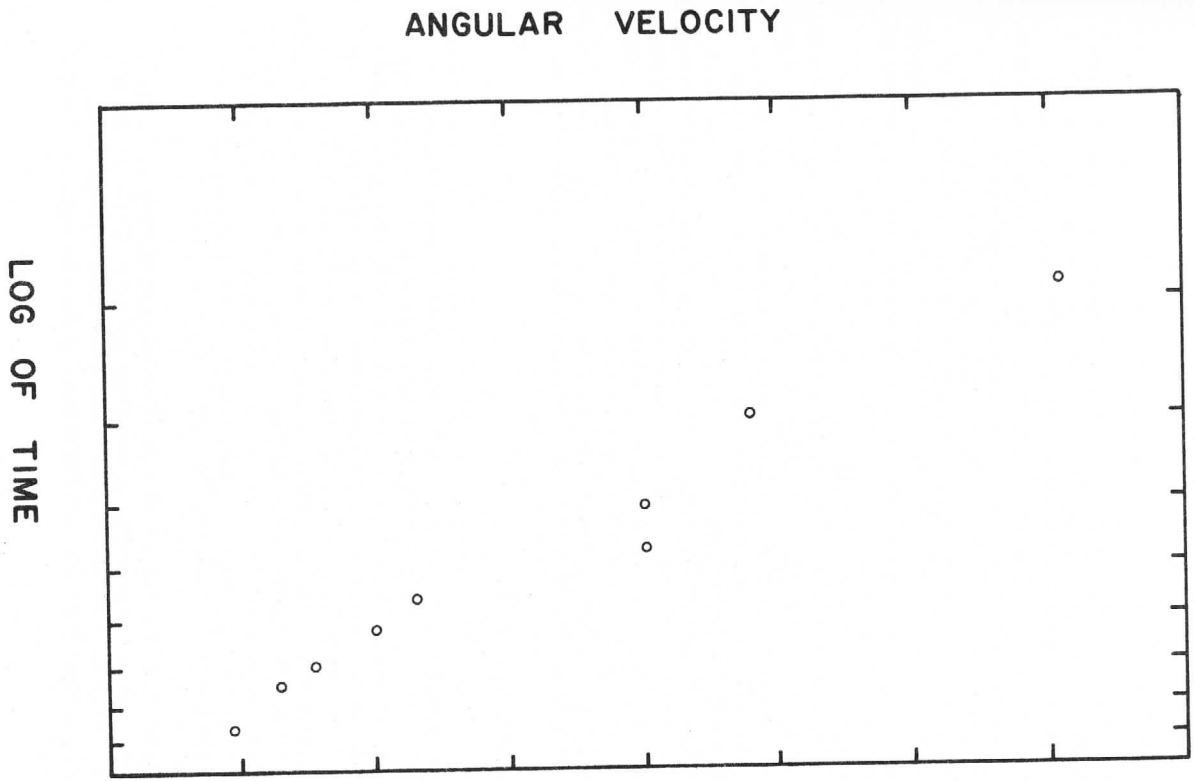

Figure 9. Semilog Plot of Lamberth's Dust Devil, Angular Velocity vs. Log of Time (raw data).

model (94). The profile is indicative of the presence of a mass sink in the vertical similar to the observations in the inner regime of Wilkins.

Anthes' Hurricane Model

In his numerical model of the hurricane, Anthes (1970) calculated tangential velocity profiles on isentropic surfaces. In a steady state, the liberation of latent heat in an isentropic layer constitutes the mass sink. Thus the portion of the vortex with latent heat release at distances of less than 150 km should conform to the formulation of the inner regime with a mass sink and the portion beyond 150 km without heating should conform to the sink-free outer regime. The semilog plot in figures 10a and 10b of Anthes' experiments #6 and #7 shows the relationship of the angular velocity to the logarithm of the radius predicted by the new model for the inner regime. In this region, Anthes (1970) illustrates that the lateral frictional force dominates over the vertical. The slight deviation of the innermost point from a linear function might possibly be reduced if the effect associated with C_3 in (94) could be evaluated. The analysis of the wind field beyond 150 km for these experiments does not yield profiles which conform to the model. In this region Anthes (1970) illustrates that vertical friction based on the bulk aerodynamic method dominates over lateral friction that is based on a Navier-Stokes formulation for friction. Thus the integration of the frictional effects of the surface stress based on the bulk aerodynamic method produces tangential velocity profiles which differ somewhat from the new model. However, since Anthes' vortex solutions were good approximations of what occurs in the atmosphere, the agreement between the new vortex model and Anthes' results suggest a de facto extension to include hurricane vortices.

Angular Velocities in M31

The last example from Rubin and Ford's (1968) data for the spiral galaxy, M31, is more in the class of curiosities, rather than an authentic data set for the vortex model. The plot of angular velocities of M31 versus the log of the radius shown in figure 11 indicates that the stellar tangential velocities also follow (94) on the semilog presentation. If the stars are fossilized remnants of the original galactic cloud, then their velocities can be treated as point tracers of the original gaseous mass. The pictures of spiral galaxies bear a remarkable similarity to the satellite pictures of hurricanes in that they both have logarithmic spiral arms. Since the tangential velocities of the stars corresponds to (94), then the Laplacian of the vorticity of the primordal gas must have been zero throughout the original cloud.

In this section, the tangential velocities for several other vortex samples over a range of seven orders of magnitude are quite similar to the profiles predicted by the new vortex model determined from Wilkins' data. This set of examples does not constitute proof of the new model; rather this

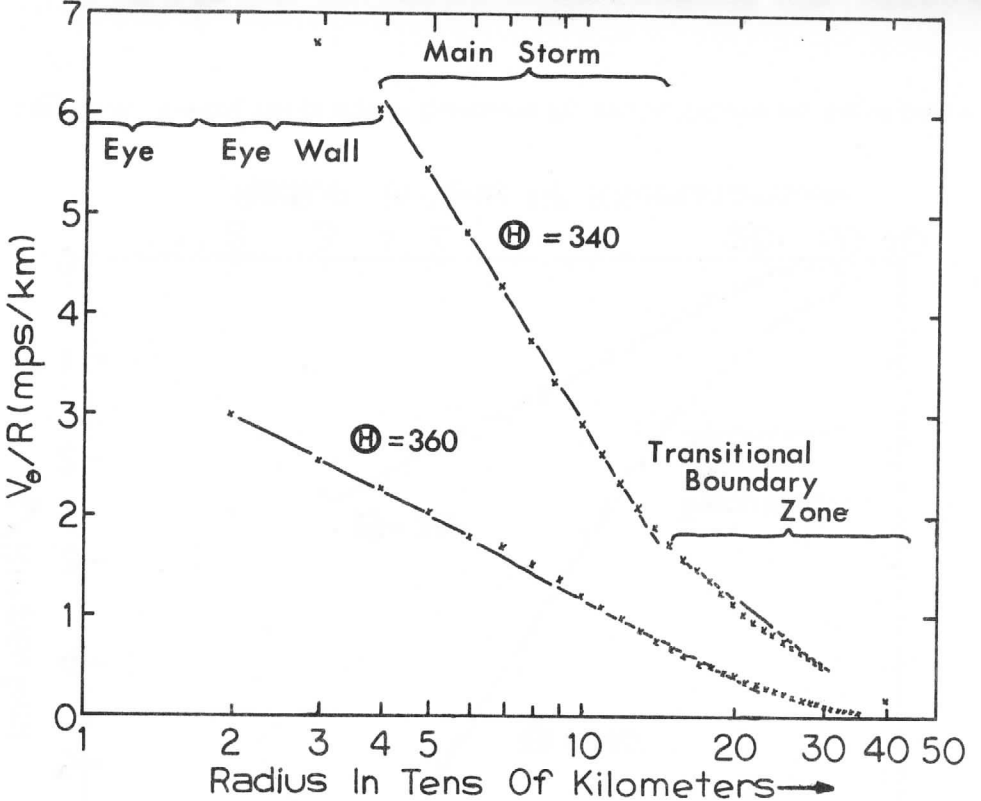

Figure 10a. Semilog Plot of Anthes' Experiment #6, Angular Velocity vs. Log of Radius

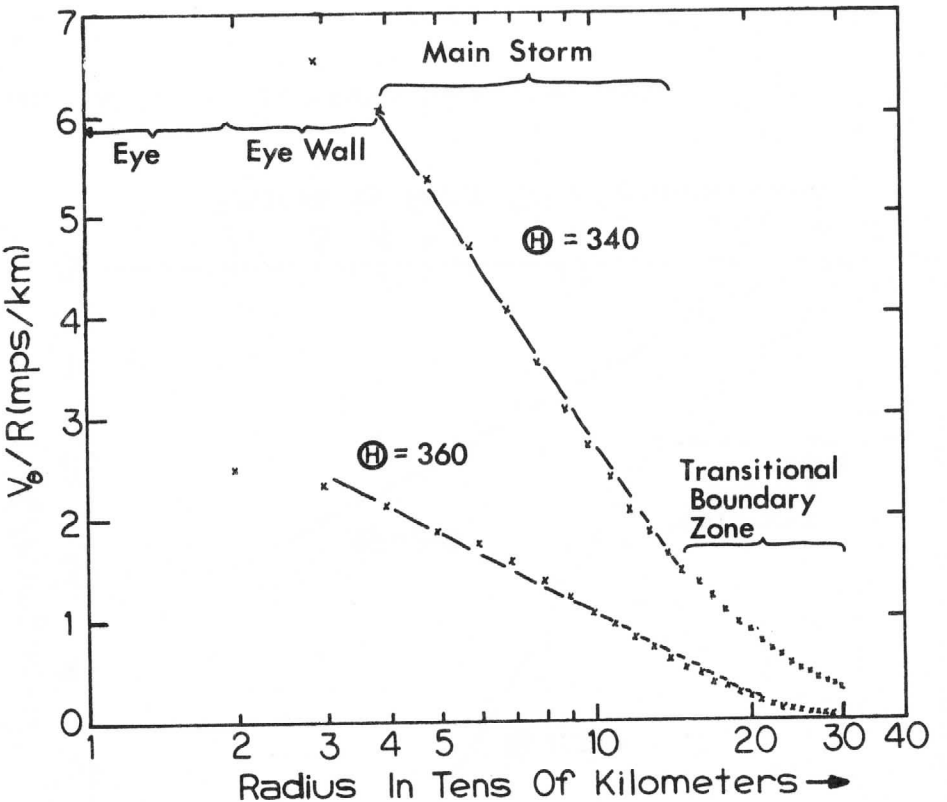

Figure 10b. Semilog Plot of Anthes' Experiment #7, Angular Velocity vs. Log of Radius

set is presented to show that there are at least some other vortices over a wide range of phenomena which do not contradict it.

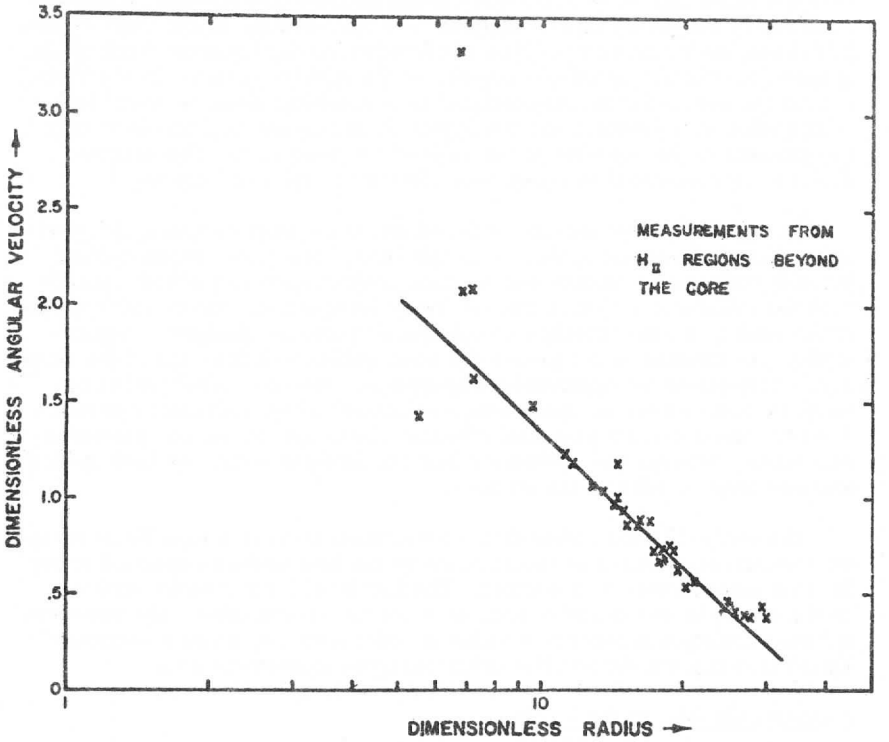

Figure 11. Angular Velocities in M31 (V. C. Rubin and W. K. Ford) vs. Log of Radius

5. A Review of the New Model

Summary

Both the new model and the Rankine model have the property that the horizontal Laplacian of the vertical vorticity is zero, but a thorough analysis of Wilkins' data demonstrates the inadequacy of the two-dimensional Rankine vortex model, yet supports the new three-dimensional model.

The mass circulation divides the new model into two parts: the inner

regime corresponding to the dimensions of the mass sink, and the outer regime corresponding to the region beyond the mass sink. The vorticity distribution is governed by this arrangement in that the physical constraints from the upper and lower boundaries of the outer regime preclude stretching or tilting of the vortex tubes, whereas both are possible in the inner regime. In the new model the outer regime is characterized by constant vorticity as opposed to constant angular momentum in the Rankine vortex. In the inner regime the new model is characterized by a changing vorticity which is a combination of a constant and the logarithm of a power function involving the gradient of the vorticity at the edge of the mass sink. The Rankine model is characterized by a constant vorticity in the inner regime.

As opposed to the Rankine model in which the wind maximum is a first-order discontinuity and unable to satisfy basic dynamical considerations, the new model has a smooth and continuous wind maximum which satisfies both the equations of motion and the vorticity equation. Along with the rest of the model, it also satisfies circulation and angular momentum requirements. The Rankine model places the wind maximum at the edge of the mass sink and requires the hydrostatic assumption. The new model places the wind maximum within the mass sink and allows for the hydrostatic defect. The new model fits the data from Wilkins' vortex and shows no systematic deviations, whereas the deviations from the Rankine vortex are both systematic and large in each of the regimes.

The analysis established that the frictional force is a significant factor, the importance of which is incorporated in the new model as opposed to the Rankine vortex where it is omitted. The frictional force creates vorticity on the one hand and destroys angular momentum on the other. The governing effects of friction appears to a factor in other vortices, since a nondimensional form fits the data of five other examples moderately well.

A Lagrangian View of the Vortex

To summarize what is involved in the new model, it is useful to follow a parcel as it travels through the vortex and to visualize its motion from the Lagrangian viewpoint.

The parcel begins its journey into the vortex through the slits of the spinning cage where it enters from the ambient atmosphere in response to the pressure forces. Viscous forces accelerate the parcel to the angular momentum of the cage wall.

The parcel continues to accelerate in the radial direction in response to an internal pressure gradient force. Here several things happen to the parcel. As it moves inward, the viscous drag from the upper and lower boundaries of the cage cause the parcel to yield angular momentum to the

lower and upper surfaces of the outer cage. This process creates vorticity. The parcel's spin or vorticity exhibits the peculiar quality that the ever-tightening spiral results in an increasing shear which exactly compensates for the increase in curvature of the parcel trajectory, thus insuring that vorticity remains constant. This unique behavior allows the lateral frictional force to remain zero while the tangential component of the parcel increases. The rate of speed-up of the parcel increases with its movement toward the vortex center.

A dramatic change of affairs occurs at the edge of the mass sink. There is no roof of the cage as the parcel passes into the inner vortex. The suction of the fan is felt directly and the parcel begins to ascend. The vertical pull is joined by strong lateral frictional drag, but again the curl of the lateral frictional forces is zero. The rate of increase of speed of the parcel begins to decrease although the parcel is still speeding up. The pressure is falling most rapidly now, and vorticity is being created at such a fast pace that a miniature tornado is generated. A hundredth of a second after the parcel enters the inner vortex, it passes through the wind maximum. The tangential component of the parcel decreases as the parcel spirals up and out of the vortex' center to return to the outside atmosphere. As it leaves, it is followed by another parcel, and yet another, each of which experiences an identical trip if only a fraction of a second later. The reason for this is that the same conditions prevail in the vortex at each radius, an unchanging function of time. It is only the parcel traveling through the vortex which experiences the rapid changes while the history of each parcel is identical.

6. Conclusion

In this study, a new improved model of the tangential velocity field of a three-dimensional steady-state, axially symmetric vortex in a rotating Dines vortex cage is developed. The model displays a wind minimum and maximum similar to wind profiles observed in natural vortices. A brief summary of the findings are:

1. The horizontal Laplacian $(\nabla_z^2 \zeta)$ of the vertical velocity field is zero.

2. The vertical component of the curl of the lateral frictional force is zero throughout the whole vortex.

3. The coefficient of viscosity for the lateral frictional force may be considered constant.

4. The model shows two distinct regimes of mass circulation, each having distinct vorticity characteristics, attributable in part to

the two- or three-dimensional nature of the circulation and boundary conditions.

5. The model contains a vortex eye, a smooth and continuous wind maximum which is dynamically viable in the presence of a mass circulation, and a tapering outer wind regime.

6. The frictional force is the only force that exerts a role in governing the tangential velocity distribution in the new model.

7. Boundary conditions are satisfied in the steady-state vortex.

8. The vorticity and angular momentum distributions computed from Wilkins' data for a laboratory vortex support the hypothesis.

9. The nondimensional form of the model is supported by data from five other vortices, evidence from a range of seven orders of magnitude, and suggests potential application to spiral galaxies.

Acknowledgments

The authors express their appreciation to Professor V. E. Suomi for his interest and encouragement and to Professors L. H. Horn and H. H. Lettau for their constructive criticism.

References

Anthes, Richard Allen, 1970: A Diagnostic Model of the Tropical Cyclone in Isentropic Coordinates, ESSA Technical Memorandum ERKTM-NHRL 89, 147 pp.

Batchelor, G. K., 1967: An Introduction to Fluid Dynamics, Cambridge University Press, London, 615 pp.

Bjerknes, V. et al., 1898: Ueber die Bildung von Cirkulations-bewegungen in reibungslosen Flüssigkeiten. Vitensel skabets Skrifter (Oslo), Math.-Naturv. Klasse, No. 5, pp. 1-29.

Dines, W. H., 1896: Experiment illustrating the formation of the tornado cloud, Quart. J. Roy. Meteorol. Soc., 22, pp. 71-74.

Dryden, Hugh L., Francis D. Murnaghan, 1960: Hydrodynamics, Dover, New York, 634 pp.

Haltiner, George J. and Frank L. Martin, 1957: Dynamic Meteorology, McGraw-Hill Book Co., Inc., New York, 470 pp.

Helmholtz, H. 1858: Ueber Integrale der hydrodynamischen Gleichungen welcheden Wirbelbewegungen entsprechen, Journal für die reine und angewante Mathematik, Bd. 55, pp. 25-55.

Hoecker, Walter H. Jr., 1960: Wind Speed and Air Flow Patterns in the Dallas tornado of April 2, 1957, MWR, Vol. 88, No. 5, pp. 167-180.

Kuo, H. L., 1960: Dynamics of Convective Vortices and Eye Formation, Rossby Memorial Volume, Oxford University Press, pp. 413-424.

Lamberth, Roy L., 1966: On the Measurement of Dust Devil Parameters, Bull. Amer. Met. Soc., Vol. 47, No. 7, pp. 522-526.

Lilly, D. K., 1969: Tornado Dynamics, paper delivered at the 6th National Hurricane Conference in Miami, abstract presented in AMS Bulletin.

Panofsky, Hans A., 1968: Introduction to Dynamic Meteorology, Penn. State University, University Park, Penn. 243 pp.

Rankine, W. J., 1888: A Manual of Applied Mechanics, London, Charles Griffin and Co., 667 pp.

Rosenthal, S. L., 1970a: Experiment with a numerical model of tropical cyclone development—some effects of radial revolution, MWR, 98, No. 2, pp. 106-120.

Rubin, V. C. and W. K. Ford, Jr., 1970: A Comparison of Dynamical Models of the Andromeda Nebula and the Galaxy, Symposium No. 38. The Spiral Structure of our Galaxy, ed. W. Becker, Astronomsich-Meteorologische Anstalt, Binningen, Switzerland, and G. Contopoulos, University of Thessanlonika, Thessaloniki, Greece. D. Riedel Publishing Co., Dordrecht Holland. Springer-Verlag, New York/New York.

Phillips, H. B., 1933: Vector Analysis, John Wiley and Sons, Inc., New York, 236 pp.

Schlichting, H., 1955: Boundary Layer Theory, Pergamon Press, New York, 535 pp.

Sinclair, Peter C., 1964: Some Preliminary Dust Devil Measurements, Monthly Weather Review, Vol. 92, No. 8, pp. 363-367.

Smagorinsky, J., 1963: General Circulation Experiments with the Primitive Equations, MWR, 91, pp. 99-152.

Taylor, G. I., 1932: Transport of vorticity and heat through fluids in turbulent motion, Proc. Roy. Soc. London Ser. A, 135, pp. 685-702.

Vonnegut, B., 1960: The electrical theory of tornadoes, J. Geophys. Res., 65, pp. 203-212.

Wilkins, E. M., 1962: The Role of Electrical Phenomena Associated with Tornadoes, J. Geophys. Res., 69, pp. 2435-2447.

Ying, S. J. and C. C. Chang, 1970: Exploratory Model Study of Tornado-like Vortex Dynamics, JAS, Vol. 27, No. 1, pp. 3-14.